

# Annual Report 2023

Laboratory of Radiochemistry

### Cover

View inside the gas stopping cell with the DC cage (front) and the ion funnel (back), which enables the thermalization and extraction of nuclear reaction products into vacuum. Combined with vacuum adsorption chromatography, millisecond chemistry experiments with superheavy elements beyond flerovium are within reach. The setup was commissioned with  $^{216}\text{Po}$  ( $t_{1/2} = 144$  ms), i.e., with a radioisotope of the lighter homolog of element livermorium (Lv,  $Z = 116$ ).

PAUL SCHERRER INSTITUT



# Annual Report 2023

Laboratory of Radiochemistry

**Editors**

Robert Eichler and Patrick Steinegger

**Paul Scherrer Institut**  
Laboratory of Radiochemistry  
5232 Villigen PSI  
Switzerland  
Secretariat +41 56 310 24 01  
Fax +41 56 310 44 35

**Reports are available from**  
Sandha Keller  
sandha.keller@psi.ch  
Paul Scherrer Institut  
5232 Villigen PSI  
Switzerland



See also our web-page  
<https://www.psi.ch/lrc/>

## Table of Content

<b>Editorial</b>	1
<i>R. Eichler (PSI &amp; UniBe)</i>	
<b>Production of short-lived Hg isotopes for sub-second chemistry</b>	3
<i>G. Tiebel (ETHZ &amp; PSI), R. Dressler (PSI), R. Eichler (PSI &amp; UniBe), C. M. Folden III (Cyclotron Institute &amp; Dep. of Chemistry), A. Kirkland (Cyclotron Institute &amp; Dep. of Chemistry), J. Mildon (Cyclotron Institute &amp; Dep. of Chemistry), E. Tereshatov (Cyclotron Institute), V. Zakusilova (Cyclotron Institute), P. Steinegger (ETHZ &amp; PSI)</i>	
<b>The ion-funnel-to-IVAC system</b>	5
<i>G. Tiebel (ETHZ &amp; PSI), R. Dressler (PSI), R. Eichler (PSI &amp; UniBe), C. M. Folden III (Cyclotron Institute &amp; Dep. of Chemistry), D. Herrmann (PSI), Y. Ito (JAEA), A. Kirkland (Cyclotron Institute &amp; Dep. of Chemistry), E. Tereshatov (Cyclotron Institute), A. Vögele (PSI), P. Steinegger (ETHZ &amp; PSI)</i>	
<b>An analytical approach to simulating molecular flow in IVAC experiments with superheavy elements</b>	7
<i>N. Iwanojko (PSI &amp; ETHZ), R. Dressler (PSI), G. Tiebel (PSI &amp; ETHZ), P. Steinegger (PSI &amp; ETHZ)</i>	
<b>Online gas-adsorption chromatography of Tl on dehydroxylated fused silica surfaces at JAEA</b>	9
<i>J. Wilson (ETHZ &amp; PSI), M. Asai, Y. Ito, Y. Nagame, K. Tsukada (JAEA), R. Eichler (PSI &amp; UniBe), G. Gyeongmin, Y. Miyachi, H. Natori, Y. Uchibab (IBU &amp; JAEA), K. Tokoi, A. Toyoshima (Osaka University), T. K. Sato (JAEA &amp; IBU), and P. Steinegger (ETHZ &amp; PSI)</i>	
<b>Offline thermochromatography of Tl on various dehydroxylated fused silica surfaces</b>	11
<i>C. Gut (ETHZ &amp; PSI), J. Wilson (ETHZ &amp; PSI), P. V. Grundler (PSI), N. P. van der Meulen (PSI), A. Sommerhalder (PSI), and P. Steinegger (ETHZ &amp; PSI)</i>	
<b>The nature of lanthanoid impurities in highly pure U materials</b>	13
<i>M. Hofstetter (ETHZ, Spiez Laboratory &amp; PSI), S. Röllin (Spiez Laboratory), P. Steinegger (ETHZ &amp; PSI)</i>	
<b>Quantifying impurities in highly pure U materials</b>	15
<i>M. Hofstetter (ETHZ, Spiez Laboratory &amp; PSI), S. Röllin (Spiez Laboratory), P. Steinegger (ETHZ &amp; PSI)</i>	
<b>From batch to flow electrolysis: The separation of <sup>110m</sup>Ag</b>	17
<i>P. Dutheil (PSI &amp; ETHZ), M. Heule (PSI), P. Steinegger (PSI &amp; ETHZ), A. Vögele (PSI)</i>	
<b>Development of an aerosol gas-jet degasser-unit for liquid-phase chemical studies with fission-products at SINQ</b>	19
<i>A. Pelletier (EPFL), P. Dutheil (PSI), R. Dressler (PSI), P. Steinegger (PSI)</i>	
<b>Preparation of natural hafnium samples for the production of <sup>179</sup>Ta</b>	21
<i>P. Albrecht (ETHZ &amp; PSI), Đ. Cvjetinović (PSI), P. Grundler (PSI), D. Schumann (PSI)</i>	
<b><sup>32</sup>Si activity measurements at IRA for the SINCHRON project</b>	24
<i>Y. Nedjadi (IRA), M. T. Durán (IRA), D. Cvjetinovic (PSI), M. Veicht (EPFL &amp; PSI), D. Schumann (PSI), and C. Bailat (IRA)</i>	
<b>Thermosublimatographic study of tellurium evaporation from lead-bismuth eutectic melts</b>	26
<i>V. Zobnin (PSI &amp; UniBe), L. Mössinger (Universität Hamburg), J. Neuhausen (PSI), R. Eichler (PSI &amp; UniBe)</i>	
<b>Thallium release from LBE doped with iodine determined from transpiration data</b>	28
<i>J. Neuhausen (PSI), I. I. Danilov (PSI &amp; UniBe)</i>	

<b>Optimization of a matrix isolation setup for the study of volatile and reactive gaseous Te molecules</b>	30
<i>I. Zivadinovic (PSI &amp; ETHZ), J.-E. Colle (JRC Karlsruhe), A. Kovacs (JRC Karlsruhe), O. Beneš (JRC Karlsruhe), J. Neuhausen (PSI), P. Steinegger (PSI &amp; ETHZ)</i>	
<b>Electrodeposition of thin films of metallic Ho from ionic liquids</b>	32
<i>N. Cerboni (ETHZ &amp; PSI), M. Christl (ETHZ), A. Müller (ETHZ), C. Vockenhuber (ETHZ), P. Steinegger (ETHZ &amp; PSI), E. A. Maugeri (PSI)</i>	
<b>Influence of selected critical parameters on molecular plating</b>	34
<i>X. Kou (ETHZ &amp; PSI), N. Cerboni (ETHZ &amp; PSI), D. Ferri (PSI), P. Steinegger (ETHZ &amp; PSI), E. Maugeri (PSI)</i>	
<b>Electrodeposition of Tb films from ionic liquids</b>	36
<i>F. Weigand (ETHZ), N. Cerboni (PSI &amp; ETHZ), P. Steinegger (PSI &amp; ETHZ), E. A. Maugeri (PSI)</i>	
<b>Production of Tb/Pd targets and their characterization</b>	38
<i>N. Cerboni (ETHZ &amp; PSI), M. Wörle (ETHZ), P. Steinegger (ETHZ &amp; PSI), E. A. Maugeri (PSI)</i>	
<b>Investigation of a Pd-Gd intermetallic target</b>	40
<i>X. Kou (ETHZ &amp; PSI), N. Cerboni (ETHZ &amp; PSI), E. Mueller (PSI), M. Makowska (PSI), M. Muntwiler (PSI), P. Steinegger (ETHZ &amp; PSI), E. Maugeri (PSI)</i>	
<b>Adsorption and separation of lanthanides by amido-type adsorbent</b>	42
<i>X. Pan (SJTU &amp; PSI), Đ. Cvjetinović (PSI), J. Petrović (PSI), M. Würtenberg (PSI), D. Schumann (PSI)</i>	
<b>Production of mass-separated <sup>169</sup>Er: a focus on separation efficiency</b>	44
<i>C. Duchemin, T. Stora, C. Crepieux, M. Inzamam, L. Lambert, C. Bernerd, R. Rossel (CERN), U. Köster (ILL), E. Renaldin, N. P. van der Meulen, Z. Talip (PSI)</i>	
<b>Preliminary studies for the activity standardization of <sup>167</sup>Tm</b>	46
<i>Y. Nedjadi (IRA), F. Juget (IRA), M. T. Duran (IRA), E. Renaldin (PSI &amp; UniBe), C. Favaretto (PSI), C. Duchemin (CERN), T. Stora (CERN), N. P. van der Meulen (PSI), Z. Talip (PSI)</i>	
<b>Production of <sup>152</sup>Tb and <sup>169</sup>Yb using medium energy cyclotron</b>	48
<i>S. Pasolini (PSI), E. Renaldin (PSI &amp; UniBe), A. Sommerhalder (PSI), H. Zhang (PSI) N.P. van der Meulen (PSI), Z. Talip (PSI)</i>	
<b>Cross-section measurements of proton-induced reactions on <sup>nat</sup>Dy<sub>2</sub>O<sub>3</sub> for the <sup>161</sup>Ho production with a medical cyclotron</b>	50
<i>E. Renaldin (PSI &amp; UniBe), R. Zehnder (PSI &amp; UniBe), S. Braccini (AEC-LHEP, UniBe), N. P. van der Meulen (PSI), R. Eichler (PSI &amp; UniBe), Z. Talip (PSI)</i>	
<b>Cyclotron production of a medically relevant radionuclide <sup>161</sup>Ho</b>	52
<i>E. Renaldin (PSI &amp; UniBe), A. Sommerhalder (PSI), H. Zhang (PSI), N. P. van der Meulen (PSI), R. Eichler (PSI &amp; UniBe), Z. Talip (PSI)</i>	
<b>Production of high specific activity <sup>166</sup>Ho for targeted radionuclide therapy</b>	54
<i>E. Renaldin (PSI &amp; UniBe), U. Köster (ILL), A. Vögele (PSI), N. P. van der Meulen (PSI), R. Eichler (PSI &amp; UniBe), Z. Talip (PSI)</i>	
<b>Production of <sup>155</sup>Tb via <sup>155</sup>Dy by irradiation of <sup>nat</sup>Tb by medium energy protons</b>	56
<i>A. N. Moiseeva (PSI), C. Favaretto (PSI), Z. Talip (PSI), P.V. Grundler (PSI), C. C. Hillhouse (PSI), R. Eichler (PSI &amp; UniBe), R. Schibli (PSI &amp; ETHZ), N. P. van der Meulen (PSI)</i>	
<b>Developing direct <sup>68</sup>Ga production for medical cyclotrons</b>	58
<i>P. V. Grundler (PSI), S. Braccini (LHEP, UniBe), N. P. van der Meulen (PSI)</i>	

<b>First-in-human administration of [<sup>161</sup>Tb]Tb-DOTA-LM3 in a patient with metastatic neuroendocrine tumour of the ileum</b>	60
<i>C. Favaretto (USB &amp; PSI), J. Fricke (USB), F. Westerbergh (University of Gothenburg), L. McDougall (USB), P.V. Grundler (PSI), S. Geistlich (PSI), P. Bernhardt (University of Gothenburg), N. P. van der Meulen (PSI), R. Schibli (PSI &amp; ETHZ), D. Wild (USB)</i>	
<b>Improving the cyclotron production of scandium-44 towards its application in nuclear medicine</b>	61
<i>C. Favaretto (USB &amp; PSI), P.V. Grundler (PSI), A. Sommerhalder (PSI), R. Schibli (PSI &amp; ETHZ), N. P. van der Meulen (PSI)</i>	
<b>Research studies towards production of medical isotopes using ISOL techniques</b>	62
<i>M. Mostamand (PSI)</i>	
Organigram	64
List of publication 2023	65
Contributions to conferences, workshops and seminars	70
Public relations and outreach activities	77
Internal presentations	77
Membership in scientific committees and external activities	78
Lectures and courses	79
Awards	80
Master Thesis	80
Bachelor thesis	81
Internship and Semester projects	81
Grants / fundings	82
Visiting guests	82
Presentations in LRC seminars	83



## Editorial

R. Eichler (PSI & Universität Bern)

---

Dear reader,

It is my pleasure to present to you the annual report of LRC for the year 2023. Traditionally, it summarizes once in a year the status of ongoing scientific projects as well as exciting scientific achievements of our laboratory. The addressed topics of radiochemistry show our broad multidisciplinary scientific involvements.

Being strongly committed to academic teaching as well as apprentice education we have a permanently changing personnel structure amongst the young generation in LRC, which I personally consider an exciting challenge. New characters and personalities enrich our daily lives with new perspectives and bright ideas. Thus, we welcome all new apprentices, bachelor, master, PhD-students, as well as Postdocs who decided or were awarded to work with us at LRC.

Our lively participation at national and international conferences to meet our peers and colleagues in person was extremely fruitful not only to present our research highlights but also to establish new collaborations. Thus, first joint experiments of LRC became possible with research groups at Texas A&M University, USA (Prof. C.M. Folden III) and at IMP Lanzhou, PR China (Prof. Q. Zhi). The big transactinide conference TAN in Huizhou impressively revealed our international standing in the field of transactinide research.

For awards, which are a great PR for LRC acknowledging our successful work, I would like to congratulate Georg Tiebel winning the NES PhD-day award 2023 for LRC, Michael Hofstetter, who was awarded as runner-up for the Poster Prize at the SCS Fall Meeting 2023 and Ivan Zivadinovic who won the 2<sup>nd</sup> place poster prize at the SCK-CEN summer school.

My sincere congratulations go also to the entire team of more than 100 professionals from the PSI-departments GFA, NUM, NES, BIO and LOG! Their commitment was key in convincing the SBFi to put the IMPACT project (<https://www.psi.ch/impact>) on the Roadmap of Swiss Research Infrastructures 2025-2028 for the decision of the Swiss parliament in December 2024. The TATTOOS part is initiated jointly by LRC and CRS who will certainly profit from the expanded radionuclide portfolio by using high-energy proton-induced spallation. Please keep your fingers crossed, that we can start building in 2025! I wish everybody

great persistence and success for furthering if not even finalizing the first technical designs.

A greatly visible scientific highlight of LRC and CRS was certainly the start of the clinical study with Tb-161. This collaborative effort with Prof. D. Wild's group at University Hospital in Basel allowed overcoming logistics challenges with collaborating reactor facilities at NESCA (South Africa) and ILL (Grenoble, France) and thus, for the first time a radionuclide could be introduced to medical application within Switzerland. So far, seven patients have been treated, hopefully, revealing the advantage of the Auger-electron emitting radionuclide Tb-161 in comparison with the gold standard, Lu-177. Let me congratulate Nick van der Meulen and his group who were heavily involved in these efforts and this great success.

This year, EU - Horizon 2020 calls were out and LRC is strongly involved in more than 5 project applications, revealing that we are internationally very active in the acquisition of third-party money.

Our joint laboratory activities demonstrate and also facilitate the great social team spirit within LRC. During this year's excursion (thank you Zeynep for arranging this!) we travelled to St Gallen to visit the EMPA facilities, to learn about material sciences and see exciting laboratories. The visit of the famous great library in the Abbey of St. Gallen was an eye-opener to the history of science – beautiful and impressive. The day was concluded with a delicious apéro riche at the "focacceria". Lastly, our Christmas party led us to the Aargauer Weinbaumuseum in Tegerfelden, where we enjoyed a great evening with many laughs.

Finally, let me thank all members of LRC for their positive attitude, their perseverance and their exceptional professionalism, allowing us to blossom scientifically and personally. It's my great pleasure and privilege supporting and leading LRC through the daily challenges solving radiochemical mysteries.

Enjoy reading about our radiochemical research @ LRC as we do enjoy researching!





# Production of short-lived Hg isotopes for sub-second chemistry

G. Tiebel (ETHZ & PSI), R. Dressler (PSI), R. Eichler (PSI & UniBe), C. M. Folden III (Cyclotron Institute & Dep. of Chemistry), A. Kirkland (Cyclotron Institute & Dep. of Chemistry), J. Mildon (Cyclotron Institute & Dep. of Chemistry), E. Tereshatov (Cyclotron Institute), V. Zakusilova (Cyclotron Institute), P. Steinegger (ETHZ & PSI)

## Introduction

The chemical characterization of superheavy elements (SHEs;  $Z \geq 104$ ) by means of gas adsorption chromatography in the continuum flow regime is limited to radionuclides having half-lives longer than  $\approx 1$  s [1]. In contrast, chemistry experiments in the molecular flow regime may enable the chemical investigation of SHEs beyond flerovium (Fl,  $Z = 114$ ), whose radioisotopes exclusively feature half-lives in the sub-second range. Feasibility studies with the lighter homologs of SHEs, such as Tl for Nh ( $Z = 113$ ), have been performed in the past, confirming the general applicability of this approach [2]. In a next step, the envisaged fast transport times of investigated chemical species must be demonstrated.

Hg has been selected for this benchmark experiments due to its comparatively low adsorption enthalpy of  $-\Delta H_{ads}^{SiO_2}(Hg) = 42 \text{ kJ mol}^{-1}$  on fused silica as the stationary phase [3]. The minimum retention already at room temperature enables a fast transport of Hg at ambient conditions. The reasonably high cross sections to produce sufficiently short-lived,  $\alpha$ -active radioisotopes of Hg (see Fig. 1) in the sub-mbarn range further underlines the suitability of Hg as an overall promising candidate for this benchmark study. Nuclear fusion-evaporation reactions, such as  $^{144}\text{Sm}(^{40}\text{Ar}, xn)^{184-xn}\text{Hg}$  [5] and  $^{147}\text{Sm}(^{36}\text{Ar}, xn)^{183-xn}\text{Hg}$  [6], are well-suited to produce Hg, thereby mimicking the production of envisaged SHEs.

$^{176}\text{Hg}$	$^{177}\text{Hg}$	$^{178}\text{Hg}$	$^{179}\text{Hg}$	$^{180}\text{Hg}$	$^{181}\text{Hg}$	$^{182}\text{Hg}$	$^{183}\text{Hg}$
20.3 ms	117 ms	266.5 ms	1.05 s	2.59 s	3.6 s	10.83 s	9.4 s

**Figure 1:** Hg radioisotopes of interest; the color code represents the different half-lives (red: short-lived, turquoise: longer-lived) [4].

The general possibility of producing short-lived Hg radioisotopes as well as others (e.g., Po or At) at the Cyclotron Institute of Texas A&M University (TAMU), USA, has been assessed during a beamtime in August 2023. Selected results, as obtained in experimental runs aiming at the production of  $^{177}\text{Hg}$  ( $t_{1/2} = 118$  ms) and/or  $^{178}\text{Hg}$  ( $t_{1/2} = 260$  ms), are presented in this report.

## Experimental

The  $^{36}\text{Ar}$  ion beam ( $E_{lab} = 7.4 \text{ MeV/u}$ ) from the K150 cyclotron at TAMU was guided toward the gas-filled separator AGGIE. Prior to impinging on the mixed Sm target (50%  $^{144}\text{Sm}$ , 50%  $^{147}\text{Sm}$ ), the ion beam passed through a  $10 \mu\text{m}$ -thick Al vacuum window, and optionally, a degrader with interchangeable Al foils of varying thicknesses (1.8 to  $6.3 \mu\text{m}$ ). Thus, the ion beam energy in the target can be adjusted without changing the primary ion beam energy as delivered from the K150 cyclotron. The nuclear reaction products (NRPs), emerging from the target, were directed into AGGIE ( $D_v Q_h D_v$ , i.e., vertically focussing dipole, horizontally focussing quadrupole, vertically focussing dipole) to separate the primary ion-beam as well as nuclear reaction by-products from the evaporation residues (EVRs, i.e., the desired short-lived radioisotopes of Hg). The EVRs were implanted into a double-sided silicon strip detector consisting of 120 vertical (front side) and 80 horizontal (back side) strips defining a  $120 \times 80$  pixel matrix, mounted in the focal plane of AGGIE. This detector was used in combination with an event-by-event data acquisition system registering the position of the implantation event as well as the subsequent energy signals originating from the subsequent  $\alpha$ -decays of the EVRs and their daughters.

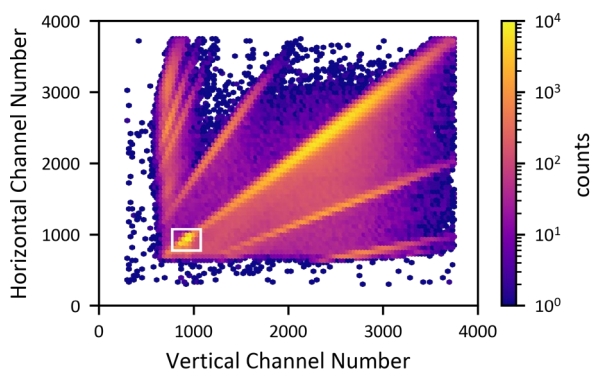


**Figure 2:** Example plot of the original data (events in all pixels) of one run with the linear center line as the region of consistent energy signals in both detectors (the framed white rectangle marks the region of the aimed at  $\alpha$ -spectrum).

## Results and discussion

The uncalibrated plot of summed responses of all pixels shows a significant contribution of scattered particles besides implantation or  $\alpha$ -decay events (see Fig. 2). A

filter algorithm was applied to remove irrelevant data located outside the central region of the plot (i.e., signals resulting from proper implantations and  $\alpha$ -decays).

The removal of undesired events and subsequent energy calibration produced a background-reduced  $\alpha$ -spectrum superimposed by the implantation signals (see Fig. 3; corresponds to a projection along the central region in Fig. 2 toward the recorded vertical energy). Noteworthy features include  $\alpha$ -lines of  $^{181}\text{Au}$  ( $E_\alpha = 5.47$  MeV) and  $^{182}\text{Au}$  ( $E_\alpha = 5.3$  MeV) as NRPs from  $^{36}\text{Ar}$ -induced pxn-reactions, as well as the  $\alpha$ -decays of the desired Hg radioisotopes in the 5.6 to 7 MeV range.

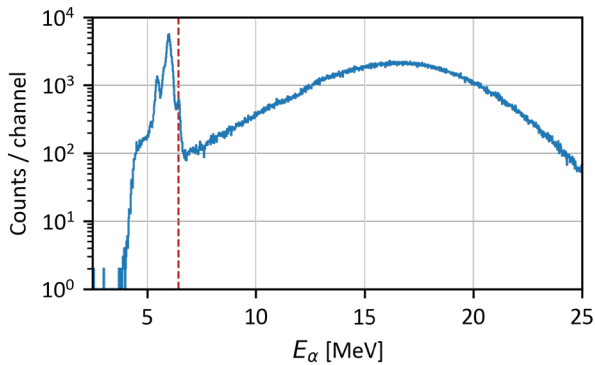


**Figure 3:** Background-reduced spectrum of implantation events and  $\alpha$ -decays of combined runs ( $t_{exp} = 180$  min) with a  $3.8\ \mu\text{m}$ -thick Al degrader foil; the peak on the high-energy shoulder at approximately 6.45 MeV indicates the presence of  $^{178}\text{Hg}$  (red dashed line).

A correlation search was conducted to unambiguously identify recoil- $\alpha$ - $\alpha$ -sequences associated with the implantation of short-lived  $^{177}\text{Hg}$  ( $t_{1/2} = 118$  ms) and/or  $^{178}\text{Hg}$  ( $t_{1/2} = 260$  ms). For this purpose, a conservative correlation window has been selected, considering the lifetime of the mother (i.e.,  $3 \cdot \tau^M$ ) and the daughter (i.e.,  $3 \cdot \tau^D$ ) radionuclides, as well as their respective  $\alpha$ -energies (refer to Fig. 4 as an example for  $^{178}\text{Hg}$ ). The use of a mixed target led to the production of  $^{175}\text{Au}$ , primarily due to the comparatively high cross section of the reaction  $^{144}\text{Sm}(^{36}\text{Ar}, p4n)^{175}\text{Au}$ . Unfortunately, this radionuclide shares similar decay characteristics with  $^{178}\text{Hg}$ , resulting in a lower peak maximum in the lifetime histogram compared to theoretical data (Fig. 4., right side). Thus, the clear distinction between these two radionuclides by correlation analysis proved difficult, and the preliminary results presented here (Fig. 4) represent a superposition of both the of  $^{178}\text{Hg}$  (5n-channel with  $^{147}\text{Sm}$  target) and  $^{175}\text{Au}$  (p4n-channel from  $^{144}\text{Sm}$  target).

By varying the centre-of-target energy in combination with the above-described correlation analysis, an optimum ion beam energy was assessed to produce  $^{178}\text{Hg}/^{175}\text{Au}$  and  $^{177}\text{Hg}$ . The number of correlated events was normalized to the response of the Rutherford-scattering-detectors positioned at the entrance of AGGIE. The response of these detectors corresponds to the luminosity of the irradiation, i.e., total number of

incident ion beam particles times the number of target atoms in the ion beam spot per experimental run. The highest level of production was observed at approximately 210 MeV centre-of-target ion beam energy, i.e., a parameter that will be considered for future experiments.

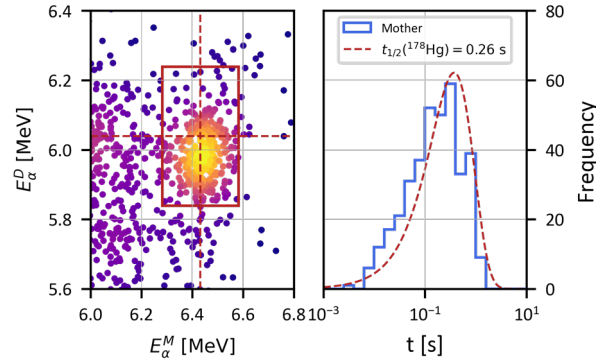


**Figure 4:** Example result of the recoil- $\alpha$ - $\alpha$  correlation analysis for  $^{178}\text{Hg}$  with correlated events (left side) and the histogram of recoil- $\alpha$  correlation times (right side), indicative for the half-life of the initially implanted mother radionuclide (red dashed line) [7]; the analysis confirms a successful production of short-lived  $^{178}\text{Hg}$  (mother, M) in the irradiation of  $^{144/147}\text{Sm}$  with a 210 MeV  $^{36}\text{Ar}$  center-of-target ion beam energy. Chosen correlation window:  $E_\alpha^M = 6.43 \pm 0.10$  MeV with  $3 \cdot \tau^M = 1.13$  s,  $E_\alpha^D = 5.980 \pm 0.125$  MeV with  $3 \cdot \tau^D = 3.86$  s ( $^{174}\text{Pt}$  as daughter, D). The red lines in the left figure indicate the correlation windows for  $^{178}\text{Hg}$ .

In summary, the potential for the production and separation of short-lived Hg radioisotopes at the heavy-ion accelerator K150 and the gas-filled recoil separator AGGIE of the Cyclotron Institute at Texas A&M University was successfully evaluated.  $^{177}\text{Hg}$  and  $^{178}\text{Hg}$ , were unambiguously identified together with the optimum ion beam and separator settings. These findings enable first chemistry experiments *in vacuo* to characterize radionuclides with half-lives in the sub-second range.

## Acknowledgements

The authors would like to thank the operating staff of the Cyclotron Institute of TAMU for the stable beam and the SNSF for funding (grant no. 200020\_196981/1).

## References

- [1] A. Türlér, V. Pershina, *Chem. Rev.*, **113**, 1237-1312, (2013)
- [2] P. Steinegger et al., *J. Phys. Chem. C*, **120**, 7122-7132, (2016)
- [3] S. Soverna, Attempt to Chemically Characterize Element 112, Universität Bern, (2004)
- [4] <https://www.nndc.bnl.gov/nudat3/> (accessed on July 09, 2024)
- [5] D. Kamas et al., *Phys. Rev. C*, **105**, 44612, (2022)
- [6] R. D. Page et al., *Phys. Rev. C*, **84**, 34308, (2011)
- [7] K. H. Schmidt et al., *Z. Phys. A - Atoms and Nuclei*, **316**, 19-26 (1984)

## The ion-funnel-to-IVAC system

G. Tiebel (ETHZ & PSI), R. Dressler (PSI), R. Eichler (PSI & UniBe), C. M. Folden III (Cyclotron Institute & Dep. of Chemistry), D. Herrmann (PSI), Y. Ito (JAEA), A. Kirkland (Cyclotron Institute & Dep. of Chemistry), E. Tereshatov (Cyclotron Institute), A. Vögele (PSI), P. Steinegger (ETHZ & PSI)

### Introduction

Isothermal vacuum chromatography (IVAC) is envisaged as a method to overcome the speed limitations of state-of-the-art gas adsorption chromatography techniques (i.e., restricted to radionuclides with a minimum half-life  $t_{1/2} \approx 1$  s) for the chemical characterization of superheavy elements (SHEs;  $Z \geq 104$ ) beyond Fl ( $Z = 114$ ) [1, 2]. The accelerator-based production of radionuclides of SHEs in nuclear fusion-evaporation reactions is typically followed by physical pre-separation in the form of vacuum or gas-filled separators. The evaporation residues (EVRs) emerging from the end of a separator feature high kinetic energies (i.e., tens of MeV) and are distributed across cm-wide areas. Prior to a chemistry experiment with these EVRs, they must be thermalized. Whereas the implementation of a so-called hot catcher has been explored in the past [2], we decided to proceed with the well-established buffer gas cell (BGC) technology. In such a BGC, ions are thermalized in a low pressure gas (up to 100 mbar) and subsequently transported using a combination of direct current (DC) and radio frequency (RF) electric fields [3-5]. In this report, we present first results of extracted ions from a BGC based on a previously established design [3]. The report provides a description of the experimental setup together with preliminary results in terms of ion transport as well as an efficiency evaluation.

### Experimental setup

The developed system consists of a thermalization chamber featuring a DC cage and a DC-RF ion funnel, a supersonic nozzle (diameter 0.6 mm or 1 mm) at its end, and a transfer chamber equipped with an RF-quadrupole (RFQ) ion guide (see Fig. 1). Two turbomolecular vacuum pumps (chamber evacuation and differential pumping during operation) with high pumping capacities are installed on each chamber. During regular operation, only the pump on the transfer chamber is used for differential pumping to separate the buffer gas from the ions of interest in the RFQ. High-purity He (purity 99.9999%; no additional gas cleaning) was selected as buffer and transport gas. Effective differential pumping has been achieved with helium as working gas by maintaining the thermalization chamber at 32 mbar leading to a pressure of  $10^{-2}$  mbar in the transfer chamber using a

nozzle with a 1 mm orifice. Higher pressures in the thermalization chamber were not possible at that point due to limitations imposed by the backing pump capacity supporting the turbomolecular pump on the transfer chamber.

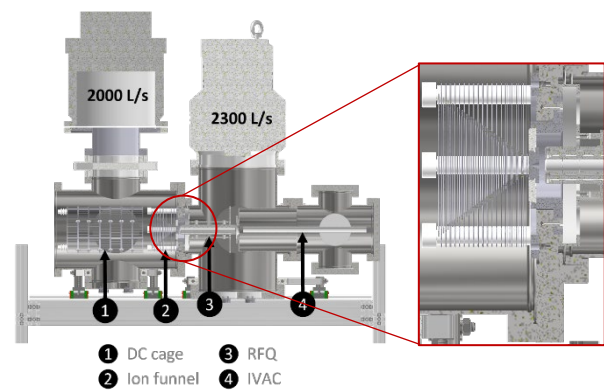


**Figure 1:** Developed BGC with thermalization chamber (DC cage, DC-RF ion funnel) connected to transfer chamber with the RFQ via a supersonic nozzle.

The preliminary evaluation of the ion transport capabilities was carried out with a short-lived isotope of Po ( $^{216}\text{Po}$ ,  $t_{1/2} = 144$  ms) originating from the  $\alpha$ -decay of  $^{220}\text{Rn}$  ( $t_{1/2} = 55.6$  s), which was flushed into the thermalization chamber with the working gas as decay product of natural Th-salt-based ( $^{232}\text{ThF}_4$ ) source. The  $\alpha$ -decays of the successfully transferred radionuclides and their daughters were measured on a Si-PIN diode located approximately 3 cm behind the RFQ exit and 1 cm behind a RF shield (lens with diameter of 11 mm). The optimization of all electric parameters such as the DC gradients as well as RF amplitudes was performed in dependence of the ion transport yield as measured with the stop detector at the end of the RFQ.

### Results and discussion

The resonance frequencies  $f_0$  of both, the ion funnel and the RFQ, were determined by screening various RF frequencies and observing the response of the RF amplitude. It was not possible to fully optimize these resonance frequencies in our experiments, as the inductance ( $L$ ) and capacitance ( $C$ ) of the system (refer to Eq. 1), could not be freely adjusted.

$$f_0 = \frac{1}{2\pi\sqrt{L \cdot C}} \quad (1)$$

Resonance frequencies of 636 kHz for the ion funnel and 766 kHz for the RFQ were determined. After applying the appropriate RF amplitudes and DC gradients,  $^{216}\text{Po}$  ions were successfully transported to the stop detector and their subsequent  $\alpha$ -decay as well as the one of its daughters could be clearly measured (see Fig. 2). Transport was achieved solely by the application of DC and RF fields, as evidenced by the absence of  $\alpha$ -decay of  $^{216}\text{Po}$  or its parent  $^{220}\text{Rn}$  when these fields were not applied.

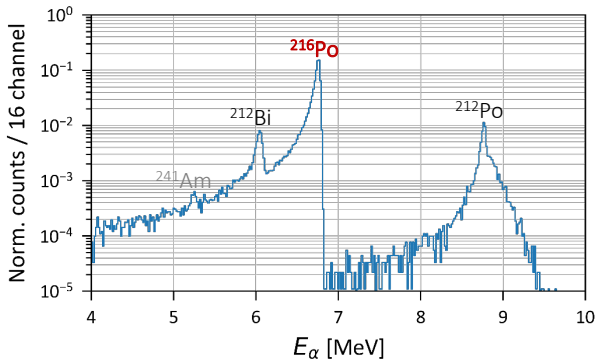


**Figure 2:** Example  $\alpha$ -spectrum of  $^{216}\text{Po}$  and its daughter radionuclides  $^{212}\text{Bi}$  and  $^{212}\text{Po}$  (with large high-energy tailing due to  $^{212}\text{Bi} + ^{212}\text{Po}$  pile-up events). The clear observation of  $^{216}\text{Po}$  proves the successful transport of the short-lived species.  $^{241}\text{Am}$  was used as a calibration source mounted on axis at the beginning of the thermalization chamber.

RF amplitudes as well as DC gradients along the DC cage, the cage-to-funnel, the ion funnel, the funnel-to-nozzle, the nozzle-to-RFQ as well as the RFQ were assessed and have led to a preliminary parameter set for an optimum ion transport. It is noteworthy that the observed count rate may not represent the maximum achievable extraction yield, but it has been deemed satisfactory for preliminary experiments at 290 cpm for more than 4 h (see Fig. 3).

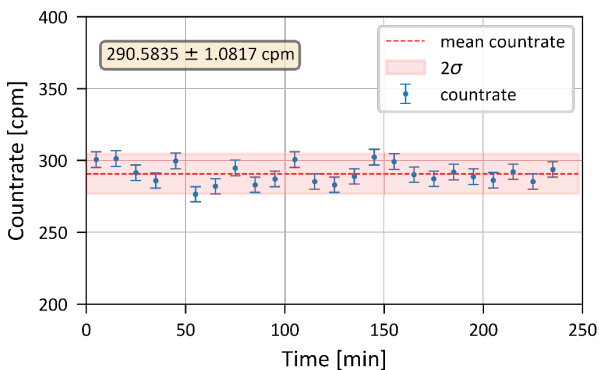


**Figure 3:** Count rate as a function of time indicating the long-term stability of the ion transport. Mean count rate in the figure considering significant figures, i.e.,  $290 \pm 1$  cpm.

Only  $^{216}\text{Po}$  ions produced inside the DC cage or the ion funnel could be transported using the DC and RF electric fields. This enables the evaluation of an extraction efficiency by means of pure geometrical considerations and under the reasonable assumption of a homogenous distribution of  $^{220}\text{Rn}$  within the thermalization chamber. The extraction efficiency of

the system was determined based on the ratios of active (i.e., a decay of  $^{220}\text{Rn}$  inside the cage or ion funnel) and inactive (i.e., a decay of  $^{220}\text{Rn}$  outside the cage of ion funnel) volume. Considering the detection efficiency and the measured maximum radioactivity of  $^{220}\text{Rn}$  transported out of the source container onto an Ag-coated zeolite, the evaluated extraction efficiency amounted to 15%.

## Conclusion and Future Work

The successfully developed BGC adapts an existing design [3] with minor changes, including additional ring electrodes in the DC cage, a slightly modified RFQ and an increased orifice diameter of the nozzle. Preliminary results demonstrate an effective extraction of ions of short-lived  $^{216}\text{Po}$  into vacuum at a moderate efficiency. A comprehensive understanding of the system, supported by ion-optical simulations, is planned. The electronic system for the control of the DC/RF electric fields will be further improved by optimizing the electrical connections of the RFQ and by reducing the capacity of the RF-DC-mixing units. Furthermore, an additional backing pump with higher pumping capacity for He will be installed to enable operation of the thermalization chamber at higher pressures.

## Acknowledgements

The authors would like to thank Dr. Sebastian Raeder and Prof. Michael Block from GSI, Darmstadt, Germany, as well as Peter Hartung and Prof. Peter Thierolf from LMU, Munich, Germany, for their valuable support in sharing information and providing complete technical drawings of the prototype for the BGC. This work was supported by the Swiss National Science Foundation, Switzerland (project grant 200020\_196981/1)

## References

- [1] A. Türlér, V. Pershina, *Chem. Rev.*, **113**, 1237–1312, (2013)
- [2] P. Steinegger et al., *J. Phys. Chem. C*, **120**, 7122–7132, (2016)
- [3] J. B. Neumayr et al., *Nucl. Instrum. Methods Phys. Res. Sect. B Beam Interact. Mater. At.*, **244**, 489–500, (2006)
- [4] C. Droese et al., *Nucl. Instrum. Methods Phys. Res. Sect. B Beam Interact. Mater. At.*, **338**, 126–138, (2014)
- [5] O. Kaleja et al., *Nucl. Instrum. Methods Phys. Res. Sect. B Beam Interact. Mater. At.*, **463**, 280–285, (2020)

# An analytical approach to simulating molecular flow in IVAC experiments with superheavy elements

N. Iwanjko (PSI & ETHZ), R. Dressler (PSI), G. Tiebel (PSI & ETHZ), P. Steinegger (PSI & ETHZ)

## Introduction

Due to low half-lives of radioisotopes of superheavy elements (SHEs) beyond Fl, a promising method to study their chemical properties is isothermal vacuum chromatography (IVAC) [1]. Given their low production rates of only a few atoms-at-a-time, Monte Carlo simulations (MCSs) are commonly used to predict the experimental outcomes as well as to validate and interpret the results. Extensive MCSs with large particle numbers are needed to obtain sufficient statistical confidence in the experimental outcome, leading to long computation times. If analytical solutions were available to describe the migration through an IVAC column for ideally isothermal temperatures and simple settings (we focused here on setup A in [2]) the computational time required to benchmark different setups and evaluate experimental data with SHEs could be significantly reduced [1]. Below we present a framework that could lead to an analytical description of the *in vacuo* chemical characterization of SHEs.

## General setup and strategy

The setup consists of a cylindrical column of radius  $r_c$  with its center aligned along the  $x$ -axis and closed on one end. The length of the column is given by  $\ell_c$ . It is common practice to consider the caliber length  $\mathcal{K}$ , i.e., the ratio  $\mathcal{K} = \ell_c/2r_c$ , as a basic scale unit. Most preparatory experiments in the context of SHE research have been done using chromatography columns with  $10 < \mathcal{K} < 100$ . The migration within the IVAC simulations starts on the plane at  $x = 0$ , which indicates the closed end of the column. The circular detector with outer diameter  $r_c$  is placed perpendicular to the  $x$ -axis at the opposite end of the column. Thus, the position of the detector is given by  $x = \ell_c$  (see Fig. 1).

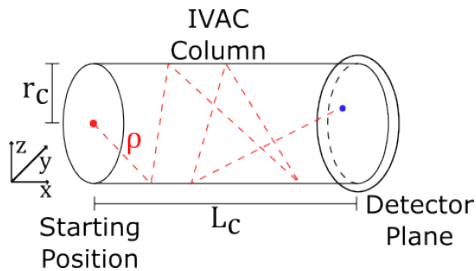


**Figure 1:** Isothermal vacuum chromatography setup with indicated size parameters and an example trajectory (dashed red line). The length of the first flight step  $\rho$  is indicated; the blue point marks the final adsorption position on the detector.

Beijerinck et al. performed MCSs, which enable the description of individual adsorption- and desorption-steps within the column [3]. In total, four different scenarios can be identified to describe a single flight step of a particle between two adsorption sites or the point of detection; these are:

- Case 1:** Desorption from the injection point and direct flight to the detector plane.
- Case 2:** Desorption from the injection point and adsorption on inner wall of the column.
- Case 3:** Desorption from the inner wall of the column and adsorption on the detector.
- Case 4:** Desorption from the inner wall of the column and adsorption on inner wall of the column.

In the following, a comparison of analytical probability density functions (PDFs) and PDFs obtained by MCSs concerning the trajectory of the migration will be discussed. This comparison involves assessing the four cases mentioned above, each representing a single step. The numerical simulations were performed in Python and done in polar coordinates with

$$\begin{pmatrix} x \\ y \\ z \end{pmatrix} = \begin{pmatrix} \rho \sin \vartheta \cos \varphi \\ \rho \sin \vartheta \sin \varphi \\ \rho \cos \vartheta \end{pmatrix}$$

where  $\rho \in (0, \infty)$  is the length of a single flight step,  $\vartheta \in [0, \pi/2)$  is the local azimuth angle with respect to the surface normal, and  $\varphi \in [0, 2\pi)$  is the local polar angle in the adsorption plane parallel to the  $x$ -axis. The angular distribution of  $\vartheta$  is given by the cosine-law, which is the PDF for the direction of desorption from the chromatographic surface [4]. Meanwhile,  $\varphi$  is uniformly distributed. These distributions can be generated from two uniform random numbers, i.e.,  $\zeta$  and  $\xi \in [0, 1)$ , and  $\vartheta = \sin^{-1}(\sqrt{\zeta})$  and  $\varphi = 2\pi \cdot \xi$ . Using these geometrical considerations, the adsorption distribution on the surfaces defined by the four cases can be determined from spatial desorption distributions following the cosine law. This allows both for an analytical and numerical calculation of the PDFs of a single flight step.

## Results and discussion

Considering that  $\vartheta$  and  $\varphi$  are random variables, the position of the particle after one single flight step is determined by a function of them within the geometry defined by the four cases above. This location can be specified by parameterizing the position of the particle.

**Table 1:** PDFs and central moments for the first three cases with respect either to the flight path  $\rho$  or to the relevant progression direction; “*fix*” indicates constant PDF and “*div*” diverging results.

Case	Parameter	PDF	Mean	Variance
1	$\rho$	$\frac{2\rho_c^2}{\rho^3} \cdot d\rho$	$2\ell_c$	<i>div</i>
	$x$	<i>fix</i> = $\ell_c$		
2	$\rho$	$\frac{2r_c^2}{\rho^3} \cdot d\rho$	$2r_c$	<i>div</i>
	$x$	$\frac{2x \cdot r_c^2}{(x^2 + r_c^2)^2} \cdot dx$	$\frac{\pi r_c}{2}$	<i>div</i>
3	$\rho$	$\frac{4x_0 \sqrt{\rho^2 - x_0^2}}{\pi \rho^3} \cdot d\rho$	<i>div</i>	<i>div</i>
	$x$	<i>fix</i> = $x_0$		
4	$\rho < 2r_c$	$\frac{(\rho^2 + 8r_c^2) \cdot K\left[\frac{\rho^2}{4r_c^2}\right] - 2(\rho^2 + 4r_c^2) \cdot E\left[\frac{\rho^2}{4r_c^2}\right]}{3\pi\rho^3} \cdot d\rho$	$2r_c$	$\frac{16}{3} \cdot r_c^2$
	$2r_c < \rho$	$\frac{(\rho^2 + 2r_c^2) \cdot K\left[\frac{4r_c^2}{\rho^2}\right] - (\rho^2 + 4r_c^2) \cdot E\left[\frac{4r_c^2}{\rho^2}\right]}{3\pi r_0 \rho^2} \cdot d\rho$		
	$x$	$\frac{1}{4r_c} \left(1 - \frac{ x (6r_c^2 + x^2)}{(4r_c^2 + x^2)^{\frac{3}{2}}}\right) \cdot dx$	0	$\frac{8}{3} \cdot r_c^2$

Applying the implicit function theorem allows us to derive the PDF for the position of the particle after desorption. In each case, it is possible to derive a PDF for the linear progression along the column as well as the flight path (see Tab. 1). The calculations were performed with the aid of Mathematica [5]. The functions  $K[x]$  and  $E[x]$  represent the complete elliptic integrals of the first and second kind. In addition, dedicated MCSs for each case were conducted using a Python code. For case 4 a comparison of MCSs and the analytical solution is plotted in Figure 2.

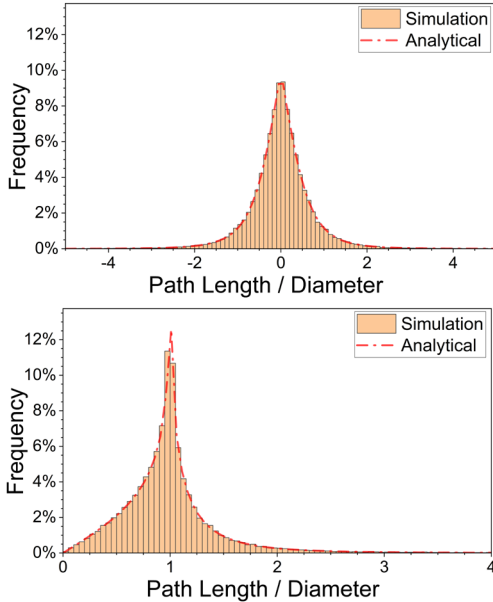


**Figure 2:** Comparison of the PDFs and dedicated simulation results for the linear progression along  $x$  (upper panel) and the flight path length (lower panel) of case 4.

Simulations of several individual steps made it possible to visualize the general behavior of the determined distributions within the scope of the central limit theorem. Although the distribution of single flight path lengths may appear complex, the total flight path

covered after six steps already shows a near-Gaussian distribution. The presence of edge cases increases the complexity of the problem, particularly when it becomes more likely for the particle to exit the column after the last desorption. Simulations of the entire flight path demonstrate that as the caliber length  $\mathcal{K}$  decreases, the distribution of the mean flight path becomes broader (see Fig. 3).

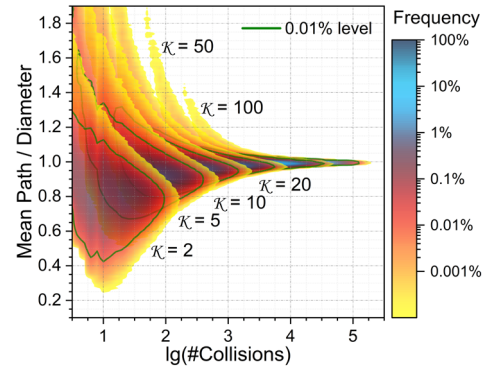


**Figure 3:** Distribution of the mean flight path length as function of the number of wall collision in dependence of various caliber lengths  $\mathcal{K}$ ; the 0.01% level is indicated by a green contour line for each distribution.

In conclusion, for large caliber lengths  $\mathcal{K}$ , the results of case 4 sufficiently describe the flight of the particle. However, as the caliber length  $\mathcal{K}$  decreases, the values for the mean flight path and mean linear progression become unreliable. For sufficiently long columns, an approach analogous to that given by Licata and Grill [6] may be necessary.

## References

- [1] P. Steinegger et al., *J. Phys. Chem. C*, **120**, 7122 (2016)
- [2] G. Tiebel et al., *LRC Annual Report 2021*, 7-8, (2022)
- [3] H.C.W. Beijerinck, et al., *Phys. BC*, **83**, 209 (1976)
- [4] J. Greenwood, *Vacuum*, **67**, 217 (2002)
- [5] Wolfram Research, Inc. Mathematica, Version 13.3
- [6] N.A. Licata, S.W. Grill, *Eur. Phys. J. E*, **30**, 439 (2009)

# Online gas-adsorption chromatography of Tl on dehydroxylated fused silica surfaces at JAEA

J. Wilson (ETHZ & PSI), M. Asai, Y. Ito, Y. Nagame, K. Tsukada (JAEA), R. Eichler (PSI & UniBe), G. Gyeongmin, Y. Miyachi, H. Natori, Y. Uchibab (IBU & JAEA), K. Tokoi, A. Toyoshima (Osaka University), T. K. Sato (JAEA & IBU), and P. Steinegger (ETHZ & PSI)

## Introduction

The chemical study of superheavy elements (SHEs) helps furthering our understanding of how relativistic effects influence chemical properties. Such experiments are particularly challenging, because radioisotopes of SHEs are produced in the order of atoms per day/week/month and have relatively short half-lives (predominantly within the single second region). Gas-adsorption chromatography has proven to be a suitable approach to adapt to these challenging constraints [1]. These experiments yield chromatograms which are then reproduced by Monte Carlo (MC) simulations to find the adsorption enthalpy for a specific chemical species on the selected surface. Typically, homolog studies are completed prior. These then serve as a basis for predictions of properties of their superheavy counterpart and their speciation utilizing periodic trends [1], complemented by relativistic quantum chemical calculations [2]. Regarding group 13, to date, there are three published Nh chemistry experiments [3-5], with accompanying prior homolog studies with Tl [6-9]. The latter were conducted offline using long-lived radiotracers [6] as well as online with short-lived radionuclides [7-9]. Online studies are of particular importance as they mimic the experimental approach used for a later SHE experiment. Despite these initial efforts, the chemical characterization of Nh remains ambiguous. This has triggered an online reinvestigation of the adsorption behavior of Tl on fused silica [9]. Therein, the authors demonstrated the central role of hydroxyl-groups covering the fused silica stationary phase regarding the promotion of multiple chemical species of Tl, i.e., elemental Tl as well as TlOH [9] or even TlOOH. To selectively stabilize one chemical form of Tl, another online study focusing on the pretreatment of fused silica was deemed necessary and is presented here.

## Experimental

At the tandem accelerator facility at the Japan Atomic Energy Agency (JAEA), a  $^{19}\text{F}^{7+}$  ion beam was accelerated to a center of target energy of 118 MeV at 463(15) nA electrical ion beam current. The ion beam first passed through a 9  $\mu\text{m}$  thin Be vacuum window and a 5 mm wide He gas slit for target cooling before impinging on the  $^{nat}\text{Hf}$  metal foil serving as the target (2  $\mu\text{m}$  thin, Goodfellow). The ion beam energy was tuned to

maximize the  $^{193\text{m}}\text{Tl}$  production ( $t_{1/2} = 2.11(15)$  min [10]) as synthesized in the heavy ion-induced nuclear fusion-evaporation reaction  $^{nat}\text{Hf}(^{19}\text{F}, xn)^{193\text{m}}\text{Tl}$  where  $x = 2-6$  (see Fig. 1). The recoiling nuclear reaction products were thermalized in the recoil transfer chamber (RTC) before being flushed by an Ar carrier gas (2 L/min flow rate, G1 grade) into the chromatography section (see Fig. 2). Prior to entering the RTC, the Ar carrier gas first passed through a getter oven with Ti granules kept at 800°C. The thus dried and deoxygenated Ar was introduced diagonally into the RTC, slightly aimed at the target, and perpendicular to the incoming recoils.

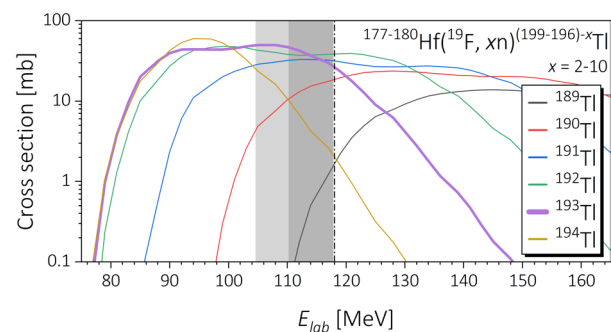


**Figure 1:** Cumulated cross sections for different Tl radioisotopes as calculated with the NRV [11] and normalized to the natural abundance of different Hf isotopes. The energy loss of the  $^{19}\text{F}^{7+}$  ion beam (primary ion beam energy  $E_{lab} = 118$  MeV, dot-dash black line) in the Be vacuum window + He cooling gas slit (dark shaded area) and the  $^{nat}\text{Hf}$  target (light shaded area) were calculated with SRIM [12].

The chromatography setup (see Fig. 2) consisted of a pretreated fused silica column (750 mm, ID 4 mm, OD 6 mm, *Schmizo GmbH*), stretching from the RTC through three independently controlled isothermal ovens (100 mm, 500 mm, 100 mm length, *THERMO-COAX*) to a custom-made clustering chamber (CC, ID  $\approx 20$  mm). For the herein presented results, the chromatography column was pretreated *in situ* in the dried Ar gas with all three ovens set to 850°C (minimum temperature of 592°C), for 8 h. The temperature variations are a consequence of the temperature dips between adjacent ovens. During the subsequent chromatography experiment, the start and end oven were both held at 850°C to reduce all incoming Tl radioisotopes over a hot preheated Ta getter foil and to minimize potential adsorption losses, respectively.

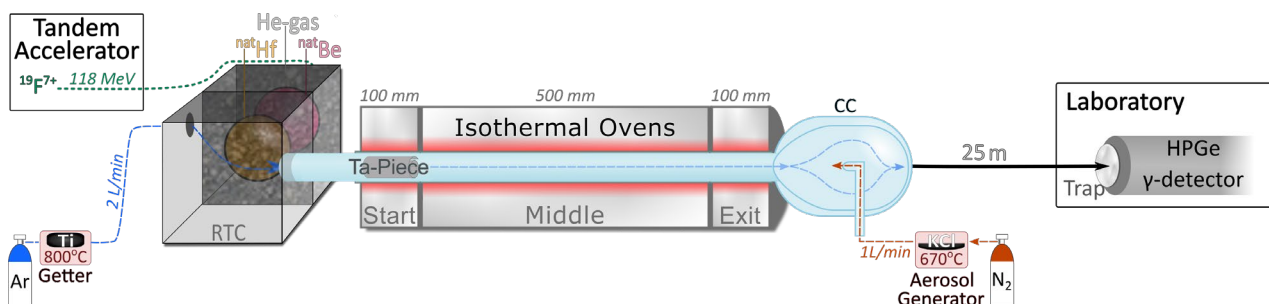


**Figure 2:** Schematic of  $^{193\text{m}}\text{Tl}$  synthesis and subsequent chemistry setup at JAEA; see text for details.

Upon entering the CC,  $^{193\text{m}}\text{Tl}$  adsorbed onto KCl aerosol particles (from KCl salt at  $670^\circ\text{C}$ ) in  $\text{N}_2$  (1 L/min, G1 grade), continuously introduced counter to the Ar carrier gas exiting the chromatography column (see Fig. 2). From there, the aerosol particles were transported to the chemistry laboratory through a 25 m long Teflon tube (OD 1/8", ID 1/16") where they were trapped on a quartz wool filter aligned with an HPGe  $\gamma$ -detector. The aerosol collection included a 10 min idle time prior to spectra acquisition to account for the in-growth of the  $^{193\text{m}}\text{Tl}$ -associated radioactivity. The corresponding external chromatogram shows the relative yield of  $^{193\text{m}}\text{Tl}$  as a function of the setpoint temperature of the chromatography oven (see Fig. 3).

## Results and discussion

In previous homolog experiments, the relative yield of transported Tl irreversibly decreased after the surface was heated above  $400^\circ\text{C}$  for at least 30 min [9]. Beginning at this temperature, fused silica, i.e., the stationary phase, irreversibly dehydroxylates [13]. Since dehydroxylation is temperature and time dependent [13], the surfaces were treated prior to the experiment under conditions mentioned previously.

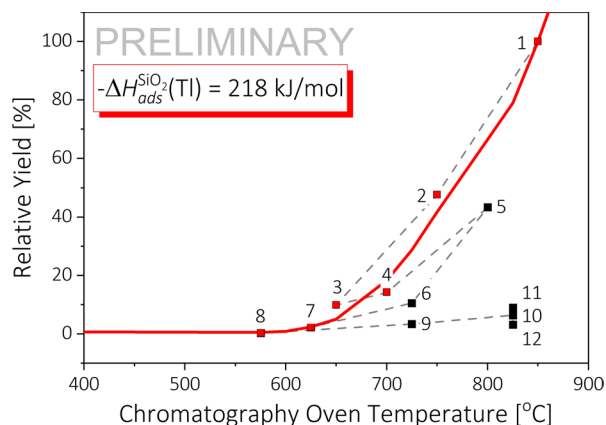


**Figure 3:** The external chromatogram of short-lived  $^{193\text{m}}\text{Tl}$  on fused silica normalized to the maximum activity. The dashed line indicates the acquisition order; selected data points (red squares) were used for preliminary MC simulations (red line).

The recorded external chromatogram (see Fig. 3) is not fully resolved and represents only the onset of the breakthrough of elemental Tl. It can be concluded that this surface pretreatment was sufficient to remove all reactive hydroxyl-groups, i.e., fully suppressing the formation of TlOH [9]. Selected data points were fitted

with a combination of MC simulations and a least-squares method for a preliminary value of the adsorption enthalpy of  $-\Delta H_{\text{ads}}^{\text{SiO}_2}(\text{Tl}) = 218(10)$  kJ/mol for elemental Tl on a dehydroxylated fused silica surface. This value is slightly higher than the previously obtained one of  $-\Delta H_{\text{ads}}^{\text{SiO}_2}(\text{Tl}) = 198(3)$  kJ/mol [9], but differs significantly from the experimental result obtained *in vacuo*, i.e.,  $-\Delta H_{\text{ads}}^{\text{SiO}_2}(\text{Tl}) = 158(3)$  kJ/mol [7]. Theoretical calculations for Tl on various dehydroxylated fused silica surfaces predict significantly lower adsorption enthalpies of  $-\Delta H_{\text{ads}}^{\text{SiO}_2}(\text{Tl}) = 20.1, 44.2$  and  $80.9$  kJ/mol [14]. Meanwhile, the prediction for TlOH on the same surfaces, namely  $-\Delta H_{\text{ads}}^{\text{SiO}_2}(\text{TlOH}) = 133.1, 157,$  and  $324.5$  kJ/mol [14], are somewhat closer. Nonetheless, employing the same chemical reasoning as brought forward in [9], the herein observed species is most likely elemental Tl. In addition to the observation of only one chemical species of Tl, a consistent decrease of the yield is seen with time (black symbols in Fig. 3). This is preliminarily attributed to the progressing oxidation of the Ta surface in the start oven over time adsorbing large quantities of  $^{193\text{m}}\text{Tl}$  (as verified by  $\gamma$ -spectroscopic measurements). Further experiments with different pretreatments of the fused silica chromatography column, conducted during the same beamtime at JAEA, are currently under evaluation.

## Acknowledgements

This work was funded by SNSF (project no. 20020\_196981/1) and the Japan Society for Promoting Science Fellowship (2022 JSPS Intl. Research Fellow).

## References

- [1] R. Eichler et al., *Nature*, **447** (2007).
- [2] V. Pershina et al., *Nuc. Phys. A*, **944** (2015).
- [3] S. Dmitriev et al., *Mendeleev Commun.*, **24** (2014).
- [4] N. Aksenov et al., *Eur. Phys. J. A*, **53** (2017).
- [5] A. Yakushev et al., *Front. Chem.*, **9** (2021).
- [6] A. Serov et al., *Radiochim. Acta*, **101** (2013).
- [7] P. Steinegger et al., *J. Phys. Chem. C*, **9** (2016).
- [8] L. Lens et al., *Radiochim. Acta*, **106** (2018).
- [9] J. Wilson et al., *Inorg. Chem. (under review)* (2024).
- [10] M. Basunia, *Nucl. Data Sheets*, **143** (2017).
- [11] A. Karpov et al., *Nucl. Instrum. Meth. A*, **859** (2017).
- [12] J. Ziegler et al., *Nucl. Instrum. Meth. B*, **268** (2010).
- [13] Z. Yonghen et al., *J. Non-Cryst. Solids*, **352** (2006).
- [14] M. Ilias et al., *Inorg. Chem.*, **61** (2022).

# Offline thermochromatography of Tl on various dehydroxylated fused silica surfaces

C. Gut (ETHZ & PSI), J. Wilson (ETHZ & PSI), P. V. Grundler (PSI), N. P. van der Meulen (PSI), A. Sommerhalder (PSI), P. Steinegger (ETHZ & PSI)

## Introduction

Compared to classic chemistry experiments, chemical investigations of superheavy elements (SHEs) are carried out with a few atoms per day, week, or month. Thus, the lighter homologs are studied in preparation of these demanding experiments since larger quantities of corresponding radioisotopes can be easily produced. As of now, only three chemistry experiments have been published regarding the SHE nihonium (Nh,  $Z = 113$ ) all of which yielding inconclusive results. Prior, Serov and colleagues studied Tl, the lighter homolog of Nh, on fused silica and Au surfaces with the radiotracer  $^{200}\text{Tl}$  via offline thermochromatography [1]. The authors concluded that Tl consistently reacts with fused silica to form TlOH regardless of an oxidizing or reducing atmosphere. Elemental Tl was only found on Au surfaces in combination exclusively with a  $\text{H}_2$  gas flow [1]. In an online isothermal chromatography experiment, the formation of TlOH on fused silica was replicated in addition to the preservation of elemental Tl due to partially dehydroxylated fused silica surfaces [2]. Therein, the authors hypothesized upon the role of hydroxyl-groups as reactive sites preventing the preservation of elemental Tl. The persistence of both Tl species during the online experiment prompted the re-investigation of the Tl adsorption behavior on various dehydroxylated fused silica surfaces via offline thermochromatography.

## Experimental

The  $^{202}\text{Tl}$  radiotracer was produced and separated from the  $^{\text{nat}}\text{HgO}$  target material as described in [3], but with He as a carrier gas instead of Ar. The therein presented methodology ends with  $^{202}\text{Tl}$  adsorbed within a Ta crucible, i.e., the starting point for the herein presented preparations.  $^{202}\text{Tl}$  was transferred from the Ta crucible to preheated Ta foils by heating the Ta crucible to  $> 750^\circ\text{C}$  for 1 h under a 60 ml/min He carrier gas flow.

Meanwhile, fused silica columns (125 cm long,  $\varnothing_{\text{in}} = 5$  cm,  $\varnothing_{\text{out}} = 7$  cm by *Schmizo GmbH*) were thermally pretreated in a separate  $\approx 110$  cm long isothermal oven under a 40 ml/min  $\text{N}_2$  carrier gas flow for 3 h, 8 h, or 40 h at temperatures ranging from  $520^\circ\text{C} - 1075^\circ\text{C}$  (see Fig. 1). Columns which were not used immediately after cooling down were sealed with parafilm for future use.

The full apparatus from [4] was expanded for better gas cleaning and monitoring. Here, the gas proceeded through a cartridge filled with SICAPENT, a getter oven with Ta at  $850^\circ\text{C}$ , then through a pressure gauge and a mass flow controller set at 20 ml/min before passing through a second SICAPENT cartridge into the thermochromatography apparatus. The Ta getter oven was turned on at least 30 min prior to the start of the experiment. The previously prepared  $^{202}\text{Tl}$ -loaded Ta foil was placed within the pretreated fused silica column, aligned to the sample oven ( $> 900^\circ\text{C}$ ). The experiments ran for exactly 3 h, i.e., the duration the ovens were on. The near-isothermal sample oven was followed by a gradient oven with a negative temperature gradient ( $933^\circ\text{C}$  to  $-173^\circ\text{C}$ ).

The deposition position was determined with a HPGe  $\gamma$ -detector via the 439.5 keV  $\gamma$ -line of  $^{202}\text{Tl}$  [5]. The associated deposition temperatures were compared to Monte Carlo simulations [6] utilizing the above-outlined experimental parameters including the negative temperature gradient measured in 1 cm steps. This ultimately led to a preliminary set of adsorption enthalpies of the deposited Tl species on fused silica.

## Results and discussion

The surface density of hydroxyl-groups on fused silica stationary phases is highly dependent on the temperature as well as the treatment time [7-8]. Presented here are the influence of two pretreatments of the stationary phase, i.e., 3 h at  $550^\circ\text{C}$  and 40 h at  $1000^\circ\text{C}$  (see Fig. 1).

For the pretreatment at  $1000^\circ\text{C}$ , the preliminary negative adsorption enthalpy was found to be  $-\Delta H_{\text{ads}}^{\text{SiO}_2}(\text{TlX}) = 90$  kJ/mol and is comparable with previous offline thermochromatography experiments *in vacuo* (i.e.,  $-\Delta H_{\text{ads}}^{\text{SiO}_2}(\text{Tl}) = 112(5)$  kJ/mol) [9], and theoretical predictions on a fully dehydroxylated fused silica surface (i.e.,  $-\Delta H_{\text{ads}}^{\text{SiO}_2}(\text{Tl}) = 80.9$  kJ/mol) [10]. However, this conclusion contradicts prior isothermal studies online *in vacuo* with a negative adsorption enthalpy of  $-\Delta H_{\text{ads}}^{\text{SiO}_2}(\text{Tl}) = 158(3)$  kJ/mol [11] and another online isothermal gas adsorption experiment in the continuum flow regime yielding  $-\Delta H_{\text{ads}}^{\text{SiO}_2}(\text{Tl}) = 197(3)$  kJ/mol [2].

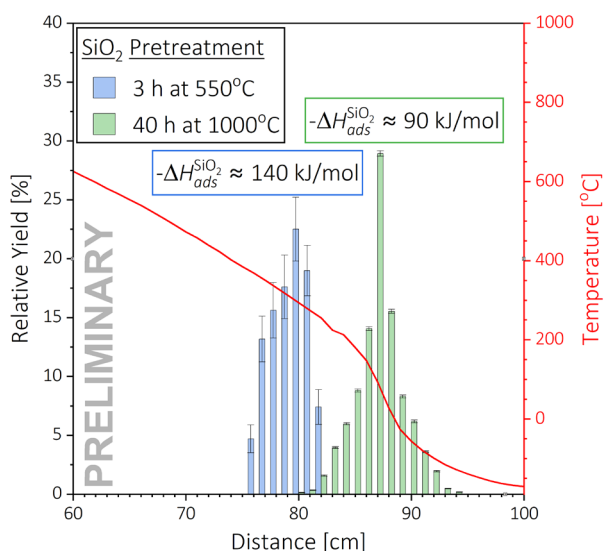


**Figure 1:** The preliminary internal chromatograms (blue and green bars; normalized to the associated individual total sum) resolved at 1 cm steps and the temperature profile (red line and right axis) as well as the preliminary negative adsorption enthalpies (color coded).

Further speculation regarding the chemical speciation of TI in the herein presented experiments is avoided as additional experiments are needed. These may include the influence of reducing or oxidizing gas impurities in combination with different surface pretreatments of the stationary phase. Ultimately, these experiments aim at reliably stabilize one or the other chemical species of TI under defined experimental conditions. Furthermore, the recovery of the deposited TI following its deposition during a thermochromatography experiment will be targeted. As the deposition of a more volatile chemical species of TI on the extensively pretreated fused silica column (i.e., 40 h at 1000°C) occurred where the temperatures decreased significantly as function of the chromatography column length ( $\approx 50^\circ\text{C}/\text{cm}$ ), a precise determination of the associated adsorption enthalpy is aggravated.

## Acknowledgements

This work was funded by the SNSF (project no. 20020\_196981).

## References

- [1] A. Serov et al. *Radiochim. Acta*, **101** (2013)
- [2] J. Wilson et al., *Inorg. Chem.* (under review) (2024)
- [3] J. Wilson et al., *LRC Annual Report 2022*, 3 (2023)
- [4] M. Witschi et al., *LRC Annual Report 2022*, 52 (2023)
- [5] M. Basunia, *Nucl. Data Sheets*, **143** (2017)
- [6] I. Zvara, *Radiochim. Acta*, **38** (1985)
- [7] L. T. Zhuravlev, *Colloid Surf. A*, **3** (2000)
- [8] Z. Yongheng et al., *J. Non-Cryst. Solids.*, **352** (2006)
- [9] B. Eichler et al., *Akademie der Wissenschaften Report*, ZfK-346 (1977)
- [10] M. Ilias et al., *Inorg. Chem.*, **61** (2022)
- [11] P. Steinegger et al., *J. Phys. Chem. C*, **9** (2016)

## The nature of lanthanoid impurities in highly pure U materials

M. Hofstetter (ETHZ, Spiez Laboratory & PSI), S. Röllin (Spiez Laboratory), P. Steinegger (ETHZ & PSI)

### Natural lanthanoids in uranium materials

Lanthanoid (Ln) patterns are of interest as it is possible to understand the underlying geologic processes responsible for rock and mineral formation by modification and fractionation of these patterns [1,2]. In geological terms, Lns are incompatible with the main silicate and rock forming phases in the earth mantle and the crust [1,2]. This leads to the accumulation of Lns in secondary magmatic phases and their fractionation from main phases. In rock, they are found selectively deposited in minerals according to their associated partition coefficients [2]. The electronic structures of Lns are generally very similar. However, redox-active Ce and Eu do not follow the general trend [3] as the reduction of  $\text{Eu}^{3+} \rightarrow \text{Eu}^{2+}$  and the oxidation of  $\text{Ce}^{3+} \rightarrow \text{Ce}^{4+}$  lead to particularly stable half-filled and empty *4f*-orbitals, respectively. This results in a higher affinity toward silicate phases and therefore to selective anomalies in the corresponding Ln patterns [4]. Lns are often found together with U and Th deposits because they share the most important chemical feature: being incompatible with silicate phases. For the deposition of U and Th, different mechanisms are responsible, which involve temperature, pressure, pH, redox potential, the presence of water and the carbon dioxide availability as well as stabilizing or precipitating ligands and cations [1,3-5]. Orogenesis is usually subjected to several stages, where initially formed ore deposits are remobilized and again deposited under various conditions, leading to a new modification of a present Ln pattern. Hence, this makes Ln patterns an almost unique fingerprint for individual U and Th ore deposits.

Nuclear forensic studies have already shown that the Ln patterns, caused by the geological environment, can be used to trace back U ore and U ore concentrates ("yellow cake") to the originating mine [6]. The processing of the U ore usually follows the procedure of leaching, solvent extraction, precipitation as sodium diuranate ( $\text{Na}_2\text{U}_2\text{O}_7$  / Yellow cake) or uranyl peroxide ( $\text{UO}_4$ ) and the final sintering to  $\text{UO}_2$ [6]. These processes can be seen as a step-by-step purification of the U material and a continuous removal of Ln impurities. However, nuclear forensic investigations employing advanced analytical techniques have shown, that – despite the decreasing concentration – the original pattern remained unaffected during these purification steps [6-8]. Determining 14 analytes (i.e., the Ln

elements) in U/Th materials is an advantage over other characterization methods, such as Sr and Pb isotopic ratios, which are easily disturbed making a geological tagging or sample matching ambiguous. Nevertheless, the outcome of Ln measurements may be matched to Sr and Pb isotopic ratios. The Lns, with their close chemical behavior toward U, lead to distinct results. Therefore, Ln patterns are considered as highly valuable analytes for sample characterization and specimen attribution in nuclear forensics [9].

### The lanthanoid pattern during conversion and enrichment of uranium

In natural U, the fissile  $^{235}\text{U}$  isotope is usually abundant with only 0.72%. Therefore, the isotope  $^{235}\text{U}$  needs enrichment when used for nuclear applications. To achieve this, the material must be converted in a form, which enables the isotope  $^{235}\text{U}$  to be physically separated from the other two abundant isotopes, i.e.,  $^{238}\text{U}$  and  $^{234}\text{U}$ . Industrially, this is conducted in the gas phase, mainly by using gas centrifugation or gas diffusion of sublimated (sp. 56.5°C)  $\text{UF}_6$  [10-12]. To convert the reduced and sintered U ore concentrate ( $\text{UO}_2$ ) into  $\text{UF}_6$ , the material is first reacted with HF to form  $\text{UF}_4$  and then further converted into  $\text{UF}_6$  using  $\text{F}_2$  gas. Prior to enrichment, the  $\text{UF}_6$  is typically purified by distillation. The final conversion process back to  $\text{UO}_2$  is a crucial step in nuclear fuel production. Besides the enrichment, it represents the last purification step in the production of low and highly enriched U materials.

Unfortunately, there is not too much information available about the behavior of Lns during conversion and enrichment because of two main reasons. Firstly, fuel producers are not very open to support research in this direction as they are reluctant to expose their manufacturing details. Secondly, all information regarding nuclear fuel and proliferation is considered as a matter of national security. Therefore, such data is usually treated as a company secret, or it is in general confidential. Nonetheless, in various documents it is stated, that exactly this final purification step removes the last chemical impurities in U materials, in particular Ln impurities. This is explained with the low volatility of trivalent Ln fluorides under the prevalent conditions during the conversion process (i.e., 100°C - 450°C in a flame reactor under an atmosphere containing 20% - 50%  $\text{F}_2$ ) [12]. So far, this seems to be correct, with one exception, namely Ce.

In many cases, the oxidation state  $Ce^{4+}$  is not included in volatility studies of the conversion process. Instead, it is mentioned, that tetravalent Ln fluorides decompose around  $400^{\circ}C$  as they are forming  $F_2$  and  $LnF_3$  upon sublimation. What is usually overlooked is the fact that  $CeF_4$  shows a by far higher chemical stability (decomposition at  $> 800^{\circ}C$ ) than all other Ln tetrafluorides. Compared to the other Lns,  $CeF_4$  is stable in the gas phase and observed to be slightly volatile at  $800^{\circ}C$  [12-13].

Furthermore, Vlastelic and Piro [13] obtained interesting results during HF digestion of geological reference material. When they digested several reference silicate materials, they observed a low volatility of various Ln fluorides (approx. 50 ng/g) below  $100^{\circ}C$  and under ambient pressure in aqueous HF solution. This proves that Ln fluorides may be slightly volatile even under mild conditions. Although the amount does not appear to be large, 50 ppb are well above the detection limit of sector field inductively coupled plasma mass spectrometry (sf-ICP-MS). Thus, further investigations are needed to clarify if Ln contaminations indeed survive the fluorination and enrichment processes and therefore might be still present in the enriched fuel pellet.

### The lanthanoid pattern in irradiated fuel

In nuclear fuel, another important source of Lns are fission products (FPs) produced during fuel irradiation. The thermal neutron-induced fission of  $^{235}U$  leads to a high yield of FPs within the mass ranges  $A = 85 - 105$  and  $A = 130 - 150$ . The second mass range covers the first half of the Ln elements and their neutron-rich isotopes. Within this range, a sufficiently high formation of stable Ln isotopes starts with  $^{139}La$  (6.35%) and drops until  $^{153}Eu$  (0.15%). Within this range, the most abundant and stable FPs are the isotopes of elements Ce, Nd and La. It is important to note that a few isotopes are only formed at very low yields, due to "shielding" by a stable isotope within the path of  $\beta$ -decay. The addition of FPs drastically increases the complexity of the Ln pattern, as it is modified with a non-natural ratio of stable isotopes in dependence of their corresponding fission yield as well as neutron capture cross sections [14].

Besides the FPs, fuel irradiation leads to the activation of U isotopes and other activation products. Typical activation pathways in irradiated fuel lead to  $^{236}U$ , as well as radioisotopes of Np, Pu and Am. These radioisotopes are important signatures to determine the source of the sample. If activation products are entirely absent, it can be assumed, that the U material is of natural origin. Meanwhile, the presence of activation products – even at very low amounts (ppt to ppq level) – are clear indicators for a reprocessing facility of spent nuclear fuel.

Lastly, fuel reprocessing is performed via dissolution and separation of FPs by solvent extraction. It is a key fact, that every industrial solvent is contaminated with trace elements, including Lns, which represents the third source of Ln contamination, that may be found in U materials.

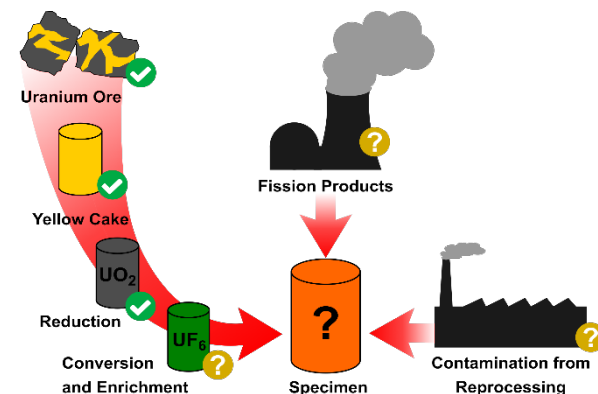


**Figure 1:** Today, the lanthanoid patterns in natural U materials are well-understood. However, the impact of enrichment, fuel irradiation and reprocessing remains unknown.

### Outlook

The sources of U material are very diverse and in some cases the mixing of different materials is commonly used to reach an intended material composition. Especially the mixed materials are very difficult to characterize and to draw meaningful conclusions. Therefore, it is essential to understand the whole U life cycle with all its conversion processes and associated types of potentially introduced contaminations as well as the vanishing effects on abundant traces. Overall, this knowledge helps us to a broader understanding of nuclear materials. Our first results are found in the following report [15].

### References

- [1] M. Wilson, *Igneous Petrogenesis*, Springer (2007)
- [2] M. R. Cicconi et al., *Magma Redox Geochemistry*, Wiley (2021)
- [3] E. Balboni et al., *App. Geochem.*, **87**, 84-92 (2017)
- [4] R. Holder et al., *Geochem., Geophys., Geosyst.*, **8**, 21 (2020)
- [5] J. Gonzalez-Estrella et al., *Env. Sc. and Techn.*, **54**, 3979-3987 (2020)
- [6] IAEA, TECDOC 1629 (2009)
- [7] J. Krajcık, et al., *Radiochim. Acta*, **104**, 471-479 (2016)
- [8] E. Keegan et al., *For. Sc. Int.*, **240**, 111-121 (2014)
- [9] H. Wood, *Sc. & Gl. Sec.*, **16**, 26-36 (2008)
- [10] I. Crossland, *Nuclear fuel cycle science and engineering*, Woodhead Publishing (2012)
- [11] V. Shatalov, et al., *Atomic Energy*, **90**, 224-234 (2001)
- [12] N. Chilingarov, et al., *J. Phy. Chem.*, **119**, 8452-8460 (2015)
- [13] I. Vlastelic et al., *Geostand. & Geoan. Res.*, **46**, 519-534 (2022)
- [14] J. Laurec et al., *Nuc. Data Sheets*, **111**, 2965-2980 (2010)

## Quantifying impurities in highly pure U materials

M. Hofstetter (ETHZ, Spiez Laboratory & PSI), S. Röllin (Spiez Laboratory), P. Steinegger (ETHZ & PSI)

### The lanthanoid sources in U materials

In nuclear forensic investigations lanthanoid (Ln) patterns are considered as highly valuable analytes for sample characterization and specimen attribution [1]. This is important as the original Ln pattern (ore) may be conserved during the purification of U ore. This is an advantage over other characterization methods, e.g., Sr and Pb isotopic ratios. Sr and Pb isotopic ratios are easily disturbed, making it challenging to match different U materials. However, within the U fuel production, the conversion and enrichment process is the last purification step, which is expected to completely remove all Ln impurities from the U material. The subsequent product is therefore described as a high purity U material without Ln traces. This is usually justified with the low volatility of trivalent Ln fluorides and the low stability of most tetravalent Ln fluorides [2].

### Fission/activation products in U material

Fission products (FPs) are very important factors because they have a significant influence on the corresponding Ln pattern in a U material. In general, the complexity increases with every reprocessing, enrichment and irradiation cycle [3].

The presence of FPs as well as activation products indicates a prior fuel irradiation and therefore non-natural isotopic ratios of Ln impurities. Additionally, the subsequent fuel reprocessing leads to a chemical contamination with Lns during solvent extraction as a result of the used chemicals and their respective impurities. According to Moody et al. [4] it can be assumed, that every reprocessing facility is using a different solvent to fuel ratio, thereby introducing a characteristic fraction of Ln impurities into the U material. To describe the analysed pattern, the result can be mathematically interpreted as a linear combination of all introduced patterns in a U material.

### Investigation of U material

To test our methods for the isolation of Np, Pu, and the Lns, we decided to subject a high purity uranyl nitrate sample to our separation process. In the first step, it was important to clarify (1) if the material is of natural origin, (2) if the material underwent enrichment or depletion, and, (3) if the material contains FPs or activation products as emerging during fuel irradiation.

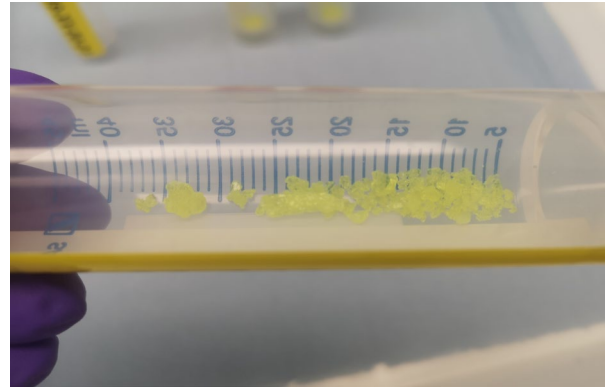


**Figure 1:** The investigated uranyl nitrate sample.

Our first results as obtained by sector field inductively coupled plasma mass spectrometry (sf-ICP-MS) showed, that the U material was partly depleted (0.3%  $^{235}\text{U}$  vs. 0.72% natural abundance). Therefore, the sample must have passed through at least one conversion and enrichment process, likely originating from the depleted tailings accumulated as waste during enrichment [2]. Additionally and together with the natural U isotopes (see Tab. 1), we clearly identified the U activation product  $^{236}\text{U}$  (0.002%). This was a first indicator that the investigated material was indeed irradiated and reprocessed prior to the enrichment process.

**Table 1:** Natural (\*) and produced U isotopes [at.-%] in the investigated uranyl nitrate as obtained with sf-ICP-MS.

Isotope	Composition [at %]	Uncertainty [at %]
U-238*	99.5570	0.0002
U-236	0.0020917	0.0000074
U-235*	0.4382	0.0002
U-234*	0.002724	0.000004

Due to the identification of  $^{236}\text{U}$ , we further tried to isolate Np and Pu radioisotopes, which were finally found at a concentration level of  $10^{-15}$  g/g (i.e., at the ppq-level; see Tab. 2). These findings underline the above-drawn conclusion of a fuel irradiation and a subsequent reprocessing. Secondly, the material must have undergone at least twice a conversion and enrichment process because it was once enriched prior to fuel irradiation and after reprocessing.

**Table 2:** Further actinides in the uranyl nitrate.

Isotope	Conc. [ $10^{-15}$ g/g]	Uncert. [ $10^{-15}$ g/g]
Np-237	160	80
Pu-239	53.5	4.9
Pu-240	1.9	0.5

From the isotopic ratio  $^{240}\text{Pu}/^{239}\text{Pu}$ , it is possible to obtain an impression of the purpose for which the U material was intended to be used. Because  $^{239}\text{Pu}$  can undergo activation to  $^{240}\text{Pu}$ , the ratio is indicative of the neutron flux prevalent within the reactor as well as the duration of irradiation. For the present case, a ratio of 0.035(10) was calculated, which indicates a strong and short irradiation because there was a considerable amount of  $^{239}\text{Pu}$  formed, but at the same time, the irradiation time was too short in order to breed it further to  $^{240}\text{Pu}$ . Such irradiation conditions are usually encountered in production schemes aiming at  $^{99}\text{Mo}$  or Pu. Another indicator is the ratio of  $^{240}\text{Pu}/^{239}\text{Pu}$ . A value below 0.08 is an indicator for a production targeting weapon grade Pu, which was indeed observed in herein presented case (0.077).

These preliminary findings rendered the sample an ideal testing material for the further investigation of its Ln impurities.

### Lns in depleted U material

In a second step, the sample was subjected to Ln isolation according to a previously developed method, which allows for Ln quantification in the lower ppb to ppt ranges [5]. This is approximately 1000 times more sensitive than previously described methods [6].

With this method, low contaminations of La, Ce and Nd in the lower ppb-level were found in the investigated sample (see Fig. 2). Unfortunately, all other isotopes of Ln elements vanished as a result of the background of the method.

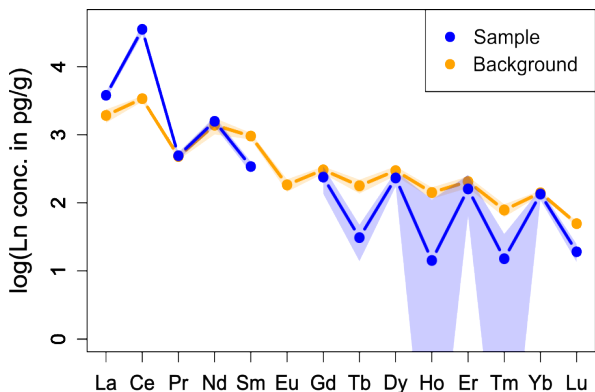


**Figure 2:** The lanthanoid pattern in the uranyl nitrate sample (blue) together with the method background (yellow).

$\text{Ce}^{3+}$  can easily undergo oxidation to  $\text{Ce}^{4+}$ , a state in which it shows similar chemical properties as U [7]. Thus, we suspect  $\text{CeF}_4$  to be slightly volatile during

enrichment conditions, leading to a contamination of Ce in enriched and depleted products of U. Moreover, a low volatility of Ln fluorides was observed in aqueous HF solutions of geological samples [7-9]. These results suggest that  $\text{CeF}_4$  is slightly volatile in the presence of hydrogen fluoride. Therefore, it can be assumed, that Ce behaves similarly during the conversion and enrichment process and shows a different behaviour compared to other Lns. This might in fact explain the contamination of Ce and other Lns in highly pure U materials. However, it is important to note that further investigations are needed to verify the effective source of the found Lns.

### Conclusion

These first results enabled us to uncover previously hidden traces of Lns in U material, which were impossible to detect previously. Unfortunately, the sample trace is very close to the method background, but showed a distinctive Ce signal. Even if the herein presented results do not represent a whole Ln pattern, it nevertheless enables first interpretations and the formulation of a hypothesis for the behavior of Lns during the conversion of  $\text{UO}_2$  to  $\text{UF}_6$ , and the subsequent enrichment of U materials: Within the Lns, Ce is the only element with a significantly higher stability in the tetravalent state ( $4f^0$  configuration). Together with the implied low volatility [7] of the Ln element in aqueous HF solutions, this might be the reason why traces of Ce survive the conversion and enrichment process

Overall, the complete interpretation of Ln patterns remains challenging due to various sources of Ln contaminations during processing of U materials (ore, fission, reprocessing). In continuation of this project, we are currently investigating more U materials in order to gain deeper insights into the nature of U materials and their trace contaminants. Uncovering further traces and influences in nuclear materials will allow us to further enhance our capabilities for sample characterization and attribution of nuclear materials.

### References

- [1] IAEA TECDOC 1529 (2007)
- [2] IAEA, TECDOC 1629 (2009)
- [3] K. Moody, Nuclear Forensic Analysis, CRC Press (2015)
- [4] M. Hofstetter et al., LRC Annual Report 2022, 14-15 (2023)
- [5] J. Krajčó et al., *Radiochim. Acta*, **104**, 471-479 (2016)
- [6] N. Chilingarov et al., *J. Phy. Chem.*, **119**, 8452-8460 (2015)
- [7] I. Vlastelic et al., *Geostand. & Geoan. Res.*, **46**, 519-534 (2022)
- [8] V. Shatalov et al., *Atomic Energy*, **90**, 224-234 (2001)

## From batch to flow electrolysis: The separation of $^{110m}\text{Ag}$

P. Dutheil (ETHZ & PSI), M. Heule (PSI), P. Steinegger (ETHZ & PSI), A. Vögele (PSI)

### Introduction

Chemical separation methods are a key to any radiochemist as they are essential for the analysis and provision of radionuclides. In agreement with earlier work, recent investigations have demonstrated that controlled-potential electrolysis (CPE) is a promising alternative technique to traditional radiochemical separation methods (e.g., ion-exchange, extraction chromatography, and precipitation or co-precipitation) [1-4]. CPE takes advantage of the reduction potential difference between elements to trigger a separation by selective electrodeposition. Therefore, it gives access to a different selectivity when compared to usual separation techniques. In addition, it also provides other advantages such as the possibility of preconcentration of the element of interest, no introduction of impurities (e.g., organic residues from chromatographic resins), high resistance to radiation damage, and direct preparation of thin sources for nuclear spectrometric measurements. However, CPE is typically carried out in batch mode, which brings certain operational inconveniences such as the difficulty of an electrolyte exchange, or a long electrolysis time. These can be circumvented using flow-through electrolysis with porous electrodes featuring a high surface area. This configuration allows for fast electrolysis upon a single pass through the electrode, enabling pre-concentration of the analyte from large volume samples with the possibility of easily rinsing the electrodes and exchange the electrolyte. Moreover, it can be readily integrated within more complex flow systems and coupled with classical separation techniques such as, for example, column chromatography. Although the concept of flow-through electrolysis is relatively old [5,6], only a few examples have been reported regarding the separation of radionuclides for, e.g., analysis [5] or production [6]. Therefore, a simple flow-through electrolyser was developed and evaluated for the separation of carrier-added  $^{110m}\text{Ag}$  from model solution containing  $^{110m}\text{Ag}$  and  $^{60}\text{Co}$  in 1M  $\text{HNO}_3$ , both relevant radionuclides in the context of routine sample analysis from nuclear power plants. The radioactive experiments were preceded by cold tests using natural Ag and Co.

### Experimental

All solutions were prepared from  $\text{AgNO}_3$  (99.8%, Merck),  $\text{Co}(\text{NO}_3)_2 \cdot 6\text{H}_2\text{O}$  ( $\geq 99\%$ , Fluka),  $\text{HNO}_3$

(suprapur, Sigma-Aldrich) and ultrapure water ( $18.2 \text{ M}\Omega\text{-cm}$ , Merck Millipore).

The working electrode (WE) of the electrochemical flow cell was built by packing pieces of a carbon fiber felt (PAN based, Fuelcell store) in a PE column. The platinum counter electrode (CE) and the  $\text{Ag}/\text{AgCl}/\text{KCl}$ -saturated reference electrode (RE) were placed in their respective separated compartments, both in contact with the solution using 1M  $\text{KNO}_3$  salt bridges to prevent side reactions at the CE, and  $\text{Cl}^-$  contamination from the RE. The potential of the working electrode was adjusted using a PGSTAT204 potentiostat (Metrohm Autolab). Samples were injected in the flow-cell using a simple flow system (see Fig. 1). All experiments were carried out at a flow rate of 1 ml/min.

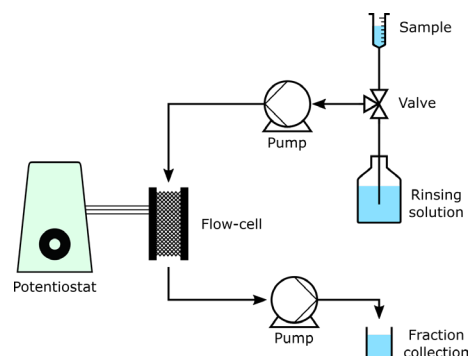


Figure 1: Setup used for flow electrolysis experiments

Yields of electrolysis were calculated from the concentrations of Ag in different fractions obtained during electrodeposition/electrodissolution cycles with different potentials applied to the WE ( $E_{app}$ ). All measurement of stable Ag and Co were carried out with an Agilent 5110 ICP-OES (Agilent Technologies, U.S.A.) calibrated externally for Ag (at 328.068 nm) and Co (at 238.892 nm) with a dilution of 1000 g/l certified calibration standards (TraceCERT, Sigma-Aldrich) in 2%  $\text{HNO}_3$ . The tracer  $^{110m}\text{Ag}$  was produced by neutron irradiation of natural  $\text{AgNO}_3$  at the SINQ-NAA facility of PSI.

### Results and discussion

The electrolysis yields obtained for the reduction of  $10 \mu\text{g}$  of  $\text{Ag(I)}$  to  $\text{Ag(0)}$  on the electrode are shown on Figure 2a. Quantitative reduction of  $\text{Ag(I)}$  is readily achieved at  $E_{app} \leq 0.1 \text{ V}_{\text{vsRE}}$ , whereas  $\text{Co(II)}$  cannot be electrodeposited in this potential range. The anodic dissolution yields were also characterized (see Fig. 2b)

and show that Ag can be fully recovered at  $E_{app} \geq 0.3$   $V_{vsRE}$ . The relationship of the reduction yield vs.  $E_{app}$  depends on the concentration of Ag, the flow-cell configuration (potential drop) and the flow rate. Therefore, a redetermination of the yields may be required if one of these parameters changes.

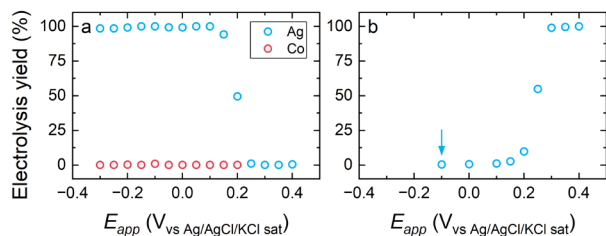


**Figure 2:** Flow electrolysis yield as function of  $E_{app}$  for (a) the electrodeposition of a sample containing 10 µg Ag and Co in 1M HNO<sub>3</sub> (10 ppm of Ag and Co) and (b) the anodic dissolution of 10 µg Ag in 1M HNO<sub>3</sub>; in (b), Ag was electrodeposited on the WE at the potential indicated by the arrow before anodic stripping. Error smaller than the displayed data points.

The adequate potential to use for separation can be selected from the data displayed in Figure 2. Accordingly, the separation was implemented by CPE of Ag at  $-0.2$   $V_{vsRe}$  whereas the later recovery occurred at  $0.8$   $V_{vsRe}$  together with an optimization of the rinsing volume. An example of a breakthrough profile as obtained with stable Ag and Co via CPE is shown in Figure 3. All Ag is reduced and retained in the column at  $-0.2$   $V_{vsRE}$  while Co is flushed out in the first fractions. Ag is subsequently oxidized and fully recovered upon switching the potential to  $0.8$   $V_{vsRE}$ .

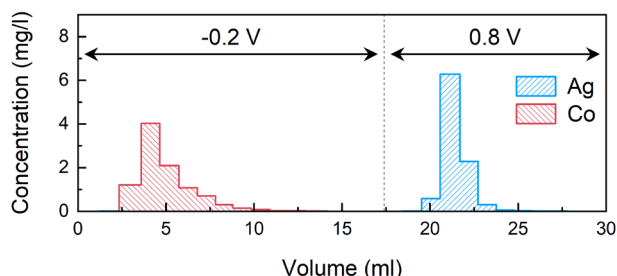


**Figure 3:** Breakthrough profile obtained for the separation of 10 µg Ag from 10 µg Co in 1M HNO<sub>3</sub> by flow electrolysis.

Further experiments were conducted with carrier-added  $^{110m}\text{Ag}$  and  $^{60}\text{Co}$  tracers. The silver carrier was added to match the concentration used previously during yield characterization. The  $\gamma$ -spectrum of the solution before separation features the characteristic  $\gamma$ -lines of both  $^{110m}\text{Ag}$  and  $^{60}\text{Co}$  (see Fig. 4a). The procedure used for separation was the same as the one used during the cold tests (see Fig. 3), with a larger

rinsing volume being necessary to ensure that all  $^{60}\text{Co}$  was flushed out of the flow cell. The first fraction collected at  $-0.2$   $V_{vsRE}$  (see Fig. 4b) contained only  $^{60}\text{Co}$  and did not show any traces of  $^{110m}\text{Ag}$ . All  $^{110m}\text{Ag}$  was present in the second fraction collected at  $0.8$   $V_{vsRE}$  (see Fig. 4c) confirming the successful separation of the two radionuclides.

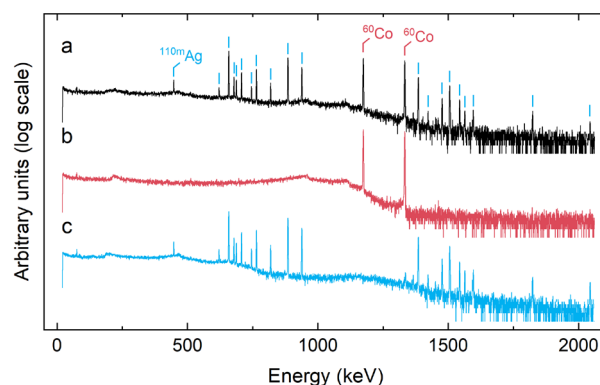


**Figure 4:**  $\gamma$ -spectra of a solution containing carrier-added  $^{110m}\text{Ag}$ , and  $^{60}\text{Co}$  in 1M HNO<sub>3</sub> (a) before, and after (b) the separation of Co and (c) the recovery of Ag by flow electrolysis.  $^{110m}\text{Ag}$ -related lines are marked in blue, and  $^{60}\text{Co}$ -related lines in red.

In some instances,  $^{110m}\text{Ag}$  was not fully recovered from the column by anodic oxidation. This is probably a consequence of AgCl formation due to Cl<sup>-</sup> impurities. In that case NH<sub>4</sub>SCN or NH<sub>3</sub> solutions may be used to recover  $^{110m}\text{Ag}$ .

These results show that flow electrolysis is a promising technique to carry out fast and routine separations of carrier-added radionuclides in aqueous phase. The method is now being explored further for applications in, e.g., routine radioanalytical separations. Additional investigations are also ongoing to check its applicability to no carrier-added conditions, where the electrode material has a bigger influence regarding the selectivity of the method.

## References

- [1] D. Lee et al., Atomic Energy Research Establishment report (1950)
- [2] K. Joerstad et al., *Anal. Chem.*, **52**, 672-676 (1980)
- [3] P. Dutheil et al., *LRC Annual Report 2021*, 12-13 (2022)
- [4] P. Dutheil et al., *LRC Annual Report 2022*, 12-13 (2023)
- [5] W. J. Blaedel et al., *Anal. Chem.*, **36**, 1245-1251 (1964)
- [6] T. Fujinaga et al., *CRC Critical Reviews in Analytical Chemistry*, **6**, 223-254 (1977)
- [7] R. Nakata et al., *Anal. Chim. Acta*, **149**, 67-75 (1983)
- [8] Y. Sugo et al., *ACS Omega*, **7**, 15779-15785 (2022)

# Development of an aerosol gas-jet degasser-unit for liquid-phase chemical studies with fission-products at SINQ

A. Pelletier (EPFL), P. Dutheil (ETHZ & PSI), R. Dressler (PSI), P. Steinegger (ETHZ & PSI)

## Introduction

Gas-Jet systems are facilities that allow for the mobilization and collection of fission products (FPs) from a fission source with the help of an aerosol flow passing through a target chamber. Examples of such systems can be found at the Ford Nuclear Reactor at the University of Michigan, United States [1], at the TRIGA research reactor in Mainz, Germany [2] or at the SINQ of PSI in the form of the recently recommissioned SINQ Gas-Jet facility [3]. The study of FPs serves basic research in radiochemistry (e.g., homolog studies with transactinide elements) or may be used for more applied topics related to the nuclear energy industry as well as to the radiopharmaceutical field, where for example  $^{99}\text{Mo}$  is used to produce  $^{99\text{m}}\text{Tc}$  for SPECT imaging [4]. The online dissolution of FPs as transported by an (aerosol) gas jet, has been achieved by different methods. One approach, i.e., the direct transfer of the aerosol particles into the solvent [5, 6], which has been used in the past, yields rather low recoveries [7]. Therefore, systems based on static mixer and degassing units have been developed. The static mixer is typically made of a high surface area material (e.g., quartz wool or PEEK wool) to ensure maximum contact time between the aerosol and the solvent. The aqueous and the gas phases are subsequently separated in the degassing stage, which may be a centrifuge [8–11], a membrane [12, 13], or a funnel [7, 14–16]. More sophisticated setups such as PILS [17] (Particles Into Liquid sampler) as well as denuders have also been used for that purpose [18–21]. The method presented here resembles the funnel degassing method described in [16]. It was the aim of this work to implement an efficient online dissolution system for FPs as transported by the SINQ Gas-Jet facility. Such a system will readily enable chemical studies with FPs in the liquid phase.

## Experimental

Neutrons are produced by spallation of a 590 MeV proton beam impinging on a lead cannelloni-target and moderated with ultrapure heavy water. More details are described in [3]. Thus thermalized neutrons collide with highly enriched  $^{235}\text{U}$  targets in the SINQ Gas-Jet target chambers embedded in the inner shielding outside of the moderator tank. Therein, the thermal neutrons induce fission leading to the aimed at FPs,

which partly recoil in the carrier gas above said targets (for details, refer to Ref. [3]). The non-volatile fraction of the FPs can be mobilized and transported to the radiochemistry laboratory by mean of the addition of aerosol particles (e.g., salt or metal aerosols). The entire SINQ Gas-Jet system is represented in Figure 1.

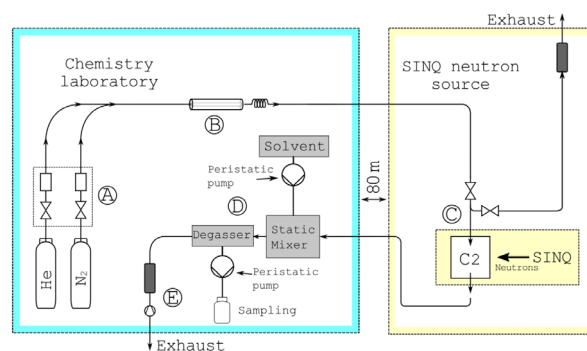


**Figure 1:** Scheme of the SINQ Gas-Jet system with the online dissolution; picture adapted from [3].

For the herein presented experiments, a He:N<sub>2</sub> carrier gas mixture (9:1 ratio, 0.7 L/min) was premixed in the laboratory from pressurized gas cylinders via the control system and was then passed through an oven (B in Fig. 1) containing KCl powder heated to  $\approx 678$  °C to produce aerosols. The aerosol loaded carrier gas was directed to the target chamber (C in Fig. 1) for the collection of FPs before being circled back to the radiochemistry laboratory. There, the FP-loaded aerosol underwent mixing (D in Fig. 1, details in Fig. 2) with a solvent (1M/0.1M HNO<sub>3</sub> or HCl), which was degassed to collect a liquid sample. The radionuclides-carrying aerosol is mixed with an acidic solvent on a frit before the mixture drops down in a funnel, while the gas exits through a joint at the side. The excess gas is directed to a trap (E in Fig. 1) to retain the potentially escaping radionuclides prior to being discarded through the exhaust.

Individual samples were collected for 15 min and subsequently measured on a HPGe  $\gamma$ -detector for 1 h (live time). All presented results were normalized to the integral of the proton beam current on the SINQ target during sampling. The efficiency of the online degasser has been derived by taking the ratio of the dissolved activity and the one of an offline dissolution from a quartz fiber filter (see [3] for details). The activities were determined by Genie2K (Cannberra) for 3 selected radionuclides, namely  $^{92}\text{Sr}$ ,  $^{94}\text{Y}$  and  $^{134}\text{I}$ .

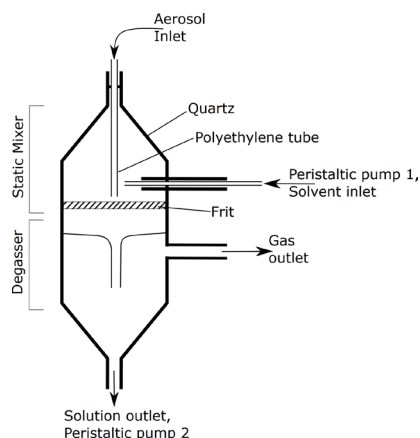


**Figure 2:** Mixer and Degasser newly implemented at the gas-jet facility.

These were easily identifiable, feature different chemical properties and do not belong to the same peak in the mass distribution of FPs.

## Results and Discussion

Different experiments were carried out to characterize the effects of various parameters on the dissolution efficiency. For example, the influence of the solvent flow at the inlet was investigated by changing the speed of the peristaltic pump, while maintaining all other parameters constant (e.g., inlet gas flow and target chamber pressure). Furthermore, the solvent type and concentration was altered. All results are presented in Figures 3 and 4.

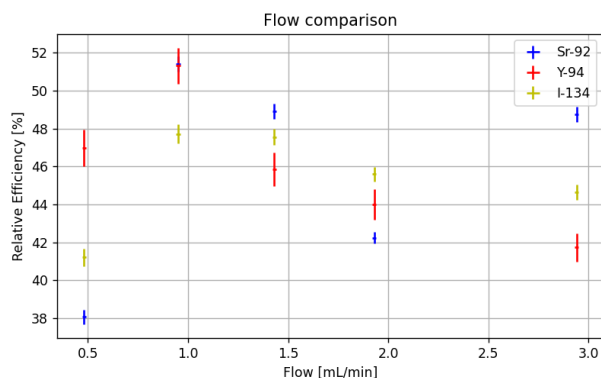


**Figure 3:** Evolution of the relative efficiency with the solvent flow at the inlet of the degasser unit.

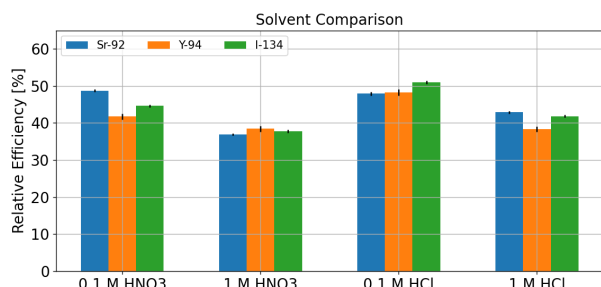


**Figure 4:** Variation of the relative efficiency as a function of the HCl and HNO<sub>3</sub> concentration.

In general, dissolution efficiencies of 40% to 50% were obtained with the herein presented setup. This is sufficiently high to enable online liquid-phase experiments, even at low flow rates.

The behavior of the relative efficiency as a function of the solvent flow at the inlet shows a maximum at 1 ml/min, while a drop is observed at lower and higher flow rates. Further measurements are needed to clarify the ambiguity of the results. The acid concentration seems to have an impact on the dissolution efficiency, with higher concentrations collecting less activity. This may be explained by an increase of viscosity at higher concentrations, thus, leading to an inferior wetting of the frit and therefore diminishing chances of catching radionuclides at high molarity [22].

The successful implementation of this mixer/degasser unit allows for online liquid phase studies with short-lived FPs at the SINQ Gas-jet facility. Future experiments may address the influence of all experimental parameters in more detail.

## References

- [1] K. Rengan et al., *J. Rad. Nuc. Chem.*, **98**, 255-263 (1986)
- [2] M. Eibach et al., *Nuc. Inst. and Met. in Ph. Res.*, **613**, 226-231 (2010)
- [3] G. Tiebel et al., *Nuc. Inst. and Met. in Ph. Res.*, **1041**, 167360 (2022)
- [4] P. H. Liem et al., *Prog. in Nuc. En.*, **82**, 191-196 (2015)
- [5] K. Kosanke et al., *Nuc. Inst. and Met. in Ph. Res.*, **115**, 151-155 (1974)
- [6] K. Kosanke et al., *Nuc. Inst. and Met. in Ph. Res.*, **124**, 365-374 (1975)
- [7] H. Bruchertseifer et al., *Radiochim. Acta*, **47**, 41-46 (1989)
- [8] K.-H. Hellmut et al., *Nuc. Inst. and Met. in Ph. Res.*, **125**, 99-104 (1975)
- [9] K. Brodén et al., *Nuc. Inst. and Met. in Ph. Res.*, **195**, 539-542 (1982)
- [10] H. Persson et al., *Radiochim. Acta*, **48**, 177-180 (1989)
- [11] G. Skarnemark et al., *Solvent Extraction and Ion Exchange*, **37**, 232-244 (2019)
- [12] J. Nilssen, "Investigations into new degasser technology for sisak", Master thesis (2009)
- [13] K. Ooe, et al. *Jour. of Radioana. and Nuc. Chem.*, vol. 303, pp. 1317-1320 (2015)
- [14] N. Trautmann et al., *Inorganic and Nuclear Chemistry Letters*, **11**, 729-735 (1975)
- [15] G. Skarnemark et al., *Nuc. Inst. and Met. in Ph. Res.*, **171**, 323-328 (1980)
- [16] Z. Szegłowski et al., *Radiochim. Acta*, **51**, 71-76 (1990)
- [17] R. Weber et al., *Aerosol Science & Technology*, **35**, 718-727 (2001)
- [18] C.-J. Tsai et al., *Journal of the Air & Waste Management Association*, **53**, 1265-1272 (2003)
- [19] D. A. Orsini et al., *Atmospheric Environment*, **37**, 1243-1259 (2003)
- [20] Z. Večera et al., *Proceedings of the 13th WSEAS international conference on Mathematical and computational methods in science and engineering*, 271-276 (2011)
- [21] P. Bartl et al., *Nuc. Inst. and Met. in Ph. Res.*, **1055**, 168500 (2023)
- [22] A. Rout et al., *J. Sol. Chem.*, **47**, 373-386, (2018)

## Preparation of natural hafnium samples for the production of $^{179}\text{Ta}$

P. Albrecht (ETHZ & PSI), Đ. Cvjetinović (PSI), P. Grundler (PSI), D. Schumann (PSI)

### Introduction

$^{180}\text{Ta}$  is a remarkable isotope: the ground state decays with a half-life of 8.15 hours whereas  $^{180\text{m}}\text{Ta}$  is quasi stable with a half-life longer than  $7 \times 10^{15}$  a. Since the exact stellar origin is unknown with three possible nucleosynthesis processes, it is a rather interesting radionuclide in astrophysics. One production route is the decay of excited  $^{179}\text{Hf}$  to  $^{179}\text{Ta}$  and subsequent neutron capture to  $^{180\text{m}}\text{Ta}$ . In order to correctly assess this reaction path, good cross-section data of  $^{179}\text{Ta}(n, \gamma)^{180\text{m}}\text{Ta}$  is needed.

As a semester project (ETHZ-EPFL-PSI master in nuclear engineering), a suitable procedure for the production of the needed target material  $^{179}\text{Ta}$  by proton irradiation via  $^{180}\text{Hf}(p,2n)^{179}\text{Ta}$  is investigated. The isotope was already produced earlier [1], but the irradiated Hf foil could not be dissolved completely due to unexpected partial oxidation. In this study, the irradiation of hafnium metal foil is repeated and compared to directly using hafnium oxide as target material for the irradiation.

### Experimental

#### Sample Preparation and Proton Irradiation

The samples need to be placed in special aluminium capsules shown in Figure 1 before being irradiated in the IP2 target station at PSI. The metal foil can be



Figure 1: Aluminium capsule with irradiation target inside.

directly used whereas the oxide powder first needs to be pressed to a disk: The powder is filled into a pressing chamber shown in Figure 2. A shaft is placed on top of the powder and pressed down in the pressing station for several seconds as shown in Figure 3. After the pressing, the oxide disk is placed inside an aluminium capsule shown in Figure 4. Finally, the capsule is closed by putting an aluminium cover and flanging it together (Figure 5).

The used  $^{180}\text{Hf}$ -metal foil disk had a thickness of 0.125 mm, a mass of 45 mg and a diameter of 6 mm.



Figure 2: Filling of powder into pressing chamber.

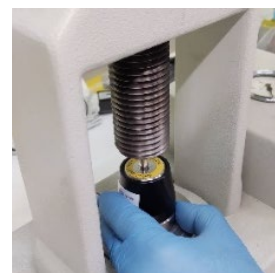


Figure 3: Pressing of the powder to a disk.



Figure 4: Pressed oxide disk.

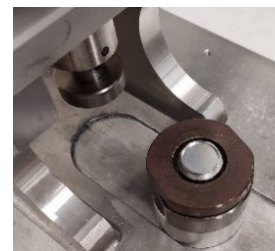


Figure 5: Airtight closing of the aluminium capsule.

According to [2] the metal foil has a purity of 97.0 % Hf with Zr impurities of 2.8 %. Additionally, it contains some other elements which are listed in Table 1. The final pressed  $^{180}\text{Hf}$ -oxide disk had a mass of 37 mg. The oxide powder from [3] has a purity of 99.995 % with less than 0.15 % Zr.

Table 1: Hafnium metal foil impurities. The metal foil has a purity of 97.0 % Hf and other elements listed here.

element	content
Zr	2.8 %
O	150 ppm
Fe, Ta	$\leq 100$ ppm
Nb, Cr, W, Cu	$\leq 50$ ppm
Al, C	30 ppm
Ti	25 ppm
N, Mg, Mo	$\leq 10$ ppm
U	0.5 ppm

The Injector II cyclotron at PSI delivers a 72 MeV proton beam of which a portion is available at the IP2 target station for radionuclide production. To bring the proton energy down to the required 20 MeV for the  $^{180}\text{Hf}(p,2n)^{179}\text{Ta}$  reaction, a 2.8 mm niobium degrader was placed in front of the target capsule. The prepared samples were irradiated for ten minutes. After the analysis of those two samples, more samples were

irradiated for one hour and eight hours for later use. The details of the irradiation are shown in Table 2.

**Table 2:** Hafnium target irradiations. Proton beam with 72 MeV and niobium degrader of 2.8 mm to reach 20 MeV.

disk ( $\phi$ : 6 mm)	amount [mg]	irradiation data (@20 MeV)	dose rate at 3 cm distance
Hf foil	45 mg	10 min, 50 $\mu$ A, (03.11.2023)	225 mSv/h (03.11.2023)
Hf foil	45 mg	1 h, 50 $\mu$ A, (29.11.2023)	62.5 mSv/h (01.12.2023)
Hf foil	45 mg	8 h, 50 $\mu$ A, (12.12.2023)	—
Hf foil	45 mg	8 h, 50 $\mu$ A, (18.12.2023)	—
Hf foil	45 mg	8 h, 50 $\mu$ A, (19.12.2023)	—
HfO <sub>2</sub>	37 mg	10 min, 50 $\mu$ A, (03.11.2023)	185 mSv/h (03.11.2023)
HfO <sub>2</sub>	40 mg	1 h, 50 $\mu$ A, (29.11.2023)	28.5 mSv/h (01.12.2023)
HfO <sub>2</sub>	40 mg	8 h, 50 $\mu$ A, (11.12.2023)	—

### $\gamma$ -ray Spectroscopy

The  $\gamma$ -ray spectra of the two samples that were irradiated for 10 minutes were measured for 1 hour with a HPGe detector one week after the irradiation (10.11.2023) to quantify the activities of the produced radionuclides. A more detailed measurement of 24 hours was performed for the metal foil sample on 23.11.2023 and the oxide sample on 29.11.2023 under the same geometry conditions. To find the isotopes corresponding to the energy lines, the nuclear data website [4] was used. For longer irradiation times a longer waiting time is needed until the dose rate is low enough to easily handle the samples. Therefore, only the samples with 10 minutes irradiation time could be measured and are discussed at this point in time.

### Solubility Tests

For the separation of Ta from Hf, it is required to dissolve the sample. To see if the metal or the oxide is more suited, solubility tests with non-irradiated samples using different chemicals were conducted. The oxide powder was used directly but the Hf metal disks were cut into pieces of approximately 11-12 mg before using them for individual tests. The test configurations and results are listed in Table 4 and Table 5 in the results section.

## Results and Discussion

### Spectrum Analysis

The  $\gamma$ -ray spectra of Hf metal foil and oxide powder are shown in Figure 6. Both spectra show the typical energy lines for <sup>177</sup>Ta, <sup>172</sup>Hf, <sup>175</sup>Hf, <sup>179m2</sup>Hf, <sup>91m</sup>Nb, <sup>92m</sup>Nb and <sup>95</sup>Nb. The metal foil sample shows some other energy lines corresponding to <sup>48</sup>V, <sup>87</sup>Y, <sup>88</sup>Y, <sup>89</sup>Zr and <sup>56</sup>Co which come from activation of the impurities in the metal (see Table 1). The two peaks at 584 keV and 610 keV only

measured in the oxide powder sample match respectively the lines for <sup>208</sup>Tl and <sup>214</sup>Pb and therefore belong to the natural background. There are some peaks appearing in both spectra that could not be clearly assigned to any isotopes. It is important to mention that the measured electron-positron annihilation peak is at (511  $\pm$  1) keV while the <sup>40</sup>K peak is measured at (1462  $\pm$  1) keV indicating a possible energy drift at higher energies. Taking this drift into account, the peaks at 1121 keV, 1766 keV and 2016 keV

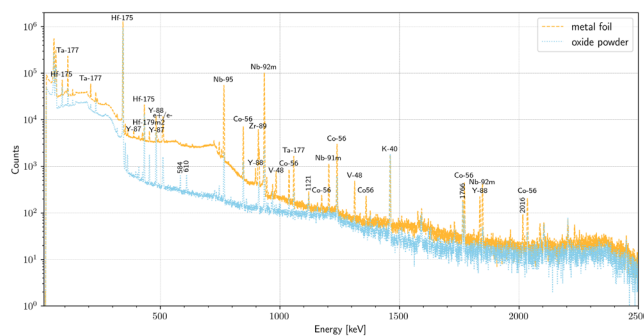


**Figure 6:** Spectra of the 24 h measurement for both samples.

visible in both samples could be from natural background radiation (<sup>214</sup>Pb). Since <sup>179</sup>Ta has no gamma lines, it cannot be directly measured with gamma spectroscopy, but it should be related to the amount of <sup>177</sup>Ta produced. The spectra of the one-hour measurement were analysed using the InterWinner 7.1 software, and the activity was back calculated to the end of irradiation. The results of irradiation are summarized in Table 3.

**Table 3:** <sup>177</sup>Ta activity after 10 minutes of proton irradiation.

hafnium target	<sup>177</sup> Ta activity	<sup>177</sup> Ta amount
45 mg Hf metal (97.0 % Hf, 2.8 % Zr)	15.84 MBq	1.36 ng
37 mg HfO <sub>2</sub> (99.995 % Hf, <0.15 % Zr)	11.78 MBq	1.01 ng

The identified radionuclides in comparison to the results reported in [1] are shown in Table 4. In the table, only the energy for the highest intensity gamma line is shown but for the analysis all lines with an intensity of at least 1 % were checked. Note that <sup>179</sup>Ta has no  $\gamma$ -ray line so the energy written here is the x-ray energy line. Many of the listed isotopes are not produced in large enough quantities in this short irradiation times and therefore are not visible. Some isotopes were not measured in the previous experiment because they probably had decayed by the time the measurement was done, 7 months after irradiation.

The spectra indicate niobium, zirconium, hafnium, and tantalum in both samples. Most of the radionuclides of these elements have a short half-life such that they are already decayed after waiting for the dose rate to be low enough. The only relevant are the niobium isotopes <sup>91m</sup>Nb, <sup>92m</sup>Nb and <sup>95</sup>Nb with a half-life of 60.86 days, 10.15 days, and 34.99 days respectively. The additional

isotopes to be removed from the metal foil which have a long enough half-life to be still present after the cool down of the dose rate are  $^{88}\text{Y}$  with a half-life of 106.6 days and  $^{56}\text{Co}$  with 77.2 days. Those are produced from impurities in the metal such as strontium and iron. The spectrum of the irradiated oxide shows no additional isotopes.

**Table 4:** Produced isotopes in comparison to the data in [1].

Isotope	$T_{1/2}$ * [days]	$E_{\text{literature}}$ [keV]	$E_{\text{foil}}$ [keV]	$E_{\text{oxide}}$ [keV]
$^{179}\text{Ta}$	664.3	55.79	—	—
$^{177}\text{Ta}$	56.56	112.9498	113	113
$^{175}\text{Hf}$	70	343.4	343.4	343.8
$^{179\text{m}2}\text{Hf}$	25.05	453.43	454.1	454
$^{181}\text{Hf}$	42.39	482.182	482.5	482.5
$^{172}\text{Lu}$	6.7	1093.657	—	—
$^{173}\text{Lu}$	485.45	272.105	—	—
$^{174\text{m}}\text{Lu}$	142	44.697	—	—
$^{177}\text{Lu}$	6.65	208.3664	—	—
$^{88}\text{Zr}$	83.4	392.87	—	—
$^{88}\text{Y}$	106.63	1836.063	1837.2	—
$^{95}\text{Nb}$	34.99	765.794	766.1	—
$^{57}\text{Co}$	271.74	122.0614	—	—
$^{58}\text{Co}$	70.86	810.775	—	—
$^{65}\text{Zn}$	243.93	1115.546	—	—
$^{54}\text{Mn}$	312.2	834.848	—	—
$^{89}\text{Zr}$	3.27	—	909.80	—
$^{91\text{m}}\text{Nb}$	60.86	—	1205.5	1205.5
$^{92\text{m}}\text{Nb}$	10.15	—	1848.5	1848.7
$^{87}\text{Y}$	3.33	—	484.81	—
$^{56}\text{Co}$	77.24	—	847.4	—
$^{48}\text{V}$	15.97	—	984.16	—

\*The half-life data are from [4]. If no peak was found, the entry is marked with a dash. The six isotopes at the bottom of the table were not reported in [1].

### Sample solubility

Table 5 and Table 6 show the experimental conditions and results of the solubility tests. The Hf metal foil is easily dissolved by hydrofluoric acid (HF).

**Table 5:** Solubility test for Hf metal.

solvent	amount of metal	T [°C]	dissolved (time)
1 ml 1 M HF	11.25 mg	RT	yes (1 s)
1 ml 10 M HF	11.25 mg	RT	yes (1 s)
1 ml 10 M HCl	11.25 mg	RT	no (4 weeks)
1 ml 10 M HNO <sub>3</sub>	11.25 mg	RT	no (4 weeks)
1 ml conc. H <sub>2</sub> SO <sub>4</sub>	11.25 mg	RT	slowly (14 days)

The HfO<sub>2</sub> could not be dissolved by any of the tested chemicals. In [5] it is mentioned that it can be slowly dissolved in HF and in hot sulfuric acid, however, this did not work in the here tested configurations. The boiling point of sulfuric acid is 337 °C, so, in principle it would be possible to try even higher temperatures but, due to the limited thermal stability of the plastic tubes that were used so far this was not possible.

Since wet chemistry is the better and preferred approach for chemical separation of radioactive materials, the non-solubility of the HfO<sub>2</sub> is the biggest

problem if this target material is chosen or the metal foil oxidizes during irradiation. Fortunately, the preliminary tests showed that the metal foil is easily dissolved in HF. This was confirmed by the easy dissolution in 1 M HF of the 10 minutes irradiated metal foil when it was tested one month after the irradiation. There was also no oxidation layer forming that could impact the solubility of the disk. Therefore, the metal is more suitable for post-processing following the sample irradiation.

**Table 6:** Solubility test for HfO<sub>2</sub> oxide powder.

solvent	amount of oxide	T [°C]	dissolved (time)
3 ml 8 M HF	10.4 mg	RT	no (4 weeks)
3 ml 8 M HF & 1-14 ml 5 M NaOH	10.4 mg	RT	no (4 weeks)
3 ml conc. H <sub>2</sub> SO <sub>4</sub>	17.1 mg	RT	no (4 weeks)
3 ml conc. H <sub>2</sub> SO <sub>4</sub>	17.1 mg	150	no (50 min)
5 ml NH <sub>3</sub>	31.6 mg	RT	no (4 weeks)
2 ml 5 M NaOH	9.7 mg	RT	no (4 weeks)
3 ml 5 M NaHSO <sub>4</sub>	9.3 mg	RT	no (4 weeks)
3 ml 5 M NaHSO <sub>4</sub>	9.3 mg	80	no (1 h)
2 ml 5 M NaHSO <sub>4</sub> & 2 ml 5 M HF	6.4 mg	RT	no (4 weeks)

### Outlook

The samples that were irradiated for 1 h and 8 h need a longer cool down period for easier handling. Therefore, as a first next step, the separation method described in [1] will be tested on the hafnium metal sample that was irradiated for 10 min. Next, different resins for the column separation will be tested using non-irradiated hafnium metal samples followed by hot column runs using the 1 h irradiated metal foil. Once an optimal column setup is found, one of the 8 h irradiated samples will be processed and its  $^{179}\text{Ta}$  content measured. This should result in a larger  $^{179}\text{Ta}$  amount being produced compared to [1] since the irradiation was performed in an airtight capsule minimizing sample oxidation. In parallel, the solubility test of the oxide powder with H<sub>2</sub>SO<sub>4</sub> will be repeated for a longer heating period and possibly higher temperatures.

### References

- [1] Ruchi Garg et al., Physical Review C, 107(4) (2023)
- [2] GoodFellow Hafnium metal disk, <https://www.goodfellow.com/de/p/hf00-fl-000210/hafnium-foil> (visited on Oct. 13, 2023)
- [3] abcr Hafnium(IV) oxide, [https://abcr.com/ch\\_de/ab120581](https://abcr.com/ch_de/ab120581) (visited on Oct. 13, 2023)
- [4] S.Y.F. Chu, et al., Database WWW Table of Radioactive Isotopes, (Feb. 28, 1999), <http://nucleardata.nuclear.lu.se/toi/> (visited on Oct. 13, 2023)
- [5] Hafnium oxide properties, [https://www.chemicalbook.com/ChemicalProductProperty\\_EN\\_CB5737990.htm](https://www.chemicalbook.com/ChemicalProductProperty_EN_CB5737990.htm) (visited on Oct. 13, 2023)

## <sup>32</sup>Si activity measurements at IRA for the SINCHRON project

Y. Nedjadi (IRA), M. T. Durán (IRA), Đ. Cvjetinović (PSI), M. Veicht (EPFL & PSI), D. Schumann (PSI), C. Bailat (IRA)

### Introduction

SINCHRON is a joint project aiming at the determination of the half-life of <sup>32</sup>Si, with the partners Physikalisch-Technische Bundesanstalt Braunschweig, Germany (PTB) and Institut de radiophysique, Switzerland (IRA) being responsible for the activity determination. The activity standardisations of various <sup>32</sup>Si solutions prepared by PSI for the SINCHRON collaboration and the respective stability studies are completed and published [1-2].

At the June 2023 SINCHRON collaboration meeting, it was decided that the IRA would standardise the new <sup>32</sup>Si solution, produced by PSI from seven proton-irradiated vanadium disks. Given that this hexafluorosilicate solution is the final solution with which the participants will determine the half-life, and in view of the chronic problems of stability or prediction of the natural silica content of previous solutions, it was resolved that it should be pre-tested by the IRA before planning the final phase of activity and mass measurements.

### Experimental

At the end of June 2023, PSI sent IRA 1 g of the final radioactive hexafluorosilicate acid (H<sub>2</sub>SiF<sub>6</sub>) solution. This solution, designated M32Si7 here, is a 2.2-fold dilution of what PSI refers to as Master solution 2, produced from another batch of proton-irradiated vanadium disks. It is assumed to be free of traces of tritium but contains traces of <sup>125</sup>Sb (10<sup>-7</sup> activity ratio relative to <sup>32</sup>Si). IRA standardised it using two techniques: TDCR and the CIEMAT-NIST method (CNET).

The solution was dispensed with a pycnometer to 11 scintillation vials, prefilled with 14.5 mL of Ultima Gold (UG) to which aliquots of about 1 mL of 0.5 M HCl were then added to make 6.5%-v/v aqueous fractions. The scintillation vials were made of HDPE to prevent adsorption of <sup>32</sup>Si. Four of the HDPE-vials contained only UG and aliquots of the radioactive solution, while the others were quenched with carbon tetrachloride (CCl<sub>4</sub>) volumes ranging from 30 to 240 μL for the quenching measurement. Each vial was shaken for two minutes with a vortex mixer, then centrifuged at 15 rpm for three minutes to recover droplets from the cap and walls. For the comparative stability study, we also prepared four additional samples, two without

hydrochloric acid supplementation, and two with demineralized water in an amount equal to that of the radioactive deposit, which were agitated and centrifuged like the rest.

The four unquenched sources were measured by defocusing, varying the focusing voltage between 560 and 320 V in 40 V steps, and by optical filtering with 15 self-adhesive films of varying optical density. The seven HDPE-vials, with varying volumes of CCl<sub>4</sub>, were measured at a focusing voltage of 560 V.

For the CNET measurements, eleven quenched tritium sources were prepared. An IRA tritium standard was used for these liquid scintillation sources, with UG and a 6.5%-v/v aqueous fraction (HCl 0.5 M ultrapure). The quenching agent, CCl<sub>4</sub>, was added in multiple volumes of 30 μL. These vials were measured to establish the calibration curve required for the CNET method. This quenched set was in HDPE geometry.

Two sets of CNET measurements (each at two cycles) of the <sup>32</sup>Si and tritium vials were made over one week with the TriCarb 2700TR. All these samples were then measured once a week for three months on the same TriCarb to monitor source stability.

### Results and discussion

As shown in figure 1, TDCR measurements of M32Si7 activity show superb consistency (less than 0.1% dispersion between values obtained by defocusing, optical filtering or quenching), and the mean TDCR deviates by less than 0.07% from the CNET mean when the kB value is 0.0075 cm/MeV. The mean TDCR and CNET activity concentration is 113.87(34) kBq/g (k = 1), at the reference date of 10 August 2023 at 12:00 UTC.

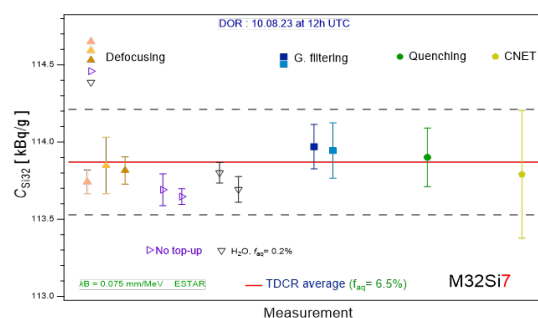


**Figure 1:** TDCR and CNET activity measurements of the M32Si7 solution. The red line is the arithmetic average of all TDCR measurements of samples with HCl 0.5 M top-up (f<sub>aq</sub> = 6.5 %).

We also monitored three samples: one with a hydrochloric acid top-up, one with a water addition equal in volume to the radioactive deposit, and a third without any top-up. They were measured approximately every four weeks using the TDCR defocusing method. These measurements confirm the observation, established by the IRA in previous studies, that only the sample with hydrochloric acid top-up remains stable over the long term. The CNET monitoring of the samples with hydrochloric acid top-up (see figure 2) also confirms the long-term stability of samples in this matrix.

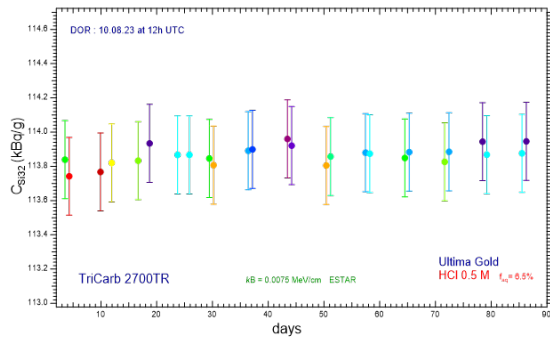


**Figure 2:** Variations in activity concentration of M32Si7 in HDPE vials over time.

IRA measurements of the latest  $^{32}\text{Si}$  solution produced by PSI confirm its amenability to produce stable LS samples for the final measurement of this nuclide's half-life.

### Acknowledgements

This project is funded by the Swiss National Science Foundation (SNSF) as part of SINCHRON (No. 177229) and received additional financial support from the European Union Horizon 2020 program under Marie Skłodowska-Curie grant agreement No. 701647.

### References

- [1] Y. Nedjadi et al., Applied Radiation and Isotopes **202**, 111041 (2023)
- [2] K. Kossert et al., Applied Radiation and Isotopes **202**, 111042F (2023)

# Thermosublimatographic study of tellurium evaporation from lead-bismuth eutectic melts

V. Zobnin (UniBe & PSI), L. Mössinger (Universität Hamburg), J. Neuhausen (PSI), R. Eichler (PSI & UniBe)

## Introduction

Lead-alloy-cooled fast reactors (LFRs) are considered as one of the approaches for the fourth-generation nuclear systems. These fast reactors can effectively transmute long-lived minor actinides via fission due to favorable cross-sections with fast neutrons. Subcritical accelerator driven LFRs, in which the coolant also acts as a spallation target for a high-energy proton beam, have improved capabilities to "burn" minor actinides compared to critical reactors.

A variety of radionuclides are formed in the liquid metal coolant due to neutron activation of its components and because of spallation reactions and forced fission of nuclei under a high energy proton beam, as demonstrated in the MEGAPIE project [1]. The primary concern with radioactive impurities relates to volatile elements that enter the cover gas. Understanding their volatilization is crucial for calculating doses during reactor maintenance, for developing cover-gas purification techniques as well as for the analysis of the consequences of accident scenarios.

Our study focuses on tellurium, a volatile element whose isotopes form by spallation and high energy fission of the liquid metal coolant in the spallation zone, due to stable impurity activation in the liquid metal or can enter the coolant by release from failing fuel elements. Understanding tellurium chemistry in liquid metal coolants also serves to enhance the knowledge on a contaminant relevant for LFRs — polonium the heavy homologue of tellurium. In continuation of earlier work [2], we use the method of thermosublimatography to reveal the speciation of tellurium in the gas phase over an LBE melt.

## Experimental

Samples of LBE doped with Te (mole fraction  $x_{Te} \cong 0.008$ ) were prepared as described in [2]. For the thermosublimatographic method, we used a tube furnace with a negative temperature gradient ( $-15$  K/cm) and a gas supply system consisting of a mass flow controller and a drying column or humidifier for experiments in dry or moist conditions, respectively. After the furnace, a charcoal trap was inserted to prevent radioactivity escaping the setup. A dew point meter (Michell Easidew) was used to monitor the water vapor content.

Experiments were performed in columns of fused silica and stainless steel 316L ( $\varnothing_{in} = 5$  mm). The distribution of Te over the column was measured with an HPGe-detector and a 1 cm lead collimator, using the 159 keV photopeak of  $^{123m}\text{Te}$ .

In an ideal case, gas phase species evaporated from the sample condense at a certain temperature, which appears as a well-defined deposition peak in the column scan profile. The relationship between deposition temperature, experimental parameters, and standard thermodynamic data of the sublimation/deposition equilibrium of the chemical compound involved can be expressed by (see [3] for more details) assuming ideal-gas behaviour:

$$\ln \frac{mRT_0}{v_0 T M p_0} = -\frac{\Delta H_{subl}}{RT_d} + \frac{\Delta S_{subl}}{R} \quad (1)$$

Experiments were conducted at a flow of 50 mL/min of He (5.0 grade) with 60 minutes heating of the sample in a stainless-steel boat. In experiments involving consecutive heatings, quartz columns with measured Te distribution after experiment in dry inert conditions were heated for a second time for 3 to 5 hours under the same conditions, but without a sample boat, to observe the changes in the Te distributions over time. Experiments in oxidative and reducing atmospheres were also performed. In oxidative conditions, 2% of oxygen was added to the helium. In reducing conditions, 10% hydrogen was added to the carrier gas. Scanning electron microscopy with the EDX method was used to study the chemical composition of depositions observed in the columns after experiments.

## Results and discussion

In the previous report [2], two depositions at around 600 °C and 300 °C were observed in thermosublimatographic experiments with Te-doped LBE in dry He flow. The deposition at 600 °C was attributed to PbTe using eq. 1, while no suitable match could be found for the second deposition using available thermodynamic data for known Te species, including elemental Te and Te<sub>2</sub>. In humid conditions, only the deposition at around 300 °C was observed in [2], indicating that the mechanism leading to this deposition involves moisture. In the present work the depositions obtained in the earlier experiments [2]

were characterized using SEM/EDX analysis. The results confirm the formation of PbTe crystals around 600 °C and reveal that crystalline elemental tellurium is deposited at 300 °C (see Fig. 1). The fact that the temperature of the second deposition cannot be predicted using eq. 1 with the thermodynamic data of elemental tellurium indicates that the chemical process underlying the deposition at 300 °C is not a simple Te(s)/Te(g) or Te(s)/Te<sub>2</sub>(g) sublimation/desublimation equilibrium, but rather a more complex process that might involve impurities in the carrier gas. The observation that moisture promotes the formation of the low temperature deposition indicates that H<sub>2</sub>O-impurities may play a role in the low temperature deposition mechanism.

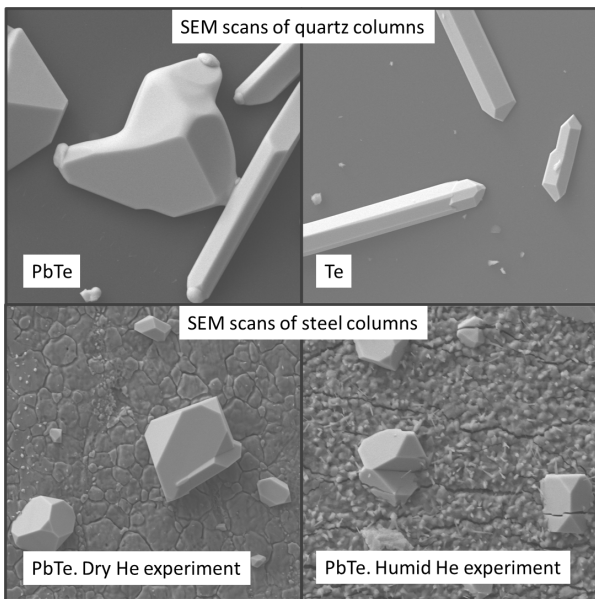


**Figure 1.** SEM images of depositions found in quartz and steel columns.

Fig 2a compares a deposition pattern recorded in a 1 h thermosublimatography experiment in a fused silica column in He containing ca. 50 to 100 ppm of H<sub>2</sub>O (1<sup>st</sup> heating) with the pattern obtained after a second, prolonged heating of 3 h of the material deposited in the 1<sup>st</sup> heating in He. It is obvious that the PbTe peak almost disappeared during the second heating, while the low-temperature deposition increased. In a similar set of two consecutive experiments with H<sub>2</sub>O content <1 ppm the transport to the lower deposition temperature is much less pronounced (Fig. 2b). This indicates that moisture indeed plays a crucial role in the transport mechanism. Adding oxygen or hydrogen to the carrier gas does not cause such effects. In similar experiments under oxidative conditions almost no tellurium activity was transported to the column. This is likely due to the formation of an oxide layer on the LBE surface which inhibits the evaporation of the melt components. With a 10% addition of hydrogen to the He carrier gas we observed a tellurium distribution similar to that under inert conditions (see Fig. 2c).

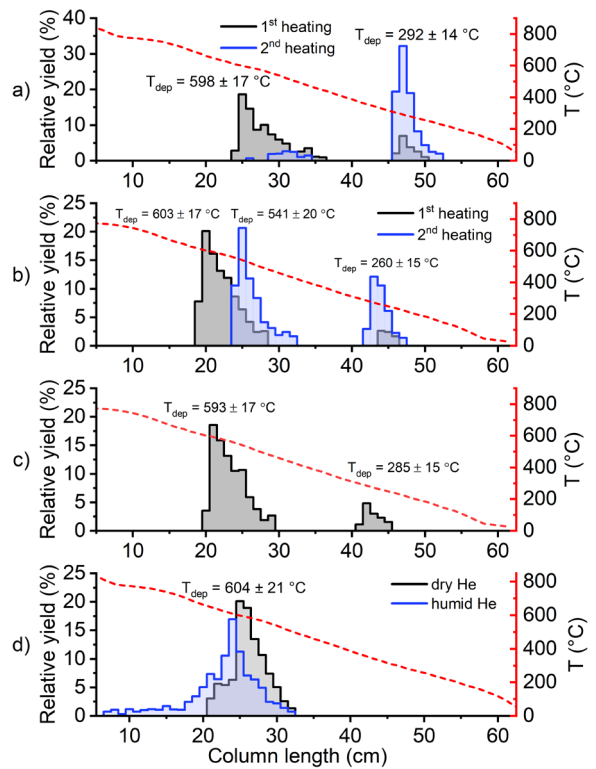


**Figure 2.** Thermosublimatograms of LBE-Te samples, where dashed line represents temperature gradient, and solid line shows distribution of Te. a) consecutive heatings in He with higher water impurity; b) consecutive heatings in He with lower water impurity; c) experiment with 10% admixture of H<sub>2</sub> to He; d) experiments in steel columns in dry and moist He atmospheres.

Experiments in steel columns in both humid and dry conditions (Fig. 2d) show only lead telluride formation, which was also confirmed using SEM studies (Fig.1). From this, we can conclude that lead telluride is stable on the steel surface and does not react with steel components under the studied conditions. More importantly, the present results indicate that the process leading to the low temperature deposition in fused silica columns obviously does not occur in steel columns. This finding is not only important for designing future transpiration experiments aimed at determining tellurium vapor pressure over LBE, but also more generally for the safety assessment of LBE-cooled reactors.

### Acknowledgements

This work was funded by the PASCAL project under EURATOM HORIZON2020 Grant Agreement No. 945341.

### References

- [1] L. Zanini et al., PSI Report 08-04, Paul Scherrer Institut, Villigen PSI, Switzerland, ISSN 1019-0643 (2008)
- [2] V. Zobnin et al., *LRC Annual report 2022*, 50 (2023)
- [3] R. Eichler et al., *Radiochim. Acta*, **87**, 151 (1999)

# Thallium release from LBE doped with iodine determined from transpiration data

J. Neuhausen (PSI), I. I. Danilov (UniBe & PSI)

## Introduction

Thallium radionuclides belong to the most prominent radionuclides produced in the LBE coolant of the MYRRHA reactor. According to [1] thallium ranks No. 9 in the hierarchy of unmitigated relative dose impact of all elements with radioactive nuclides produced in the LBE of the MYRRHA ADS. Therefore, it is important to investigate its release from liquid LBE. In an early paper [2] the release of non-carrier-added  $^{202}\text{Tl}$  generated by neutron activation in LBE has been studied in a temperature range between ca. 400 and 1273 K in an Ar/7%H<sub>2</sub> atmosphere. In this work, no measurable Tl evaporation was detected. In a later study [3] a temperature-dependent thermodynamic activity coefficient for Tl in LBE was estimated from literature data on the Pb-Tl and Bi-Tl systems that qualitatively supports the experimental finding that the vapour pressure of elemental Tl above diluted solutions in LBE is low. However, a recent thermodynamic assessment of the MYRRHA system [4] predicted that in presence of iodine impurities, thallium may be released in form of thallium iodide TlI, enhancing the release of thallium. Transpiration experiments on LBE samples containing both thallium and iodine were performed in the MYRTE project between 2015 and 2019 [5]. However, since the focus of MYRTE was iodine release, the experiments were never carefully evaluated in terms of the behaviour of thallium. To verify the thermodynamic predictions the MYRTE data are now evaluated to obtain more information regarding the evaporation of Tl from LBE.

## Experimental

For a detailed description of the sample preparation and the procedure for transpiration type experiments we refer to reference [5]. The various series of experiments performed within MYRTE can be divided in two groups concerning the iodine concentrations present in the LBE: Experiments of group 1 were performed using LBE-samples doped with weighable amounts of neutron-irradiated PbI<sub>2</sub>. Thus, they contained relatively large amounts of iodine, i.e. mole fractions of  $6 \times 10^{-4}$  and  $5 \times 10^{-5}$ . For these samples it can be definitely stated that there is a large excess of iodine with respect to thallium, i.e. the ratio I:Tl is  $\gg 1$ .

On the other hand, experiments of group 2 were performed using LBE doped with tellurium in which  $^{131}\text{I}$

was produced by neutron irradiation. The concentrations of  $^{131}\text{I}$  calculated from its activity correspond to mole fractions around  $10^{-10}$  to  $10^{-11}$ . However, it is not clear whether additional stable iodine isotopes are present in these samples. In NAA analyses performed at SCK-CEN on the LBE, no iodine was detected at a detection limit of ca. 0.05 atom-ppm, i.e. mole fractions of  $5 \times 10^{-8}$ . Therefore, it cannot be ruled out that additional stable iodine is present in these LBE samples up to this detection limit.

Similarly, it is straight forward to calculate the mole fraction of  $^{202}\text{Tl}$  in the investigated samples from the measured activities. For experiments of group 1 these concentrations ranged from  $x_{\text{Tl}} \cong 4 \times 10^{-13}$  to  $4 \times 10^{-14}$ , while for group 2  $x_{\text{Tl}}$  was about  $10^{-12}$ . However, it is not clear how much additional Tl is present in these samples in form of stable Tl isotopes. ICP-MS analyses of the raw materials indicate Tl-concentrations below the detection limit, i.e. in the order of a few ppm. Therefore, the presence of stable Tl in these samples up to mole fractions of some  $10^{-6}$  cannot be ruled out.

## Results and discussion

Typical results for experiments with a large excess of iodine compared to the Tl-content are shown in Fig. 3. For comparison, the estimated temperature function of the Henry constant of Tl in LBE estimated in [3] and the vapour pressure of pure TlI [5] are plotted as well.

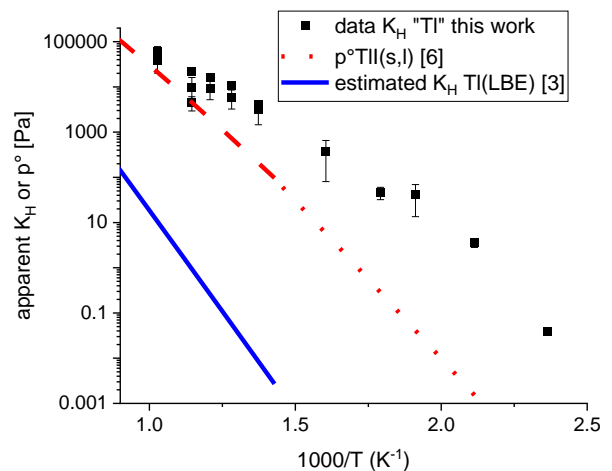


**Figure 3:** apparent Henry constant of Tl in non-reduced LBE prepared from Pb and Bi with 99.9999% purity, containing iodine as impurity with a mole fraction of ca.  $6 \times 10^{-4}$ , measured in purified helium gas at a flow of 100 ml/min.

The measured data are many orders of magnitude higher than those expected for elemental Tl dissolved in LBE. The Henry constants also are higher than the vapor pressure of pure Tl. A plausible interpretation is that thallium in these samples indeed evaporates in form of  $Tl(g)$ , and that the activity coefficient of Tl dissolved in LBE is  $>1$ . Activity coefficients larger than 1 are expected for the solution of a polar species such as Tl in a non-polar metallic solvent. Thus, the present results are chemically plausible and confirm the predictions of the thermodynamic model of [4].

Fig. 4 shows a comparison of the results for two series of experiments with non-carrier added amounts of iodine impurity. The two series differ regarding the pretreatment of the LBE prior to the experiments.

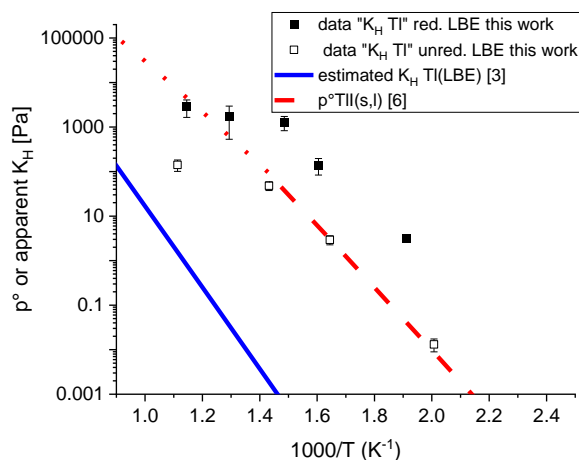


**Figure 4:** apparent Henry constant of Tl in unreduced (open squares) and reduced LBE (filled squares) containing non-carrier-added amounts of iodine, measured in purified helium gas at a flow of 100 ml/min.

For one series the LBE has been reduced by contact with hot tantalum foil prior to the doping with tellurium and subsequent neutron activation for generation of  $^{131}I$ . The Henry constant data from this series (filled squares in Fig. 4) are very similar to those obtained with much higher concentrations of the iodine impurities shown above. Thus, they are well compatible with the interpretation proposed above that Tl is formed in the liquid metal and subsequently evaporated. Looking at the relative concentrations of  $^{131}I$  and  $^{202}Tl$  calculated from their activities, it seems plausible that the thallium is completely converted to Tl because of the excess of iodine. However, it is surprising that this reaction occurs quickly and completely at mole fractions of  $x_I \cong 10^{-10}$  and  $x_{Tl} \cong 10^{-12}$ . This may indicate that the actual concentrations of iodine and/or thallium may be higher than those indicated by the activities of the studied isotopes, caused by additional stable iodine and thallium present in the sample. The open squares in Fig. 4 show results obtained from experiments using LBE that was not reduced. It is obvious that also for this series of experiments the data obtained for the apparent Henry constant of Tl in LBE is much higher than expected for elemental Tl dissolved in LBE. At the lower temperatures the data agree well with the

behavior expected for an ideal solution of Tl in LBE, i.e. a solution with activity coefficient 1. Thus, the apparent Henry constant found in this series is clearly lower compared to that found in the experiments with reduced LBE. The reason for this difference is not clear so far. A comparison of results from the experiments evaluated so far indicates that the reason for the varying behavior is not the reductive pre-treatment but rather a different impurity spectrum in the different batches of LBE used. Evaluation of the remaining series of experiments will help to clarify whether this interpretation is valid and systematic variations between different LBE batches can be found.

## Conclusion and outlook

The results obtained here indicate that Tl dissolved in LBE is transformed into species that evaporate much faster than expected for elemental Tl dissolved in LBE when iodine is present in the LBE. Most likely, Tl is formed in the liquid metal and evaporated as  $Tl(g)$ , in agreement with thermodynamic predictions [4]. It seems that the behavior of Tl in LBE may be influenced by the presence of other impurities present in different batches of LBE. More information on this effect may be obtained from a careful evaluation of available but not yet evaluated data. There will however remain open questions concerning the evaporation behavior of thallium from LBE that cannot be answered using the available data. This includes studying the kinetics of Tl formation from I and Tl dissolved in LBE as a function of their concentrations and temperature as well as a dedicated study of the temperature dependency of the thermodynamic activity coefficient of pure Tl in LBE. Given the recent advances in using the transpiration method for studying the evaporation of small amounts of radiotracers from LBE, such studies may be envisaged for follow-up projects.

## Acknowledgements

This work was funded by the project PATRICIA under EURATOM HORIZON2020 Grant Agreement No. 945077.

## References

- [1] A. Aerts et al., Behavior of Spallation, Activation and Fission Products in LBE, in *Comprehensive Nuclear Materials* 2<sup>nd</sup> ed., 735 (2020)
- [2] J. Neuhausen et al., *Radiochim. Acta*, **93**, 155 (2005)
- [3] C. Fazio (ed.), *Handbook on Lead-bismuth Eutectic Alloy and Lead Properties, Materials Compatibility, Thermal-hydraulics and Technologies - 2015 Edition*, OECD-NEA Report 7268, Paris, France (2015)
- [4] A. Aerts et al., Deliverable D5 for the LB2 (LBE Chemistry) Focus Point, Report SCK•CEN/23927153(R-6452), Mol, Belgium (2017)
- [5] J. Neuhausen et al., Report on volatilization and deposition studies, MYRTE deliverable D4.3, Paul Scherrer Institut, Villigen PSI, Switzerland (2019)
- [6] M. Binnewies, E. Milke, *Thermochemical Data of Elements and Compounds* 2nd Edition, Wiley VCH (2002)

## Optimization of a matrix isolation setup for the study of volatile and reactive gaseous Te molecules

I. Zivadinovic (ETHZ & PSI), J.-E. Colle (JRC Karlsruhe), A. Kovacs (JRC Karlsruhe), O. Beneš (JRC Karlsruhe), J. Neuhausen (PSI), P. Steinegger (ETHZ & PSI)

### Introduction

The focus of this research was centered on the development and optimization of a matrix isolation apparatus to study volatile and reactive chemical species, with a particular focus on Te molecules such as tellurium dioxide or Telluric acid. This endeavor is motivated by the need to understand the evaporation dynamics of different Po molecules from liquid lead-bismuth eutectic (LBE). The latter is foreseen as coolant as well as spallation target in a so-called accelerator driven system (ADS) and represents a Gen IV nuclear reactor concept. The thus obtained results are critical for the later envisaged safety evaluation and licensing of such advanced systems. Te, as a lighter homolog of Po, serves as a surrogate for its heavier counterpart, offering at the same time insights into the release behavior of Te itself, which is likewise produced in the LBE of an ADS during operation.

### Experimental Setup

To achieve the research objective, a specialized matrix isolation apparatus was used. This comprised a cylindrical Knudsen cell made from W and filled with the desired material to be effused and deposited (Fig. 1). The cell was placed in an evacuated chamber and resistively heated to evaporate the material, which subsequently effuses through small holes (0.5 mm) on either side. The effused material from both holes was directed towards a quartz crystal microbalance (QMB) for mass quantification on one side and an Ir-coated and cooled mirror for solid Ar matrix formation on the other side. The solid Ar is formed by dosing Ar into the evacuated matrix chamber and condensing it on the mirror, that is cooled to 5K. Since the Ar matrix formation and the effusion of the substrate occur simultaneously, the reactive molecules are trapped within the growing Ar crystal in the form of defects. This isolates individual molecules from each other and prevents undesired reactions of the deposited reactive species among themselves and with contaminants due to the inert nature of the Ar matrix. After the crystal is sufficiently grown, the matrix containing the sample is irradiated with a 532 nm laser for Raman scattering measurements. The scattered radiation is passed through a spectrometer to a detector, for the vibrational characterization of the trapped species.

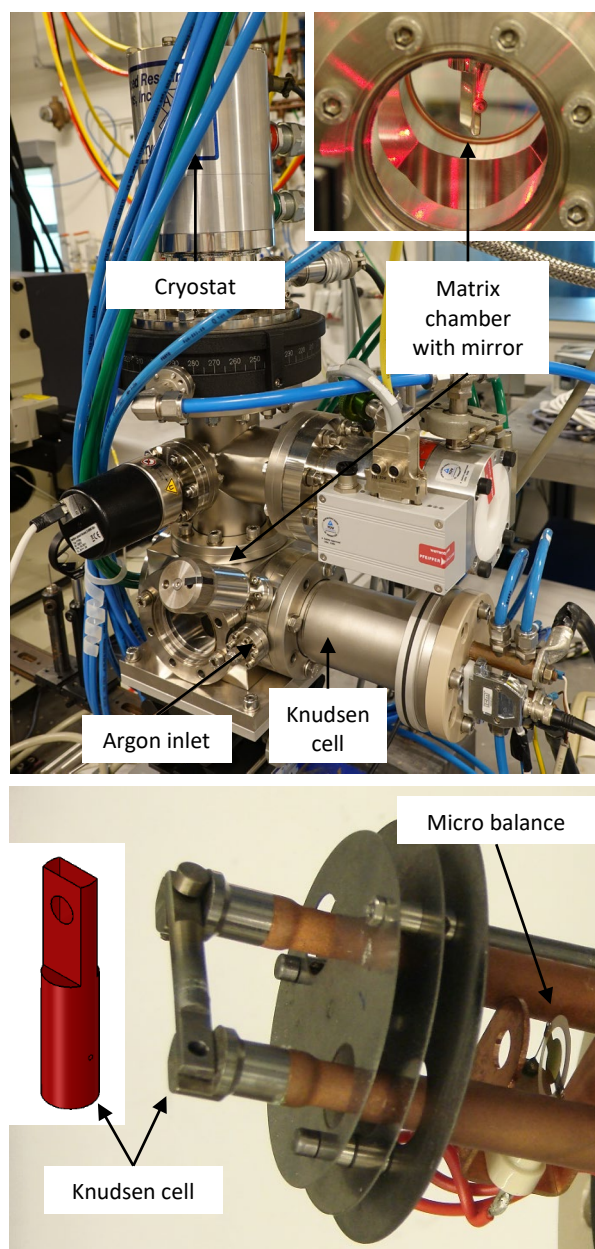


**Figure 1:** Top picture: Image of the matrix isolation setup, which consists of the main chamber, a side chamber containing the Knudsen cell, as well as a He-cooled cryostat. (Insert: Main chamber with the Ir-coated mirror) Bottom picture: Knudsen cell fixed between the heating elements. The quartz crystal microbalance is located behind the heat shield. (insert: schematic of the Knudsen cell with one hole visible)

## Method validation and optimization with Sulfur

Before attempting the speciation analysis of Te in the gas phase, S was employed as a reference material to validate and fine-tune the experimental setup. The start of the effusion process, which is tracked by the frequency change of the QMB as a result of a deposition onto the crystal, represents the most important step of setting up the experiment. Achieving an optimum deposition rate is critical for several reasons. If insufficient material is deposited within the Ar matrix, the sample fails to produce a detectable spectral response. Contrary, depositing excessive amounts of material can lead to undesirable outcomes, such as side reactions or the formation of agglomerates within the Ar matrix. Such occurrences can obscure or distort the spectral signals of interest, complicating the interpretation of results. In addition, the deposition rate of the investigated material needs to be adjusted to the growth rate of the Ar matrix to ensure a uniform distribution of the desired substance within the Ar crystal. Sulfur with its high vapor pressure already at moderate temperatures made it easy to tune the deposition rate. This allowed us to achieve a robust spectral response during the deposition process, which proved to be essential for determining optimum deposition parameters. During these initial runs, we successfully deposited isolated S molecules within the Ar matrix. The resulting spectrum obtained from the trapped molecules is depicted in Figure 2.

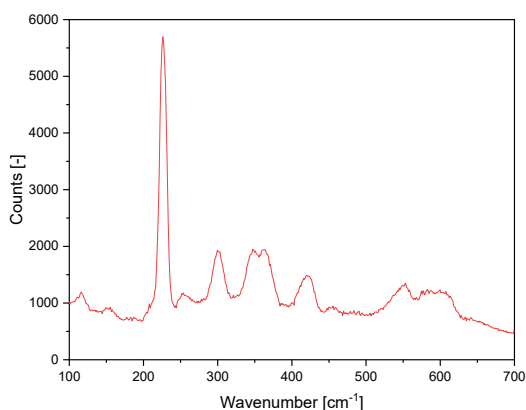


**Figure 2:** Raman spectrum of deposited S within the solid Ar matrix using an excitation wavelength of 532 nm.

The obtained Raman spectrum seems to indicate that sulfur was incorporated into the Ar matrix predominantly as S<sub>8</sub> rings with small proportions of various other sulfur allotropes, including but not limited to S<sub>7</sub> rings [1-2]. This matched our expectations, as those allotropes represent the predominant forms in both natural elemental sulfur crystals, as well as within the melt [3]. Further analysis and calculations are needed to confirm the exact composition and ratios of the various allotropes.

Following the successful commissioning of the setup, we will attempt to isolate and analyze the gaseous species of tellurium dioxide in the next step. First calculations imply that this substance most likely evaporates either as a monomer or as a dimer (see Fig. 3).

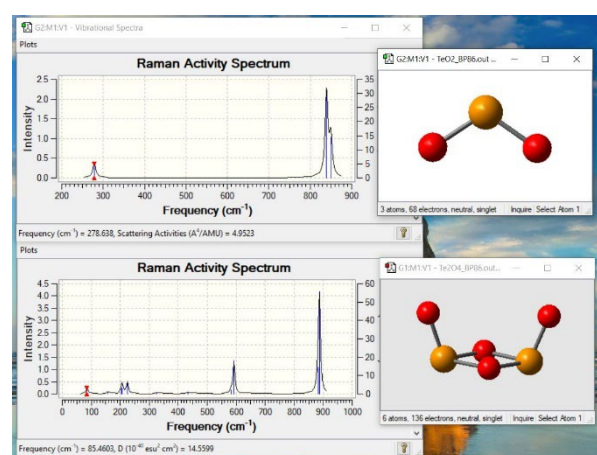


**Figure 3:** Calculated Raman spectrum of TeO<sub>2</sub>. The formation of both the monomer and the dimer seem plausible.

## Acknowledgements

This work was funded by the PATRICIA project under EURATOM HORIZON2020 Grant Agreement No. 945077.

This work was supported by an ETH Zurich Doc.Mobility Fellowship

## References

- [1] R. Streudel et al., *Z. Naturforsch.*, **43**, 581-589 (1988)
- [2] E. Picquenard et al., *J. Mol. Struct.*, **293**, 63-66 (1993)
- [3] G. A. Ozin, *J. Chem. Soc. D*, **22**, 1325-1327 (1969)

# Electrodeposition of thin films of metallic Ho from ionic liquids

N. Cerboni (ETHZ & PSI), M. Christl (ETHZ), A. Müller (ETHZ), C. Vockenhuber (ETHZ), P. Steinegger (ETHZ & PSI), E. A. Mauger (PSI)

## Introduction

Auger electrons (AEs) have an anti-cancer effect not only when delivered directly into the nucleus of the cancer cell, but also when placed close to the cellular membrane [1]. Consequently, a novel class of radiopharmaceuticals could be designed, particularly using radiolanthanides such as  $^{155}\text{Tb}$ ,  $^{161}\text{Tb}$ , and  $^{161}\text{Ho}$  [2]. To enable precise micro dosimetry using said radionuclides, an accurate experimental characterization of the energy distribution and emission probabilities of AEs is needed. Unfortunately, the demanding nature of such measurements translates into a lack of suitable data [3]. One of the main challenges is the production of a proper source for these measurements. An ideal method of source preparation of AE-emitting radionuclides should provide thin films of chemically pure, electrically conductive and uniformly distributed radionuclides, to avoid AE self-absorption. The latter leads to a reduced energy resolution and, consequently, to a more difficult spectrum interpretation. The electrodeposition of thin films of metallic lanthanides (Lns) is a promising technique for this purpose. Nevertheless,  $\text{H}_2\text{O}$  cannot be used as an electrolyte due to the negative standard reduction potential of Lns (i.e., between  $-2 V_{\text{vs. SHE}}$  and  $-2.5 V_{\text{vs. SHE}}$  [4]), which is lower than reduction potential of  $\text{H}_2\text{O}$  itself. Ionic liquids (ILs) are an alternative to aqueous electrolytes because they feature large electrochemical stability windows – among other favorable properties [5]. This allows for the application of the required low potentials, thus, enabling a complete reduction of Lns. So far, the challenging task of electrodepositing metallic Lns has only been studied for a limited number of these elements [6].

This work focuses on the electrochemical deposition of thin films of metallic Ho from ILs and their subsequent structural characterization.

## Experimental

Studies on the electrodeposition of Ho in 1-butyl-1-methylpyrrolidinium bis(trifluoromethylsulfonyl)imide ([BMP][TFSI]) were carried out in a glovebox under an inert Ar atmosphere ( $\text{H}_2\text{O}$  and  $\text{O}_2 \leq 0.1$  ppm).

In order to increase the solubility of Ho in [BMP][TFSI],  $\text{Ho}(\text{TFSI})_3$  was synthesized by a ligand exchange reaction between  $\text{Ho}_2\text{O}_3$  and HTFSI (stoichiometric ratio of 1:6) in  $\text{H}_2\text{O}$ , while stirring and heating at  $80^\circ\text{C}$

for 40 min. Any excess of HTFSI and  $\text{H}_2\text{O}$ , that could potentially affect the electrochemical properties of the solution, were removed under vacuum at  $120^\circ\text{C}$  for 24 h. A 90 mM solution of  $\text{Ho}(\text{TFSI})_3$  in [BMP][TFSI] was prepared under an inert Ar atmosphere. A Au working electrode (WE; 1 mm diameter), a Pt wire as counter electrode (CE) and a self-made reference electrode (RE; double-junction glass body with a Ag wire in [BMP][TFSI] separated by a Vycor tip from the analyzed solution) were used in the cyclic voltammetry (CV) experiments. The  $\text{Fc}/\text{Fc}^+$  couple was used as an internal standard.

Subsequently, a Ho electrodeposition was performed at  $-2.14 V_{\text{vs. Fc}}$  for 48 hours. The employed setup (detailed in Ref. [7]) consisted of the previously mentioned RE, an Au foil (used as WE; 10 mm diameter) and a Pt foil (used as CE; 10 mm diameter). Following electrodeposition, dry dimethylformamide and dry isopropanol were used to wash the Au foil.

The surface morphology and the elemental composition of the resulting deposit were analysed by scanning electron microscopy (SEM) and energy-dispersive X-ray spectroscopy (EDX), respectively. Meanwhile, the depth profile of the deposited elements was investigated by 2 MeV  $\text{He}^{2+}$  Rutherford backscattering (RBS) and 13 MeV  $^{127}\text{I}$  heavy ion time-of-flight elastic recoil detection analysis (ERDA), at the Laboratory of Ion Beam Physics, ETH Zürich.

## Results and discussion

To better understand the electrochemistry of Ho, CV analyses were performed for [BMP][TFSI] both without and with Ho (see Fig. 1). In the case of pure [BMP][TFSI], no significant reduction peaks are visible throughout the whole investigated potential range. The drop toward  $-3 V_{\text{vs. Fc}}$  arises because of the decomposition of [BMP][TFSI]. Compared to the pure [BMP][TFSI], Ho-[BMP][TFSI] displays a major current peak at  $-2.7 V_{\text{vs. Fc}}$ , which is attributed to the reduction of  $\text{Ho}(\text{III})$ .

Using the data obtained from the CV, Ho was electrodeposited by applying different voltages for different periods of times. The most homogeneous surface was achieved by applying a constant voltage of  $-2.14 V_{\text{vs. Fc}}$  for 48 hours. Based on this initial result, an attempt to deposit onto a larger surface was carried out with the deposition cell described in Reference [7].

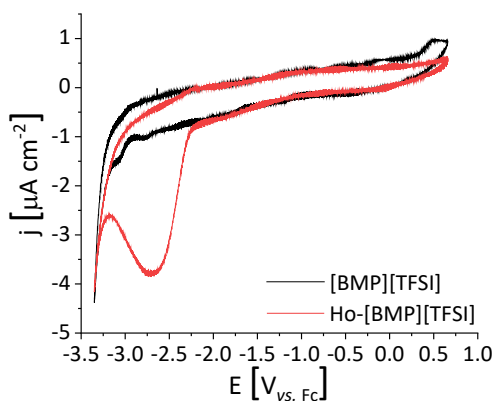


**Figure 1:** Second cycle of the CV responses recorded at  $100 \text{ mV s}^{-1}$  for pure [BMP][TFSI] (black) and Ho-[BMP][TFSI] (red).

The deposited film exhibited a spectrum of different tarnishing colors, indicative of a nanometer-scale thickness. A large feature, possibly generated by the  $\text{H}_2$  evolution caused by the reduction of residual  $\text{H}_2\text{O}$ , is visible on the upper part of the WE (see insert in Fig. 2(a)). The SEM image of the resulting deposit (see Fig. 2(a)) shows a very uniform film with no cracks, resembling the surface morphology of the WE prior to the deposition (not shown here). The EDX spectrum (see Fig. 2(b)) proves the presence of Ho, thus, indicating its successful deposition. However, the deposit also contains elements C, N, O, F, and S, which originate from [BMP][TFSI], and the handling in air. In addition, by comparing the weak Ho signal to the very intense Au signal from the underlying Au foil, one can conclude on a film thickness below the micrometer range.

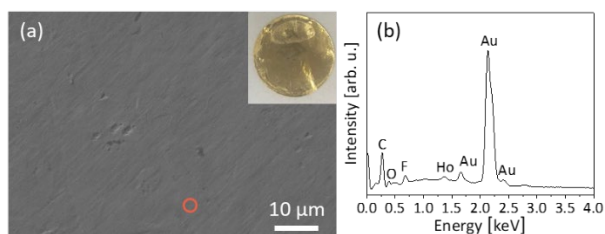


**Figure 2:** (a) the SEM image of the Au foil used as WE (insert) after applying  $-2.14 \text{ V}_{\text{vs. Fc}}$  for 48 hours to Ho-[BMP][TFSI] and (b) the EDX spectrum of a selected area (red circle in (a)).

The depth profile of the elemental composition of the deposited Ho film was investigated by RBS (see Fig. 3(a)). The sharp peak at approx. 1.8 MeV and the respective tailing indicate that Ho is present throughout the whole investigated thickness. The experimental outcome agrees reasonably well with dedicated SIMNRA simulation of Ho on Au. Since the cross sections of the backscattering of  $\text{He}^{2+}$  ions with Ho and Au are quite similar, no reasonable assessment of the film thickness could be made. The light trace elements H, C, N, O, F, and S were measured by means of ERDA (see Fig. 3(b)). It is worth mentioning that the presented depth profile is to be considered only qualitatively. Since the sample was exposed to air for a long period of time prior to the RBS/ERDA measurements, a high concentration of oxygen was

expected at the surface, caused by the oxidation of reactive metallic Ho. However, mostly H, C, and F were found at the surface (see Fig. 3(b)). This could indicate that, upon electrodeposition, Ho is reduced to its metallic state and subsequently reacts with [BMP][TFSI] to form a layer of Ho compounds. The concentration of lighter elements decreases with increasing distance from the surface of the deposited film, until they completely disappear. This phenomenon suggests that a thin film was deposited, and the Ho compounds on the surface hinder the further oxidation of the underlying Ho in air.

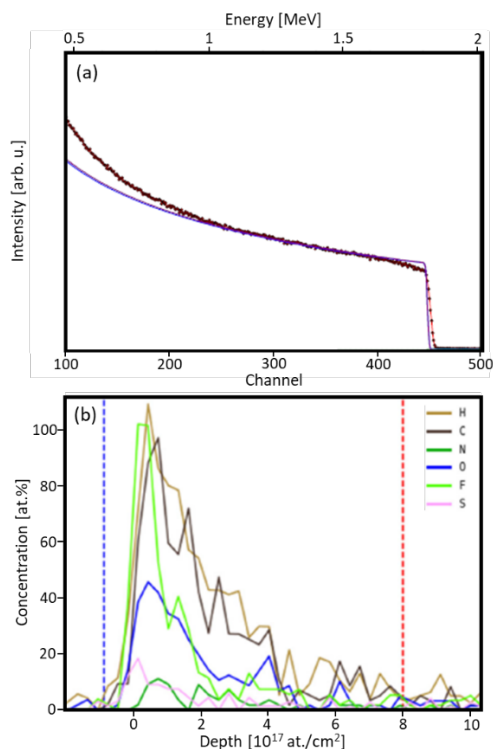


**Figure 3:** (a) RBS spectrum with the experimental data (black dots and red line) and SIMNRA simulations (blue line) and (b) ERDA spectra (i.e., only measured for the range between the blue and red dashed lines) of the Ho film on the Au foil after applying  $-2.14 \text{ V}_{\text{vs. Fc}}$  for 48 hours to Ho-[BMP][TFSI].

These findings need further investigation by X-ray photoelectron spectroscopy (XPS) analysis. A combination of XPS and  $\text{Ar}^+$  sputtering may provide an indication for the change in oxidation state of Ho at the surface in comparison to Ho in the bulk of the film. In addition, to minimize the number of elements, present as impurities and co-deposited at the surface, other ILs may be investigated.

## References

- [1] A. Ku et al., *EJNMMI Radiopharm. Chem.*, **4**, 1 (2019)
- [2] D. Filosofov et al., *Nucl. Med. Biol.*, **94**, 19 (2021)
- [3] T. Vyllov et al., *Catalogue of radionuclide LEES* (2003)
- [4] P. Vanysek, *CRC Handb. Chem. Phys.*, **8** (2000)
- [5] M. Freemantle, *An introduction to ILs*, RSC (2010)
- [6] A. P. Abbott et al., *Annu. Rev. Mater. Res.*, **43**, 24 (2013)
- [7] E. A. Maugeri et al. *LRC Annual Report 2017*, 37 (2018)

# Influence of selected critical parameters on molecular plating

X. Kou (ETHZ & PSI), N. Cerboni (ETHZ & PSI), D. Ferri (PSI), P. Steinegger (ETHZ & PSI), E. A. Maugeri (PSI)

## Introduction

Molecular plating (MP) is a form of electrodeposition occurring in organic solvents providing wide electrochemical stability windows [1]. This method has been established as a standard procedure for the preparation of targets for nuclear physics experiments consisting of a specific radionuclide. Despite over six decades of research, the exact mechanism of the plating process and the precise composition of the resulting thin films remain poorly understood. Existing experimental evidence suggests a mechanism that includes the electrolytic dissociation of organic solvents and trace amounts of water in the system, leading to the formation of metal carboxylates and hydroxides during MP [2-5]. Recent studies have explored the influences of several critical parameters on the outcome of MP, including the roughness of the substrate surface, solvent type, salt concentration, and the current density [6]. However, the effects of other variables, such as the water content and the salt type, have yet to be thoroughly investigated. Here, the influence of (1) the water content in the DMF-based plating solution as well as (2) the counter ion of Gd(III) on MP is reported.

## Experimental

The conducted MP experiments utilized a simple two-electrodes setup, using a carbon foil as the substrate/cathode and a coiled Pd wire as the anode (setup shown in [7]). MP experiments were conducted using galvanostatic approach at a current density of  $0.8 \text{ mA cm}^{-2}$ . In this study the plating solution consisted of the following constituents (1) 12 mL of DMF, (2) ca. 0.6 mg of  $\text{Gd}(\text{NO}_3)_3 \cdot 6 \text{ H}_2\text{O}$ , and (3) 10  $\mu\text{L}$  of 0.01 M  $\text{HNO}_3$ . For comparative analysis, when  $\text{GdCl}_3$  was evaluated against the nitrate, the  $\text{Gd}(\text{NO}_3)_3 \cdot 6 \text{ H}_2\text{O}$  and  $\text{HNO}_3$  were replaced by  $\text{GdCl}_3 \cdot 6 \text{ H}_2\text{O}$  and  $\text{HCl}$ . A series of experiments were conducted to investigate the impact of water content on the MP process. For the anhydrous conditions, the MP was carried out in a glovebox using anhydrous DMF (99.8%, Sigma-Aldrich) as the solvent. In contrast, experiments performed under ambient conditions utilized standard DMF (99.8%, Sigma-Aldrich).

The topographical characteristics of the deposited layer were examined using Scanning Electron Microscopy (SEM; Zeiss NVision 40). Considering the insulating properties of the deposited materials, an operational

voltage of 3-5 kV was determined to be optimal. For a comprehensive elemental characterization of the deposited film, Energy Dispersive X-ray spectroscopy (EDS; X-Max SDD Detector, Oxford Instruments Inc.) was used. The IR spectrum was collected in attenuated total reflection mode (ATR) using a spectrometer (Tensor 27, Bruker) equipped with a Pt-ATR unit and a liquid  $\text{N}_2$  cooled HgCdTe detector.

## Results and discussion

The comparison of the SEM images of the plated layers produced under anhydrous and ambient conditions highlight the influence of water on the MP process (Fig. 1). The presence of water contributes to the formation of a more uniform surface. Meanwhile, the sample prepared under anhydrous condition displays a significant number of island-like features, indicative of potential side reactions occurring during the deposition process.

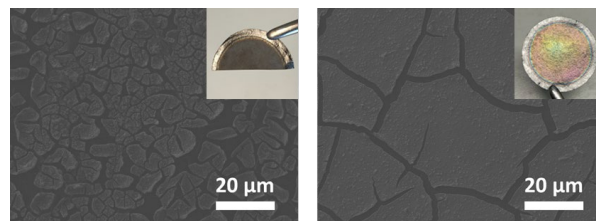


**Figure 1:** SEM images (magnification given at the bottom right) of the plated layer under anhydrous (left) and ambient condition (right); embedded are the digital images.

The result from EDX analysis (Fig. 2, right) shows traces of Pd dendrites detected at the surface of the carbon backing foil between the island of deposited material, indicating the corrosion of Pd anode.

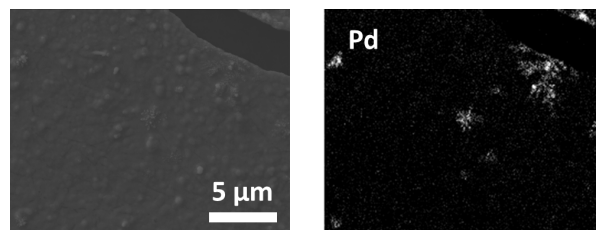


**Figure 2:** SEM image of the plated layer under ambient condition (left) and EDX mapping of Pd (right).

The IR spectrum of the film obtained in ambient condition is depicted in Fig. 3. Distinct absorption bands are observed at  $1570 \text{ cm}^{-1}$  and  $1357 \text{ cm}^{-1}$ , indicating the presence of carboxylate compounds, possibly formates [8]. Additionally, a broad absorption band around  $3300$

$\text{cm}^{-1}$  potentially indicates the presence of OH species. Considering the molecular structure of DMF and the distinctive ammonia-like odor of the post-deposition electrolyte, it is postulated that DMF undergoes decomposition during the molecular plating process, yielding products such as dimethylamine and formic acid. Subsequent reactions between the formate anion and  $\text{Gd}^{3+}$  could result in the precipitation of  $\text{Gd}(\text{OOCH})_3$ . However, due to the overlapping and dispersive feature of the OH band, definitive identification of the exact chemical species remains ambiguous, leaving Gd hydroxide as a potential additional product.

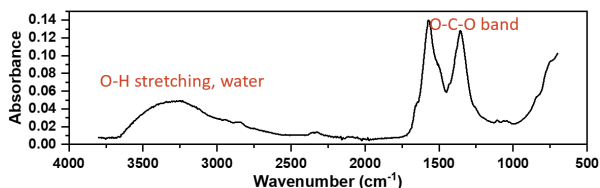


**Figure 3:** FT-IR spectrum of the deposited layer from DMF under ambient condition, indicating the presence of  $\text{Gd}(\text{OOCH})_3$  and probably  $\text{Gd}(\text{OH})_3$

While both metal nitrates and chlorides have been utilized for MP in the past, the impact of the anionic counter ion on the plating outcome needs to be studied. In case of  $\text{GdCl}_3$  as the precursor salt, a large amount of Pd clusters were formed (Fig. 4). This can be attributed to the formation of tetrachloropalladate complexes; similar complexes do not form in case of Gd nitrate-based plating solutions. Evidently, the latter offers superior performance in MP compared to chloride-based plating solutions.

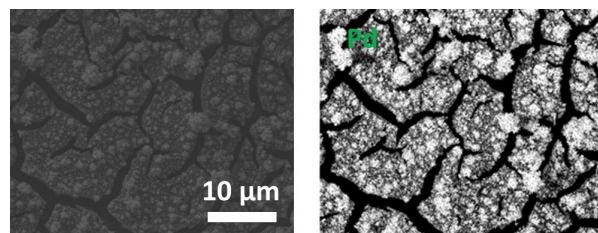


**Figure 4:** SEM image of the plated layer from chloride (left) and Pd signal from EDX (right).

## Outlook

From the aforementioned study, future work will focus on several topics: the temporal evolution of the yield; the optimal water content for MP; validation of the proposed decomposition of DMF into carboxylates. The relevant findings can significantly enhance our understanding of the MP technique.

## References

- [1] J. Runke et al., *J. Radioanal. Nucl. Chem.*, **299**, 1081 (2014)
- [2] A. Vascon et al., *Nucl. Instrum. Methods Phys. Res. B*, **696**, 180 (2012)
- [3] A. Vascon et al., *Nucl. Instrum. Methods Phys. Res. B*, **721**, 35 (2013)
- [4] A. Vascon et al., *J. Radioanal. Nucl. Chem.*, **299**, 1085 (2014)
- [5] K. Myhre et al., *Surf. Sci. Spectra*, **25** (2018)
- [6] A. Vascon et al., *Nucl. Instrum. Methods Phys. Res. B*, **714**, 163 (2013)
- [7] K. Eberhardt et al., *Nucl. Instrum. Methods Phys. Res. A*, **521**, 208 (2004)
- [8] P. Lustemberg et al., *J. Phys. Chem. C*, **119**, 21452 (2015)

## Electrodeposition of Tb films from ionic liquids

F. Weigand (ETHZ), N. Cerboni (ETHZ & PSI), P. Steinegger (ETHZ & PSI), E. A. Maugeri (PSI)

### Introduction

In recent years, the radiolanthanide  $^{161}\text{Tb}$  has emerged as promising candidate for radiotherapy applications, due to its chemical similarities to clinically approved  $^{177}\text{Lu}$  and its associated superior decay characteristics [1]. Unlike  $^{177}\text{Lu}$ ,  $^{161}\text{Tb}$  emits a significant number of Auger and conversion electrons during disintegration [2], which have been found to enhance its therapeutic efficacy [3]. In the context of a medical application, the measurement of associated Auger electron spectra is key to enable precise microdosimetry. This in turn requires the manufacturing of atomically thin and homogeneous Tb films to serve as sources for accurately measuring the energies and emission probabilities of said electrons [4].

Electrodeposition (ED) presents an effective method to produce such films. In this process, a specific voltage is applied across electrodes immersed in a Tb(III)-containing solution leading to the reduction and deposition of Tb(0) on the working electrode (WE). The ED of Tb cannot be performed in aqueous solutions due to the highly negative reduction potential of Tb ( $-2.3\text{ V}$  at standard conditions [5]) which is outside of the electrochemical stability window of  $\text{H}_2\text{O}$ . At these negative voltages,  $\text{H}_2\text{O}$  reduces to  $\text{H}_2$  gas at the surface of the WE, thus preventing the Tb deposition. Furthermore, the presence of  $\text{H}_2\text{O}$  leads to the formation of undesired Tb hydroxides and oxides. A promising alternative as an electrolyte for the ED of metallic Tb are ionic liquids (ILs). These are known for their broad stability range down to very negative potentials and their ability to readily dissolve Tb.

Presented here and inspired by previous work done on the ED of metallic Tb from ILs [6] are the influence of the WE material, the deposition time, the temperature as well as the anion of the IL on the surface morphology of the electrodeposited Tb film.

### Experimental

All experiments were conducted using 10 mM Tb solutions, produced by dissolving  $\text{Tb}(\text{NO}_3)_3$  (REActon,  $\geq 99.99\%$ ) in either 1-butyl-1-methylpyrrolidinium bis(trifluoromethyl-sulfonyl)imide ([BMP][TFSI], IoLiTec,  $> 99.5\%$ ) or 1-butyl-1-methylpyrrolidinium dicyanamide ([BMP][DCA], IoLiTec,  $> 98\%$ ) (see Fig. 1).

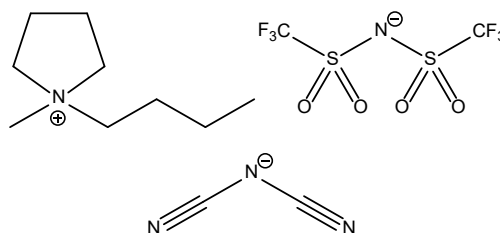


**Figure 1:** Structures of [BMP]<sup>+</sup> (top left), [TFSI]<sup>-</sup> (top right) and [DCA]<sup>-</sup> (bottom).

For the herein presented electrochemistry experiment, a standard three-electrode setup was used, including a counter electrode (CE), a WE, and a reference electrode (RE), all of which interfaced with a Nordic Electrochemistry ECI-200 potentiostat. We utilized Pt wires as CEs, ensuring that their surface areas were substantially larger than the one of the WEs to avoid kinetic limitations. Various materials were selected as WE, including Au, Pt, Ag, Cu and glassy carbon, each with a defined surface area to ensure consistency across experiments. The RE consisted of a Ag wire immersed in a glass vessel filled with either [BMP][TFSI] or [BMP][DCA] ILs and a Vycor frit for the separation from the solution under investigation. To maintain an inert environment and to prevent any contamination, all experiments were performed in a glove box under Ar atmosphere.

Cyclic voltammetry (CV) was employed to determine the reduction potential of Tb by sweeping the voltage from  $-3$  to  $1\text{ V}_{\text{vs. Ag RE}}$  while simultaneously recording the resulting current flow. For each IL, two CVs were recorded, i.e., a baseline CV with the pure IL and another CV with dissolved  $\text{Tb}(\text{NO}_3)_3$ . The CVs of [BMP][TFSI] and [BMP][DCA] were performed at room temperature (RT), while [BMP][TFSI] was also tested at  $70^\circ\text{C}$ . Each of these three different experimental conditions was replicated across all five types of WEs, adjusting the upper voltage sweep range for Ag and Cu electrodes to  $0.5$  and  $-1.5\text{ V}_{\text{vs. Ag RE}}$  respectively to prevent oxidation of the electrode material.

After determining the reduction potential of Tb, ED experiments were carried out by applying a constant potential of  $-1.8\text{ V}_{\text{vs. Ag RE}}$  for different experimental times. The thus prepared Tb-coated WE was washed sequentially with [BMP][DCA], dimethylformamide (Sigma-Aldrich,  $> 99.8\%$ ) and isopropanol (Scharlau anhydrous,  $> 99.8\%$ ) to remove any remaining IL.

Scanning electron microscopy (SEM, NVision 40) and energy-dispersive X-ray spectrometry (EDX, Oxford instruments X-Max<sup>N</sup>) analyses were conducted to assess the morphology of the Tb film and its elemental composition, respectively.

## Results and discussion

A distinct peak at  $-2.6 V_{vs. Ag RE}$ , observed in all conducted CVs, is attributed to the reduction of Tb(III), as evident by the comparison of the CVs of pure IL to the ones containing Tb (Fig. 2). A pronounced downward trend close to  $-3 V_{vs. Ag RE}$  indicates an increasing decomposition of the IL. Among the five tested WE materials, Au consistently yielded the most distinct CV peaks. However, the choice of WE material did not alter the position of the peak associated with the reduction of Tb(III).

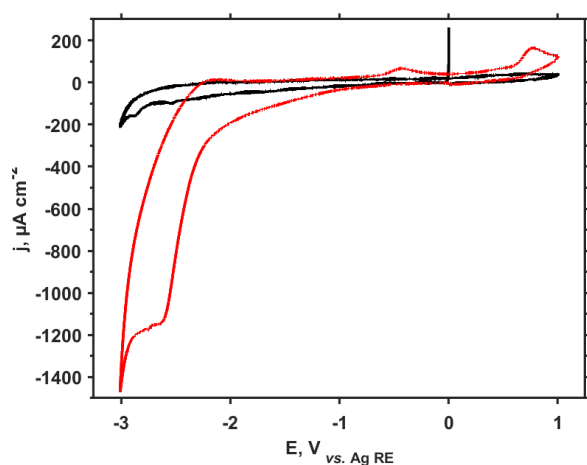


**Figure 2:** First cycle of the CV of pure [BMP][TFSI] (black) and of Tb in [BMP][TFSI] (red), both recorded using a Au WE at a scan rate of  $50 \text{ mV s}^{-1}$  and at room temperature.

Of the three experimental conditions described before, [BMP][TFSI] at RT provided the most distinct current peaks, whereas experiments with [BMP][DCA] resulted in barely visible current peaks, whereas heated [BMP][TFSI] led to only rather small peaks.

Based on these CVs, a reduction voltage of  $-1.8 V_{vs. Ag RE}$  was chosen for the ED of Tb on a Au WE in [BMP][TFSI] at RT. The first ED was performed with a deposition time of 56 h, resulting in a film with a non-uniform, porous surface featuring several large cracks (Fig. 3, left). By reducing the deposition time to only 2 h, a thinner film was obtained (Fig. 3, right). The dendritic structures observed in case of both Tb films are attributed to the nucleation process of Tb during ED [7].

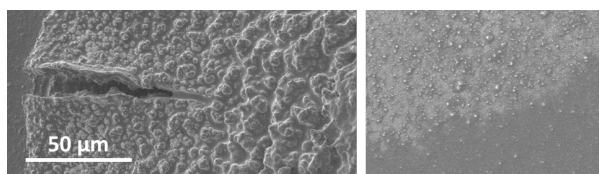


**Figure 3:** SEM images (same scale) of the Tb films as obtained by ED of Tb(III) from [BMP][TFSI] on a Au WE by applying a constant voltage of  $-1.8 V_{vs. Ag RE}$  for 56 h (left) and 2 h (right) at RT.

Comparing the films from 6-h-long EDs at RT (Fig. 4, left) and at  $70^\circ\text{C}$  (Fig. 4, right), the latter showed a smoother surface with fewer cracks, although with numerous dendrites.

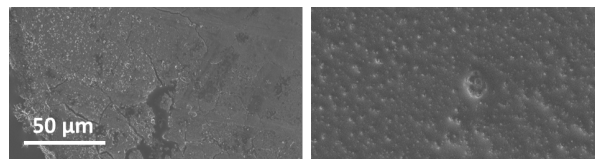


**Figure 4:** SEM images (same scale) of the Tb films as obtained by ED of Tb(III) from [BMP][TFSI] on a Au WE by applying a constant voltage of  $-1.8 V_{vs. Ag RE}$  for 6 h at RT (left) and at  $70^\circ\text{C}$  (right).

Further EDs from the two ILs at RT revealed that the film deposited from [BMP][TFSI] (Fig. 5, left) shows fewer dendrites than the one from [BMP][DCA] (Fig. 5, right). However, the Tb layer in between the dendrites of the film deposited from [BMP][DCA] was thinner than the one deposited from [BMP][TFSI]. This was also confirmed by EDX analysis (not shown here). This indicates the potential of [BMP][DCA] in the ED of thin Tb films.

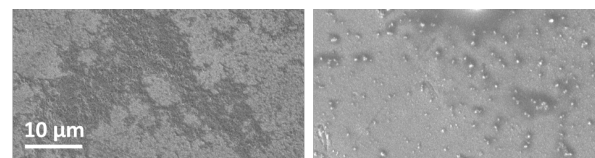


**Figure 5:** SEM images (same scale) of the Tb film as obtained by ED of Tb(III) from [BMP][TFSI] (left) and [BMP][DCA] (right) on a Au WE by applying a constant voltage of  $-1.8 V_{vs. Ag RE}$  for 2 h at RT.

EDX analysis confirmed the presence of Tb in the films but also indicated contaminants, such as C, O and F, likely arising from co-deposited or residual IL.

## Conclusions and outlook

An ED over a duration of 2 h successfully yielded thin Tb films. However, enhancing the uniformity of film thickness remains a major challenge. Among the tested ILs, [BMP][DCA] emerged as a favorable choice for future depositions due to its superior homogeneity in terms of thickness compared to [BMP][TFSI]. To achieve more accurate measurements of film thickness and gain insights into the oxidation state of Tb, advanced analytical techniques such as Rutherford backscattering or X-ray photoelectron spectroscopy is envisaged.

## References

- [1] S. Lehenberger et al., *Nuc. Med. Biol.*, **38**(6), 917 (2011)
- [2] K. Eckerman et al., *Ann. ICRP*, **38**(3), 7 (2008)
- [3] C. Müller et al., *Eur. J. Nucl. Med. Mol. Imaging*, **41**(3), 476 (2014)
- [4] D. Filosofov et al., *Nucl. Med. Biol.*, **94**, 19 (2021)
- [5] D. R. Lide, *CRC Handbook of Chemistry and Physics*, CRC Press, Boca Raton, 2006
- [6] T. Shubin et al., *RSC Adv.*, **8**, 3789 (2018)
- [7] G. Gunawardena et al., *J. Electroanal. Chem.*, **138**, 225 (1982)

# Production of Tb/Pd targets and their characterization

N. Cerboni (ETHZ & PSI), M. Wörle (ETHZ), P. Steinegger (ETHZ & PSI), E. A. Maugeri (PSI)

## Introduction

First introduced by Usoltsev *et al.* in 2012 [1], molecular plating (MP) followed by coupled reduction (CR), i.e., a thermal treatment at high temperatures under H<sub>2</sub> atmosphere, is a promising combination for the preparation of thin films of metallic radioisotopes of lanthanides (Lns) or actinides (Ans) and platinoids (i.e., Ru, Rh, Pd, Os, Ir, Pt). During the CR reaction, the Lns/Ans are reduced to their metallic state and diffuse into the platinoid bulk, forming a thermodynamically stable crystalline material [2]. Besides being stable in air, the generated samples exhibit high thermal and electrical conductivity, as well as chemical and mechanical stability. These properties are beneficial if the metallic samples are used as targets to produce superheavy elements.

This work reports on the attempt to produce Tb/Pd targets, by the combination of MP and CR [1]. The surface morphology of the obtained samples was investigated by scanning electron microscope (SEM). In addition, the phase identification of the formed crystalline structure(s) was performed for the first time by X-ray diffraction (XRD).

## Experimental

A comparably thick film of Tb(III) (loading: 0.92 mg/cm<sup>2</sup>) was deposited onto a 12.5 μm thick Pd foil from dimethylacetamide via MP, applying a constant current density of 0.8 mA/cm<sup>2</sup> for 90 min (exp-1.1). Afterwards, parts of the plated Pd foil were heated at different temperatures and for different treatment times under a H<sub>2</sub> gas flow of 25 mL/min. One part was heated at 1000°C for 4 h (exp-1.2), while another part was heated at 1100°C for 24 h (exp-1.3). In addition, a piece of the bare Pd foil was heated at 1100°C for 24 h (exp-1.4) and served as reference. The produced samples are summarized in Tab. 1. These samples were used to investigate their surface morphology by means of SEM and crystalline phases by XRD.

**Table 1:** Summary of all produced samples and their corresponding experimental parameters, i.e., the Tb loading, heating temperature, and time.

Name	Tb loading	Temperature	Time
exp-1.1	0.92 mg/cm <sup>2</sup>	-	-
exp-1.2		1000°C	4 h
exp-1.3		1100°C	24 h
exp-1.4	-		

## Results and discussion

The surface morphology of sample exp-1.1 is presented in Fig. 1(a). Expectedly, interconnected cracks are visible throughout the surface of the molecular plated film [3]. In addition, parts of the deposited layer (not shown here) are detached, indicating poor adherence between the deposited film and the Pd backing. This is ascribed to the comparably large amount of plated Tb in comparison to common layer thicknesses produced by MP in a single step (usually < 0.8 mg/cm<sup>2</sup> [3]).

Similar structural features to the initially plated film of exp-1.1 are visible on the surface of exp-1.2 (see Fig. 1(b)), suggesting an incomplete CR reaction due to a too short heating time or not being subjected to high enough temperatures. On the other hand, a more even surface with clearly visible grain boundaries – similar to exp-1.4 (see Fig. 1(d)) – is obtained by increasing both the heating time and temperature (see Fig. 1(c)). This indicates that the CR reaction was indeed successful, and all Tb seems to be reduced and diffused into the Pd bulk.

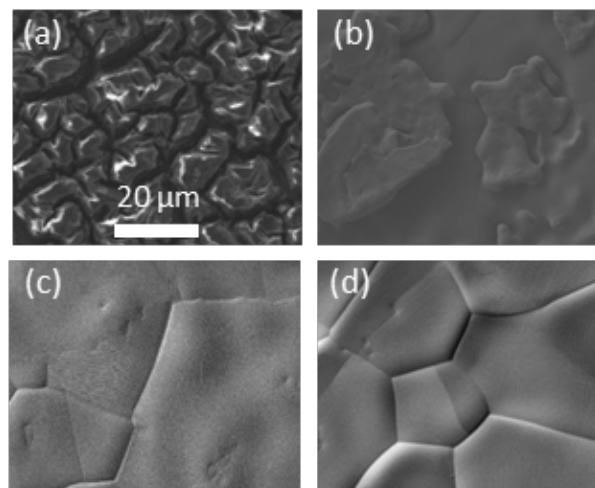


**Figure 1:** SEM images of (a) exp-1.1, (b) exp-1.2, (c) exp-1.3, and (d) exp-1.4. The scale, and therefore the resolution, is the same for all four SEM images.

Fig. 2 shows the XRD pattern of sample exp-1.2, recorded in reflection mode and with Mo as an X-ray source. Three different crystalline phases were found: first, a set of peaks that matches the face-centred cubic crystal structure of Pd (\*) [4], secondly, one that is in line with the primitive cubic crystal structure of the intermetallic compound (IMC) TbPd<sub>3</sub> (+) [5] and, lastly, one set that corresponds to the body-centred cubic

crystal structure of  $\text{Tb}_2\text{O}_3$  (-) [6]. The fact that Pd,  $\text{TbPd}_3$ , and  $\text{Tb}_2\text{O}_3$  are present simultaneously indicates that the Tb compounds deposited during MP first transform into an oxide before they are reduced and form the IMC  $\text{TbPd}_3$ . The latter is easily formed because there is sufficient Tb at the interface between the Pd foil and the Tb film to achieve an exact stoichiometric Tb/Pd atomic ratio 1 to 3.

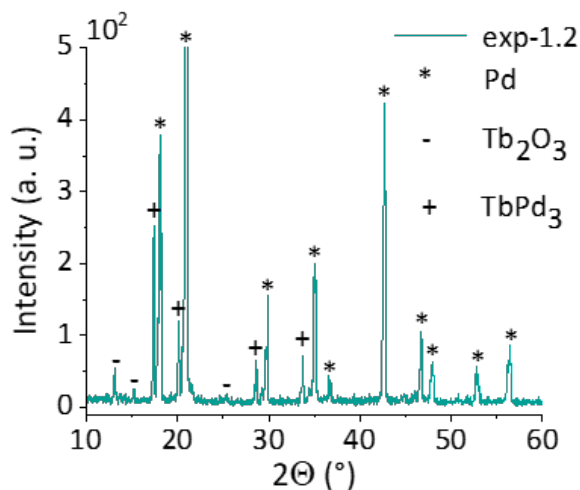


**Figure 2:** XRD patterns of exp-1.2 measured in reflection mode (MoK $\alpha$ 1-radiation with  $\lambda = 0.70930 \text{ \AA}$ ). The three identified crystalline phases are (\*) the Pd face-centered cubic crystal lattice, (+) the primitive cubic crystal structure of  $\text{TbPd}_3$ , and (-) the body-centered cubic crystal lattice of  $\text{Tb}_2\text{O}_3$ .

On the other hand, the XRD pattern of exp-1.3 (see green line in Fig. 3) was measured with other experimental parameters, i.e., in transmission mode and with Cu as an X-ray source, and is, therefore, not comparable with Fig. 2. Nevertheless, only one set of peaks can be identified. The absence of the peaks corresponding to  $\text{TbPd}_3$  and  $\text{Tb}_2\text{O}_3$  suggests that all of the Tb(III) was reduced and diluted in the Pd bulk. In comparison to exp-1.4 (see orange line in Fig. 3), the reflections of sample exp-1.3 are shifted toward lower  $2\theta$ -values. This confirms an increase in lattice constant and, hence, the formation of a Tb/Pd solid solution, which is consistent with earlier work [7]. After thermal treatment, the cell parameter of exp-1.4 could be determined as  $a(\text{Pd}) = 3.8893(2) \text{ \AA}$ , and for exp-1.3, as

$a(\text{Tb/Pd}) = 3.9198(3) \text{ \AA}$ , following a Rietveld refinement of both patterns. Due to the larger atomic radius of Tb compared to the one of Pd [8], it is indeed expected that it will expand the face-centred cubic lattice of Pd, indicating an enlarged unit cell. The obtained values closely match the ones determined by others [7].

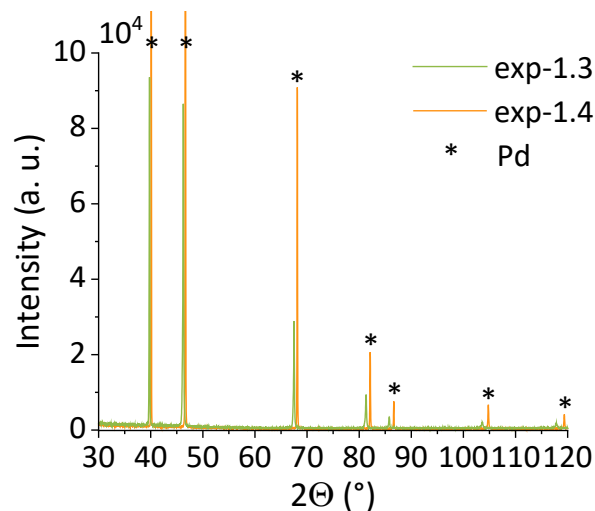


**Figure 3:** XRD patterns of exp-1.3 (green) and exp-1.0 (orange) measured in transmission mode (CuK $\alpha$ 1-radiation with  $\lambda = 1.54060 \text{ \AA}$ ). The face-centered cubic crystal structure of Pd (\*) was successfully identified.

An analysis of the oxidation state of Tb of the samples exp-1.1, exp-1.2, and exp-1.3 by means of X-ray photoelectron spectroscopy is on-going.

## References

- [1] I. Usoltsev et al., *Nucl. Instrum. Meth. A*, **691**, 5 (2012)
- [2] B. Erdmann, Ph.D. thesis, Gesellschaft für Kernforschung GmbH (1971)
- [3] C. E. Düllmann et al., *J. Radioanal. Nucl. Chem.*, **332**, 1505 (2023)
- [4] A. W. Hull, *Phys. Rev.*, **17**, 571 (1921)
- [5] I. R. Harris et al., *J. Less Common Met.*, **9**, 263 (1965)
- [6] W. H. Zachariasen, *Nor. J. Geol.*, **9**, 310 (1927)
- [7] Y. Sakamoto et al., *J. Less Common Met.*, **159**, 191 (1990)
- [8] <https://hbcpc.chemnetbase.com/contents/ContentsSearch.xhtml?dswid=9033> (accessed in 12/2023)

## Investigation of a Pd-Gd intermetallic target

X. Kou (ETHZ & PSI), N. Cerboni (ETHZ & PSI), E. Mueller (PSI), M. Makowska (PSI), M. Muntwiler (PSI), P. Steinegger (ETHZ & PSI), E. A. Maugeri (PSI)

### Introduction

Intermetallic targets exhibit superior electrical and thermal conductivity, alongside enhanced mechanical stability. These properties are particularly advantageous for stationary targets employed in the synthesis of super-heavy elements. A suitable method for producing such targets has been proposed, involving the application of molecular plating (MP) to coat a noble metal backing foil (i.e., Pd), which acts as a catalyst in the subsequent high-temperature treatment in a flow of pure hydrogen [1]. The co-called *coupled reduction* leads to the reduction of the plated lanthanide/actinide element before it diffused into the underlying backing foil. It was assumed that this process results in the formation of an intermetallic compound with the host metal [2]. Employing this methodology, a  $^{243}\text{Am}/\text{Pd}$  target was produced and then tested with an intense  $^{48}\text{Ca}$  ion beam [3]. A diffusion of Am through the Pd foil was demonstrated by means of alpha spectroscopy. Based on these findings, the authors inferred the intermetallic nature of the resulting target. However, the then gathered data alone does not provide conclusive proof for the formation of either an intermetallic compound or a simple alloy. Therefore, appropriate characterization techniques are needed to clarify the true nature of the metal-metal mixture. Here, we present the identification and characterization of a Gd-Pd intermetallic phase, as produced by MP in combination with the coupled reduction method.

### Experimental

The conducted molecular plating experiments utilized a conventional two-electrodes setup, with *N,N*-dimethylacetamide (99.5%, Sigma-Aldrich) as the solvent. Gadolinium nitrate hexahydrate (99.999%, Sigma-Aldrich) was used as the Gd source. A galvanostatic method was employed ( $0.8 \text{ mA cm}^{-2}$  for 1.5 h) under ambient conditions. Two distinct Pd foils were utilized, characterized by their respective thicknesses:  $25 \mu\text{m}$  (99.95 %, GoodFellow) and  $12.5 \mu\text{m}$  (99.95 %, GoodFellow), as backing material for the targets. The rationale for reducing the thickness from  $25 \mu\text{m}$  to  $12.5 \mu\text{m}$  in the later stage of this study lies in its effectiveness in significantly enhancing the mass loading of Gd, while not proportionally increasing the quantity of materials deposited during the molecular plating process. In the experiment utilizing a  $25 \mu\text{m}$ -

thick Pd foil, a theoretical Gd mass loading was designed to be 3.4 at. %. This was primarily aimed at the initial testing of molecular plating with milligram amount of Gd and the subsequent coupled reduction process. For the  $12.5 \mu\text{m}$  Pd foil, the desired Gd content for the final target was set at 8 at. %.

After the MP, the dried sample (desiccator) was placed within a stainless-steel tube and thermally treated for a specified time under a hydrogen flux of  $25 \text{ mL/min}$  at either  $1100^\circ\text{C}$  (for  $25 \mu\text{m}$ -thick sample) or  $1050^\circ\text{C}$  (for  $12.5 \mu\text{m}$ -thick sample, due to its severe melting at  $1100^\circ\text{C}$ ). After the heat treatment, the Pd-Gd sample was retrieved without any additional processes. Besides, a pure Pd foil with the same thickness, as reference sample, was subjected to the same thermal treatment.

**Table 1:** Sample numbers and corresponding characteristics (MP: molecular plating; CR: coupled reduction).

Sample	Pd thickness	Preparation method
1	25 $\mu\text{m}$	MP on Pd
2		MP on Pd, CR ( $1100^\circ\text{C}$ , 2h)
3		MP on Pd, CR ( $1100^\circ\text{C}$ , 24h)
4	12.5 $\mu\text{m}$	MP on Pd
5		MP on Pd, CR ( $1050^\circ\text{C}$ , 24h)
6		Lamella from Sample 5 by FIB
Reference		Pure Pd, CR ( $1050^\circ\text{C}$ , 24h)

The synthesized Pd-Gd sample underwent detailed characterization by means of scanning electron microscopy (SEM) and energy dispersive X-ray spectroscopy (EDX). To assess the Gd distribution in the sample's axial dimension, a lamella was extracted using the Focused Ion Beam (FIB) technique with a Ga ion source. Conclusively, the lamella was fixed onto a modified polyether ether ketone (PEEK) tip. Phase identification and Gd distribution within the sample were determined through micro-X-ray diffraction ( $\mu\text{-XRD}$ ) and micro-X-ray fluorescence ( $\mu\text{-XRF}$ ), available at the microXAS beamline of the Swiss Light Source (SLS) at PSI. High-resolution 2D sample scans were taken utilizing a precision sample stage yield projection map which show the crystallographic phases and atom distributions. All aforementioned characterizations

used transmission mode with a specific X-ray wavelength of 0.68499 Å. Besides, micro-X-ray photoelectron spectroscopy ( $\mu$ -XPS) measurements under UHV condition was done at the PEARL beamline of the SLS with an X-ray energy of 200 eV to study the oxidation state of Gd on the sample's surface after coupled reduction. To prevent any ambiguity, the seven samples discussed in this report are systematically listed in Table 1.

## Results and discussion

The SEM image depicting the deposit in the central region of Sample 1 is illustrated in Figure 1a. This image clearly demonstrates the existence of numerous small islands-like formations. After coupled reduction for 2 h and 24 h, changes in the morphology of the plated sample were observed, as depicted in Figures 1b and 1c, respectively. During this process, the 'islands-like' deposits gradually decreased in prominence. Conversely, the Pd surface, which had been previously covered in the central region of the sample, became exposed. It is hypothesized that the Gd-containing islands might have partially amalgamated with the Pd.

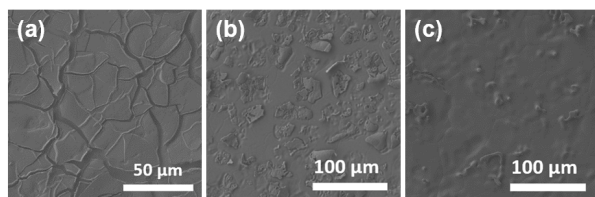


**Figure 1:** SEM images of central regions on (a) Sample 1, (b) Sample 2, and (c) Sample 3.

In order to know whether the Gd atoms diffused into the interior of the Pd foil or merely remained on its surface, Sample 4-6 were produced. SEM images of post-molecular plating (Sample 4) and post-coupled reduction (Sample 5) states of the sample are presented in Figure 2a and 2b, respectively. Together with the result from yield measurement (60.5%), the intrinsic concentration of the Pd-Gd sample is estimated to be around 5 at. %.

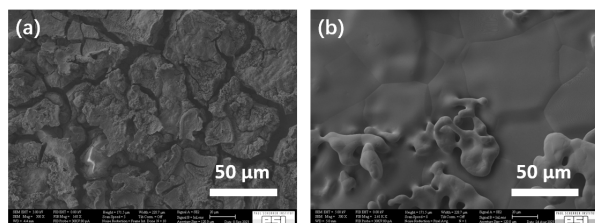


**Figure 2:** SEM images of central regions on (a) Sample 4 and (b) Sample 5.

A lamella was cut with FIB milling from a flat region of the Sample 5 and mounted on a PEEK tip, named as Sample 6. The fluorescence intensity map of Gd obtained via  $\mu$ -XRF of Sample 6 (not shown here) reveals a relatively homogenous distribution of Gd along a selected transect in the thickness direction. The XRD patterns integrated through the selected regions in Samples 6 and 5 are shown in Figure 3a and 3b, respectively. The Pd peaks show a minor shift

towards the low angle region relative to the peak positions of the reference sample, which can indicate a formation of a solid solution. Notably, Samples 5 and 6 exhibit several peaks that coincide with the position of the characteristic peaks of the intermetallic compound  $\text{GdPd}_3$ , as documented in literature [4]. The presence of  $\text{Gd}_2\text{O}_3$  peaks was noted exclusively in Sample 5, suggesting a predominant oxygen localization on the sample's residual islands. Given the presence of peaks corresponding to the intermetallic phase within the lamella, it can be inferred that the  $\text{GdPd}_3$  compound is distributed in the entire sample. Further investigation on some undetermined peaks is still on-going.

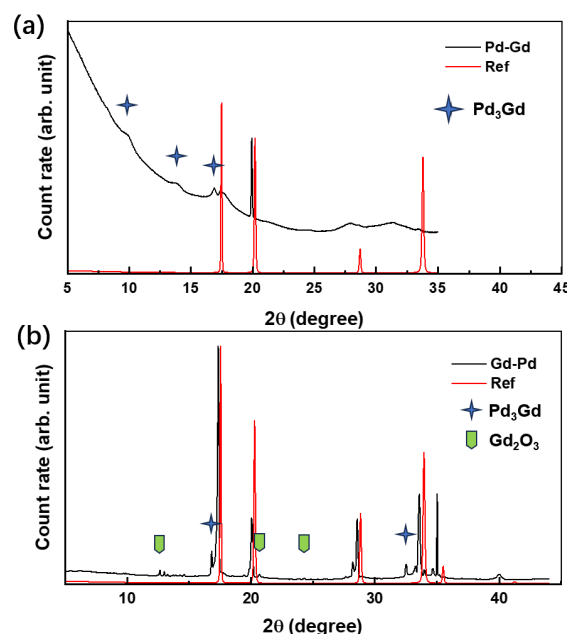


**Figure 3:** XRD pattern of selected regions in (a) Sample 6 and (b) Sample 5.

The results from  $\mu$ -XPS measurement (not shown here) also confirmed the presence of unevenly distributed  $\text{Gd}_2\text{O}_3$  on the sample's surface.

In summary, tests employing 25  $\mu\text{m}$  Pd backing and low Gd content, proved the feasibility of both plating milligram amount of Gd on Pd foil and the partial coupled reduction. For a comprehensive analysis of the phase composition and Gd distribution, a Pd-Gd sample with an enhanced Gd content (5 at. %) was synthesized.  $\mu$ -XRF analysis showed that the Gd atom distribution across the thickness was nearly uniform. Utilizing  $\mu$ -XRD, the emergence of a  $\text{GdPd}_3$  intermetallic phase was identified. This intermetallic phase is sporadically distributed within the Pd-Gd solid solution matrix. Residual  $\text{Gd}_2\text{O}_3$  was observed on the reduced sample's surface by both  $\mu$ -XRD and  $\mu$ -XPS.

## References

- [1] H. Kleykamp et al., *J. Nucl. Mater.*, **201**, 193 (1993)
- [2] I. Usoltsev et al., *Nucl. Instrum. Methods Phys. Res., Sect. A*, **691**, 5 (2012)
- [3] I. Usoltsev et al., *Nucl. Instrum. Methods Phys. Res., Sect. B*, **318**, 297 (2014)
- [4] S. Malik et al., *Bull. Mater. Sci.*, **6**, 263 (1984)

# Adsorption and separation of lanthanides by amido-type adsorbent

X. Pan (SJTU & PSI), Đ. Cvjetinović (PSI), J. Petrović (PSI), M. Würtenberg (PSI), D. Schumann (PSI)

## Introduction

Rare earth elements (REEs) have significant applications in various fields, such as catalysis, optoelectronics, nuclear medicine and as magnetic materials [1-3]. Due to their rarity and high costs, studying the adsorption behavior of lanthanide elements in solid-liquid systems is essential for the efficient utilization and recovery of these REEs. The separation of lanthanides (Ln) can serve as simulation for the investigation of lanthanide-actinide (An) separation, facilitating a deeper comprehension of the differences in chemical properties and behavior between these two-element series. Ion exchange is a promising technique for the recovery and separation of lanthanides due to the facile and economical operation [4].

In this study, an amide polymeric material was synthesized by the reaction of cyclic anhydride with an amino-type polypropylene (PP) nonwoven, and the adsorbent obtained was used for the adsorption and intergroup separation of lanthanide ions.

## Experimental

### Adsorbent synthesis

The preparation of adsorbent PP-g-GMA@EDA/SA (PGES) was based on radiation grafting and chemical modification method, according to the previous work [5, 6]. Two steps were included. In the first part,  $^{60}\text{Co}$  was utilized as the  $\gamma$ -ray source for the irradiation-induced copolymerization, with glycidyl methacrylate (GMA) as the graft monomer and PP nonwoven as the substrate. Intermediate PP-g-GMA was obtained after 5 kGy dose irradiation. In the second step (chemical modification), the active epoxy group of GMA reacted additionally with the amino group of ethylenediamine (EDA) in the isopropyl alcohol solvent under 70°C, and PP-g-GMA@EDA was synthesized by the amination modification. Through further amide condensation reaction with succinic anhydride (SA), the adsorbent PP-g-GMA@EDA/SA (PGES) containing amide and carboxyl group was finally obtained.

### Batch experiments

Sm(III), Eu(III), Gd(III), Tb(III), Ho(III) and Yb(III) were selected as lanthanide (Ln) representatives. For each Ln(III), the initial solutions of 100 mg/L were diluted from the ICP standard solutions (1000 mg/L). Freshly prepared  $\text{HNO}_3$  and NaOH solutions were used to adjust the pH value in the range from 2.0 to 4.0. The adsorption tests were evaluated using  $5.0 \pm 0.3$  mg PGES with 1.0 mL Ln(III) aqueous solution at a certain pH value in a 2 mL centrifuge tube. Samples were shaken for 16 hours at room temperature. After the adsorption, supernatant of each sample was extracted and diluted 10 times using 2 wt.-%  $\text{HNO}_3$ . The initial and the residual Ln(III) concentration in the solution were measured using ICP-OES. The distribution coefficient ( $K_d$ , mL/g) of each nuclide in the adsorbent and solution was calculated by Eq. (1):

$$K_d = \frac{C_0 - C}{C} \times \frac{V}{M} \quad (1)$$

where,  $C_0$  (mg/L) and  $C$  (mg/L) are the concentration in initial solution and after adsorption,  $V$  (mL) is the solution volume, and  $M$  (g) is the adsorbent mass used in each sample.

**Table 1** Mass distribution coefficients ( $\log K_d$ ) for Ln(III) ions in different acidity solution.

pH	Sm(III)	Eu(III)	Gd(III)	Tb(III)	Ho(III)	Yb(III)
2.0	2.94± 0.049	3.46± 0.035	2.84± 0.102	2.43± 0.011	2.32± 0.042	3.51± 0.046
2.5	4.65± 0.013	4.58± 0.043	4.16± 0.023	4.11± 0.057	3.91± 0.090	4.19± 0.131
3.0	4.92± 0.025	5.02± 0.041	4.71± 0.111	5.01± 0.042	4.17± 0.091	4.59± 0.033
3.5	4.65± 0.056	4.95± 0.082	4.96± 0.033	4.44± 0.121	4.45± 0.206	4.27± 0.098
4.0	4.59± 0.118	4.75± 0.027	4.54± 0.131	4.22± 0.086	4.44± 0.239	4.11± 0.149

## Results and Discussion

For the An/Ln separation by solid-liquid systems, the acidity of aqueous phase is an important parameter [7]. Adsorption experiments were conducted at different initial solution acidities in order to establish the optimum separation system of and Ln(III) using PGES. Table 1 reflects the influence of solution pH on the

Ln(III) ions uptake using PGES with the data given logarithmically ( $\log K_d$ ). For each Ln(III), the distribution coefficients present a tendency to rise and then fall with increasing pH from 2 to 4. The lowest  $K_d$  values at pH 2 are due to the excessive free  $H^+$  ions in the solution, which occupy adsorption sites for cations, carboxylic acid group, on the adsorbent. The best adsorption performance occurred between pH 3-3.5 with  $\log K_d$  values reaching more than 5, indicating the excellent lanthanide recovery ability by the adsorbent PGE. At pH 3.5, as the atomic number increased for  $^{62}\text{Sm}$  to  $^{70}\text{Yb}$ , the corresponding  $K_d$  value of each element increased from  $^{62}\text{Sm}$  to  $^{64}\text{Gd}$  and then decreased. This may be related to the lanthanide contraction property, which can be used to optimize the lanthanide intragroup separation, and further establish the lanthanide-actinium separation system.

### Conclusion

The adsorption of Ln(III) ions on the amide type adsorbent PGES was studied by batch technique in dependence of the pH. pH 3.0-3.5 is the best for lanthanide recovery from aqueous phase with  $\log K_d$

values around 5 using the developed ion exchanger. The intragroup separation of lanthanides is guaranteed because PGES exhibits different capture capacities for different elements at the same condition. In the following work, the recovery of lanthanide in complex aqueous environment will be further studied, and the establishment of separation system of lanthanides and actinides is also in the focus of our research.

### Acknowledgments

The financial supports of the National Natural Science Foundation of China [No.11975152] and [No. 12275177].

### References

- [1]. T. Ogata et al., *Hydrometallurgy*, **163**, 156-160 (2016)
- [2]. E. Chang et al., *Environ. Eng. Sci.*, **38**(3), 154-164 (2021)
- [3]. Y. Zhang et al., *J. Photoch. Photobio. C*, **20**, 71-96 (2014)
- [4]. X. Zheng et al., *ACS Appl. Mater. Inter.*, **6**(22), 19840-19849 (2014)
- [5]. X. Pan et al., *Sep. Purif. Technol.*, **322**, 124123 (2023)
- [6]. X. Pan et al., *Sep. Purif. Technol.*, **297**, 121450 (2022)
- [7]. Y. Cai et al., *J. Hazard. Mater.*, **405**, 124214 (2021)

# Production of mass-separated $^{169}\text{Er}$ : a focus on separation efficiency

C. Duchemin, T. Stora, C. Crepieux, M. Inzamam, L. Lambert, C. Bernerd, R. Rossel (CERN), U. Köster (ILL), E. Renaldin (UniBe & PSI), N. P. van der Meulen, Z. Talip (PSI)

## Introduction

The beta emitter Er-169 has promising decay properties ( $t_{1/2}$ : 9.39 d,  $E\beta_{av}$ : 100 keV) toward Targeted Radionuclide Therapy (TRT). Er-169 can be produced by neutron capture using enriched  $^{168}\text{Er}_2\text{O}_3$  targets in a nuclear reactor. However, this route is unsuitable for TRT due to the low specific activity of Er-169 produced.

The first proof-of-concept study regarding the production of mass-separated Er-169 was performed using electromagnetic isotope separation [1]. In another previously published study, collected Er-169 activities were increased up to a factor of four by combining surface ionization and resonant laser ionization [2]. As a follow-up, this study aims to perform a systematic study to increase the separation efficiency of Er-169.

## Material and Method

Three ampoules with  $\text{Er}_2\text{O}_3$  enriched to 98% in Er-168 (ISOFLEX) were prepared at PSI and irradiated at ILL, Grenoble, in 2023 to continue the investigation on the efficiency optimization for the mass separation of Er-169 at the CERN-MEDICIS offline mass separator facility. Based on the previous mass separation of Er-169 from Er-168 performed in 2018, it is known that the  $\text{Er}^+$  current from the ion source has to be limited not to lose efficiency, and a mass separation duration of about 1 week shall be considered for the planning.

Two samples containing 1 mg and one sample of 5.1 mg Er were irradiated in the ILL reactor and shipped to CERN-MEDICIS. All three samples were measured by  $\gamma$ -ray spectrometry before opening the ampoules and after the opening and processing of the target material. The measurements were performed using an HPGe detector (Mirion Technologies) and the APEX acquisition and data analysis system. Each sample geometry is modeled using the LabSocs/ISOCS software to compute the corresponding efficiency curve.

The CERN-MEDICIS team worked on an optimized process to extract the Er from the ampoule with the best efficiency, by avoiding the risk of contamination and avoiding the presence of quartz pieces in the final sample to be loaded inside the container of the ISOL target.

## Results and Discussion

*1<sup>st</sup> sample:*

It arrived at CERN on 06.07.2023 with an activity of 2.9 GBq. Before opening, each ampoule was cleaned using  $\text{HNO}_3$ , ethanol and water in an ultrasonic bath. The presence of trace quantities of Yb in the target material led to the co-production of Yb-169 ( $t_{1/2}$ : 32 d) due to the high thermal neutron capture cross-section of Yb-168 ( $\sigma$ : 2400 b). Since Er-169 has the same gamma-ray peaks (109.78 keV, 0.0014%) as Yb-169 (109.78 keV, 17.93%) with much lower intensity, it complicates precise Er-169 activity measurements using  $\gamma$ -ray spectrometry. Therefore, the transfer yield was determined based on the activity ratio of the co-produced Er-171 and Er-172 (Figure 1), considering they have the same transfer yield.



**Figure 1:** Karlsruhe nuclide chart showing the production of Er-169, Er-171 and Er-172.

This first sample was processed using only ethanol and very low contracted  $\text{HNO}_3$  as the final flush. It was aimed to transfer target material without dissolving it. The transfer efficiency was calculated to be 47%.

The mass separation was performed between 11.07. and 14.07.2023 by combining surface ionization and laser ionization. On 14.07. an issue with a water-cooling circuit of the facility stopped the collection prematurely. The collection foil was retrieved with an activity of 142 MBq collected, resulting in 15% efficiency, the highest separation efficiency achieved so far. This value has to be considered as lower limit considering the premature interruption of the collection.



**Figure 2:** Al-coated gold foil implanted with Er-169. The beam spot size and shape of the Er-169 implanted area (dark grey) are visible on the Al layer close to the center of the image.

#### *2<sup>nd</sup> sample:*

For the second sample, the same mass of  $\text{Er}_2\text{O}_3$  was irradiated at ILL. Following the experience and advice from PSI and ILL with the transfer of Er powder, the MEDICIS team has used concentrated (2 M and 4 M at 50°C)  $\text{HNO}_3$  for the transfer to increase the transfer efficiency, which increased the activity at the start. This means the transfer efficiency had increased to 74%. Moreover, a new special sample oven design was used, which allows for more homogenous heating within the target container and previously showed an increased performance at ISOLDE. The separation was performed between 13.11. and 20.11.2023, again using surface and laser ionization. However, the separation efficiency at the end of the collection appeared to be only 1.2% with these parameters.

#### *3<sup>rd</sup> sample:*

A 5 mg  $\text{Er}_2\text{O}_3$  sample was irradiated as a third sample at ILL. The transfer method stayed the same as for the second attempt, but the target unit used for the first collection was reused for the third collection.

It was aimed to assess the impact of using highly concentrated  $\text{HNO}_3$  on separation efficiency. The transfer efficiency was 83(11)%. The separation was performed between 4.12. and 11.12.2023 using the same parameters (temperature, lasers, optics, high voltage) as used in the first collection. The efficiency obtained at the end of the collection was 0.1%, i.e., 100 times less than for the first collection.

### **Conclusion & Outlook**

Further investigations are required to increase the transfer efficiency by avoiding the use of concentrated  $\text{HNO}_3$ , which seems to impact the final collection and separation efficiency of Er-169 from enriched  $^{168}\text{Er}_2\text{O}_3$  powder. A preliminary idea is to modify the transfer system design by combining the current flushing system with an ultrasonic bath to allow more powder to be extracted from the vial by movement. The new target design recently achieved at CERN-ISOLDE will also be further studied, not only for Er-169 but also for other radionuclides being produced at CERN-MEDICIS.

### **Acknowledgment**

This research was supported by the European Union's Horizon 2020 research and innovation programme under grant agreement No. 101008571 (PRISMAP - The European medical radionuclides programme).

### **References**

- [1] R. Formento-Cavaier et al., Nucl Instruments Methods Phys Res Sect B Beam Interact with Mater Atoms, **463:468** (2019)
- [2] Z. Talip et al., Frontiers in Nuclear Medicine, 643175 (2021)

## Preliminary studies for the activity standardization of $^{167}\text{Tm}$

Y. Nedjadi (IRA), F. Juget (IRA), M. T. Duran (IRA), E. Renaldin (UniBe & PSI), C. Favaretto (PSI), C. Duchemin (CERN), T. Stora (CERN), N. P. van der Meulen (PSI), Z. Talip (PSI)

### Introduction

$^{167}\text{Tm}$  is considered as a theragnostic radionuclide due to its conversion/Auger electron emissions and gamma energy released through its decay. Previous studies have demonstrated its use as a bone-scanning agent by detecting its intense 207-keV gamma line [1]. To date,  $^{167}\text{Tm}$  production has been investigated using different projectiles [2]. It is worth mentioning that the most significant uncertainty in  $^{167}\text{Tm}$  production cross-section measurements derived from the uncertainty in the intensity of 207-keV gamma ray is 42% with 19% uncertainty. To perform precise emission intensity measurements, radionuclidically pure  $^{167}\text{Tm}$  samples are needed.

### Material and Method

#### *Production of Mass separated $^{167}\text{Tm}$ :*

$^{167}\text{Tm}$  was produced at the CERN-MEDICIS facility by irradiating natural Ta rolls with a 1.4 GeV proton beam delivered by the CERN-PS Booster between June 6<sup>th</sup> and 7<sup>th</sup>, 2023, followed by mass separation.  $^{167}\text{Tm}$  was implanted onto Al-coated gold foils for 32 hours and shipped to PSI. An activity of 18.5 MBq  $^{167}\text{Tm}$  was measured using HPGe, with a reference date at the end of the collection.

#### *Separation of $^{167}\text{Tm}$ :*

The Al-coated gold foil, containing  $^{167}\text{Tm}$ , was dissolved in 6 M HCl and further processed at PSI using chromatographic techniques. In particular,  $^{167}\text{Tm}$  was separated from Al using extraction (DGA) and cation exchange (Sykam) resins. The resultant solution was then concentrated using an extraction column (LN3), resulting in the activity being eluted in 1.5 mL of 0.1 M HCl. This separation was proven to be successful for the nearly complete removal of Al by the previous cold tests, which resulted in a final product containing < 0.2  $\mu\text{g}$  of Al as measured by ICP-OES.

#### *Preliminary activity standardization measurements:*

In June 2023, 1.5 g 7 MBq  $^{167}\text{Tm}$  in 0.1 M HCl solution was sent to IRA for exploratory activity standardisation tests. The main challenge for standardizing this isotope, which decays by electron capture, stems from the isomeric state of its daughter ( $^{167\text{m}}\text{Er}$ ), with a 2.269-s half-life. Its decay scheme is still poorly understood, and the main decay branch has a branching ratio with a typical relative uncertainty of 25%.

An aliquot of 0.2 g was taken from the stock solution and diluted by a factor of 17.5 to produce a solution (M167Tm2) for primary activity measurements. The remaining solution sent by PSI was diluted by a factor of 2.3, and the resulting solution (M167Tm1) was transferred into an IER ampoule to calibrate the reference ionization chamber and half-life measurement with a transportable ionization chamber. The largely diluted solution (M167Tm2) was used to prepare three sources for gamma spectrometry. Aliquots of this solution were also dispensed with a pycnometer to produce 14 liquid scintillation sources, with Ultima Gold and a 6.5% aqueous fraction, in frosted glass vials for the triple-to-double coincidence ratio (TDCR) and CIEMAT-NIST (CNET) measurements. Seven sources were quenched with increasing volumes (20 to 140  $\mu\text{L}$ ) of  $\text{CCL}_4$ . Two further unquenched sources were readied for  $4\pi\beta(\text{LS})\text{-}\gamma$  correlation coincidence counting with digital electronics. An extra solid source was prepared to determine the half-life by continuously monitoring the decay with a gamma counter.

### Results and Discussion

At the end of the radiochemical separation process (lasting 2 hours), a total of 8.3 MBq of Al-free  $^{167}\text{Tm}$  was obtained. HPGe-gamma spectrometry measurements showed that the  $^{167}\text{Tm}$  solution contained a  $^{168}\text{Tm}$  impurity. The impurity ratio (activity of  $^{168}\text{Tm}$  normalized to that of  $^{167}\text{Tm}$ ) was 0.01% when the solution was received by the IRA and grew to more than 1% a couple of months later.

Half-life measurements were carried out with an ionization chamber and two gamma counters (a NaI(Tl) well detector and a  $\text{CeBr}_3$  detector). In the latter case, gamma signals were processed with an amplifier and single-channel analyzer before being inserted into two inextensible dead-time imposition circuits. Analyses of all these decay measurements, using stochastic fits that assume the presence of a  $^{168}\text{Tm}$  impurity and take into account decay during measurement and uncertainties in timings and counting rates, predict half-life values compatible with each other, and close to that adopted by ENSDF (9.25(2) d).

The TDCR technique was implemented by defocusing, with the focus voltage varying from 560 to 280 V in steps of 40 V, grey filtering, with fifteen self-adhesive films of varying optical densities, as well as chemical

quenching with a focusing voltage set at 560 V. The counting times ranged from 300 s to 900 s, so the relative standard deviations of the triple coincidence count rates were lower than 0.1%. As for the CNET measurements, they were performed with a Tricarb 2700 TR counter, which uses a  $^{133}\text{Ba}$  source for determining the quench parameter (tSIE).

The computation of the double or triple detection efficiency relies on the knowledge of the energy deposits in the scintillant. Monte Carlo simulations with the Geant4 code and its Atomic Relaxation module were run to sample the nuclear decays of  $^{167}\text{Tm}$ , together with the associated atomic rearrangements, as well as the interactions of the gamma and X-rays with the scintillant cocktail and the consequent atomic rearrangements. These samplings were separated into two sets: a) the energy depositions arising from the decay of the isomeric state and b) the energy depositions from the electron capture and gamma cascades that do not transit through the isomeric state. Our efficiency calculation model takes advantage of this separation to correct adequately for the dead time effect associated with the decay of the metastable state.

$^{167}\text{Tm}$  presents a particular difficulty for the TDCR analysis. The difficulty is that the relationship between its double or triple detection efficiency and the triple-to-double-coincidence ratio is not bijective (see Figure 1 below). To overcome this problem transforms of the TDCR were used to establish a bijective relationship between the detection efficiencies and these transformed TDCRs. Corresponding codes have been written.

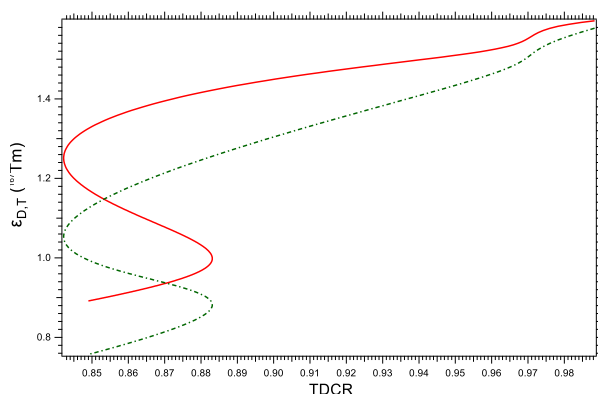


**Figure 1:** Variation of the  $^{167}\text{Tm}$  double and triple detection efficiencies with the TDCR.

## Outlook

Preliminary analyses of the TDCR measurements predict an activity concentration that was 4 % higher than the nominal value given by PSI. The TDCR measurements showed good internal coherence, with the relative deviation between the grey filtering and chemical quenching estimated at less than 0.75%. As pointed out earlier, the decay scheme of this isotope has branching ratios and emission probabilities with quite large uncertainties. However, uncertainty

calculations using Monte Carlo simulations with boundary decay scheme parameters showed that the propagation of the decay scheme uncertainties would contribute less than 4% to the total activity concentration. CNET calculations are well underway but not yet complete.

Analysis of digital coincidence measurements ( $4\pi\beta(\text{PS})-4\pi\gamma$  and  $4\pi\beta(\text{LSx2})-\gamma\text{x3}$  (CeBr<sub>3</sub>, CeBr<sub>3</sub>, NaI)) is in progress. The sole possible technique for standardizing this nuclide by  $\beta$ - $\gamma$  coincidences counting is the correlation counting method. A computer code for this technique is in the process of development.

## Acknowledgment

This research was supported by the European Union's Horizon 2020 research and innovation programme under grant agreement No. 101008571 (PRISMAP - The European medical radionuclides programme).

## References

- [1] Ando, A. et al., *European Journal of Nuclear Medicine*, **8**(10), 440-446 (1983)
- [2] E. Renaldin et al., *Frontiers in Chemistry*, **11**, 1-14 (2023)

# Production of $^{152}\text{Tb}$ and $^{169}\text{Yb}$ using medium energy cyclotron

S. Pasolini (PSI), E. Renaldin (UniBe & PSI), A. Sommerhalder (PSI), H. Zhang (PSI) N. P. van der Meulen (PSI), Z. Talip (PSI)

## Introduction

$^{152}\text{Tb}$  ( $t_{1/2}$ :17.5 h; EC,  $\beta^+$ : 100%) belongs to the terbium sisters ( $^{161}\text{Tb}$ ,  $^{155}\text{Tb}$ ,  $^{152}\text{Tb}$  and  $^{149}\text{Tb}$ ), also known as the “swiss army knife” of nuclear medicine. Considering their decay properties, they exhibit notable potential, being emerging radionuclides for theragnostic applications [1].

$^{152}\text{Tb}$  has been considered as a medical radionuclide for Positron Emission Tomography (PET). It could be potentially used for *in vivo* dosimetry to monitor  $^{149}\text{Tb}$  and  $^{161}\text{Tb}$  bio-distribution in radiotherapy. To date, its production has been investigated using charged particles, high-energy protons via spallation reactions, and heavy ions. The main limitation for  $^{152}\text{Tb}$  production via (p,n) reaction is the non-availability of the highly enriched  $^{152}\text{Gd}_2\text{O}_3$  target materials (commercially available  $^{152}\text{Gd}$  enrichment level is 30-35%). Here, we aim to investigate its production using medium energy protons with an isotopically enriched  $\text{Gd}_2\text{O}_3$  target.

$^{169}\text{Yb}$  is mainly used in brachytherapy. In this study, its production was investigated for a future project regarding the emission intensity measurements of its Auger electron emission.

## Materials and Methods

Enriched gadolinium-155 oxide ( $^{155}\text{Gd}_2\text{O}_3$ , enr. 91.9 %, ISOFLEX USA) served as target material for the  $^{152}\text{Tb}$  production, while  $^{169}\text{Yb}$  was obtained proton-irradiation of natural thulium oxide ( $\text{Tm}_2\text{O}_3$ , 99.999% ChemPUR, DE), a mono-isotopic element.

Target preparation consisted of pressing roughly 40 mg of oxide powder into disc-shaped pellets. The products are cylindrical pellets 6 mm in diameter and 0.3 mm in thickness, and they possess an average density of  $5.1 \text{ g/cm}^3$ .

Both productions were performed through proton irradiations using Injector II cyclotron of the Paul Scherrer Institute, triggering  $^{155}\text{Gd}(p,4n)^{152}\text{Tb}$  and  $^{169}\text{Tm}(p,n)^{169}\text{Yb}$  reactions.

The irradiation parameters were determined by theoretical calculations to maximize the production yield while reducing the radionuclidic impurities. The stopping range of ions in the target material was calculated using SRIM software. In the case of  $^{169}\text{Yb}$ , the experimental cross-section data were taken from the IAEA library (Figure 1) [2], while the  $^{152}\text{Tb}$  theoretical

cross-sections were retrieved from the TENDL 2023 library.

Once the optimum energy range for the irradiations was identified, the theoretical production yields were determined according to Otuka’s definition [3].

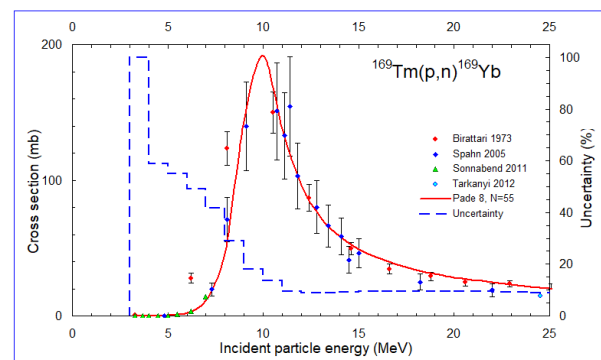


**Figure 1:** Experimental  $^{169}\text{Tm}(p,n)^{169}\text{Yb}$  cross section data including Pade fit (Figure is taken from ref 3).

10-minute and 5-minute irradiations were performed for the production of  $^{152}\text{Tb}$  and  $^{169}\text{Yb}$ , using proton currents of  $5 \mu\text{A}$  and  $18 \mu\text{A}$ , respectively. The proton beam was degraded to 40.4 MeV by means of the cooling water for  $^{152}\text{Tb}$  production. For  $^{169}\text{Yb}$  production, a Nb degrader of 3.4 mm thickness was used to decrease the proton energy to 10.6-MeV.

The spectra acquisition was performed through gamma-ray spectrometry with a high-purity germanium (HPGe) detector and the spectroscopy analysis was carried out using InterWinner software.

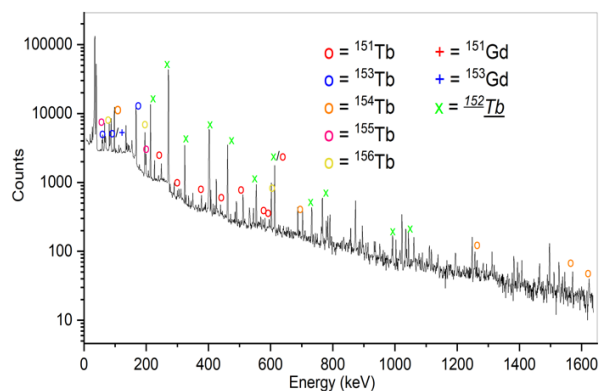
## Results and Discussion

Table 1 and Table 2 compare the experimental and theoretical activities for  $^{152}\text{Tb}$  and  $^{169}\text{Yb}$  production.

**Table 1:** Comparison of the theoretical and experimental end of beam (EOB) activities for  $^{152}\text{Tb}$ .

Samples	Theoretical EOB activity (MBq)	Measured EOB activity (MBq)	Radionuclidic purity
Tb1	$23.7 \pm 0.8$	$28.7 \pm 1.1$	64.19%
Tb2	$23.7 \pm 0.8$	$29.0 \pm 1.1$	76.69%

The main impurities found in the samples were due to  $^{151-155}\text{Tb}$  isotopes, which formed via (p,xn) reactions on  $^{155}\text{Gd}$  and other isotopic impurities of the enriched  $^{155}\text{Gd}_2\text{O}_3$  target. Figure. 2 shows that the main radionuclidic purity produced is  $^{151}\text{Tb}$ .



**Figure 2:** Gamma spectrum of proton-irradiated enriched  $^{155}\text{Gd}_2\text{O}_3$  target (counting time: 1917 s sample detector distance (SDD): 1 m).

**Table 2:** Comparison of the theoretical and experimental EOB activities for  $^{169}\text{Yb}$ .

Samples	Theoretical EOB activity (MBq)	Measured EOB activity (MBq)	Radionuclidic purity
Yb1	$83.1 \pm 0.8$	$69.5 \pm 0.9$	98.35%
Yb2	$83.1 \pm 0.8$	$79.4 \pm 0.8$	98.23%

The main impurity found in the proton-irradiated  $^{169}\text{Tm}_2\text{O}_3$  samples was due to  $^{168}\text{Tm}$  coming from (p,pn) reaction occurring on  $^{169}\text{Tm}$  (Figure 3). However, the measured activities were lower than the theoretical ones, and the sources of error could stem mainly from material losses and beam-centering uncertainties. Moreover, the target is not as ideal as the one considered in the theoretical calculations.

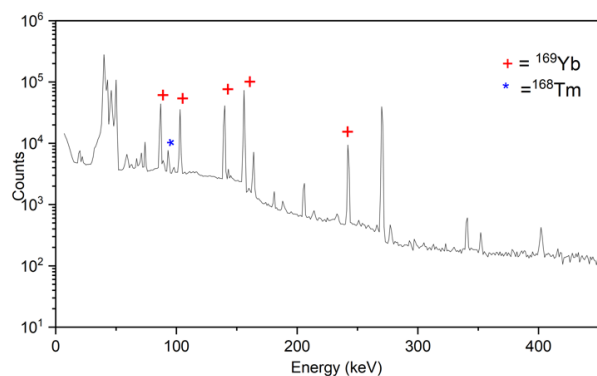


**Figure 3:** Gamma spectrum of proton-irradiated  $\text{Tm}_2\text{O}_3$  target (counting time: 237404 s, SDD:1 m).

## Conclusion

In this project, preliminary test irradiations were performed using PSI Injector II cyclotron to produce  $^{152}\text{Tb}$  and  $^{169}\text{Yb}$ . In all cases, the experimental results were in good agreement with the theoretical calculations.

The main outlook is the implementation of a better beam position monitoring system that could help reduce the experimental uncertainties. The next steps involve the development of a chemical separation method to obtain radionuclidically pure  $^{169}\text{Yb}$  and the investigation of  $^{152}\text{Tb}$  production using different

enriched  $\text{Gd}_2\text{O}_3$  targets. The latter will provide preliminary data for an offline mass separation process, which is considered as a next step to produce radionuclidically pure  $^{152}\text{Tb}$ .

## References

- [1] N. Naskar et al. "Theranostic Terbium Radioisotopes: Challenges in Production for Clinical Application". In: Front Med (2021)
- [2] <https://www-nds.iaea.org/medical/tm9p9yb0.html>
- [3] N. Otuka et al., *Radiochim. Acta*, 103 (2015)

# Cross-section measurements of proton-induced reactions on $^{nat}\text{Dy}_2\text{O}_3$ for the $^{161}\text{Ho}$ production with a medical cyclotron

E. Renaldin (UniBe & PSI), R. Zehnder (UniBe & PSI), S. Braccini (AEC-LHEP, UniBe), N. P. van der Meulen (PSI), R. Eichler (PSI & UniBe), Z. Talip (PSI)

## Introduction

The future of Targeted Radionuclide Therapy (TRT) will lie in tailored medicine. However, several challenges and unknowns persist towards optimum cancer treatments. Specifically, Auger-electron emitters have recently stood out as efficient tools to eradicate micrometric or single-cell tumors. This objective is achieved thanks to the high linear energy transfer (LET) of these particles, thereby travelling short distances in human tissues (Kassis, 2011). Access to Auger-electron emitters in both adequate quality and quantity would enable systematic preclinical studies.

$^{161}\text{Ho}$  ( $t_{1/2} = 2.48$  (5)  $h$ , EC = 100 %) emerges as a viable candidate as Auger-electron emitter thanks to its relatively large emittance of low-energy electrons:  $3.51 e^-/\text{decay}$ ,  $E_e^- < 20 \text{ keV}$  (Filosofov et al., 2021). In addition, it emits low-intensity, low-energy gamma rays ( $E_\gamma = 103.05$  (2)  $\text{keV}$ ,  $I_\gamma = 3.9$  (6) %), reducing the risk of additional dose deposition in patients, while enabling follow-up imaging of therapy.

In the framework of radionuclide production, the decision of the optimum production route relies on several factors, such as production cross-section data. A comprehensive characterization of the end-of-beam (EoB) radionuclidic composition is crucial for assessing the production yields and minimizing undesired impurities. This will impact the dose administered to the patient and, consequently, the therapeutic outcome.

To date, different studies have been reported regarding the use of several projectiles to investigate the production cross sections of  $^{161}\text{Ho}$ . In particular,  $^{nat}\text{Dy}_2\text{O}_3$  was used as target material, covering the energy range of (5-77) MeV (Červenák & Lebeda, 2022).

The present work investigated the proton-induced production cross sections of holmium radioisotopes using  $^{nat}\text{Dy}_2\text{O}_3$  target material. We employed an 18-MeV cyclotron installed at the Bern medical cyclotron laboratory in collaboration with the Laboratory of High-Energy Physics (LHEP).

## Materials and Methods

The Bern facility comprises two bunkers. One hosts an IBA Cyclone 18/18 HC cyclotron, connected to the neighboring bunker through a 6-m-long Beam Transport Line (BTL) (Braccini, 2013). This structure efficiently transports a proton beam of  $(18.3 \pm 0.4)$  MeV in energy, whose current ranges from a few pA to 150  $\mu\text{A}$ . Several tools installed along the BTL ensure a good quality of the proton beam, including the UniBEaM, a non-destructive two-dimensional beam profiler.

The target material was purchased from ChemPUR (DE) with a chemical purity of 99.99 %. Each target was irradiated for few minutes (<10 min) with a flat proton beam of 10 nA in current. The irradiated targets consist of aluminum disks with a central pocket. Here, about 2 mg of target material was deposited by pipetting 5  $\mu\text{L}$  of  $\text{Dy}_2\text{O}_3$  suspended in ethanol. The deposition was repeated until the whole pocket surface was completely covered. Each target disk was covered with an aluminum foil (13  $\mu\text{m}$  in thickness) prior to irradiation. This precaution prevents any loss of target material while handling the disk post-irradiation. Stacked thin aluminum disks (125, 200, and 300  $\mu\text{m}$  in thickness) degraded the proton beam energy to scan the available energy range ( $\leq 18.3 \text{ MeV}$ ).

The produced activity of each radionuclide was ascertained using gamma-ray spectrometry immediately following irradiation. A n-type high purity germanium (HPGe) detector (Canberra 2019) is coupled to an electronic acquisition chain and to a Lynx<sup>®</sup> digital signal analyzer. A Microsoft Excel interface was used to control the Genie-2000 Spectroscopic Software of Canberra Industries. The analysis of each spectrum was conducted using the InterSpec analysis software. Due to the complexity of the spectra and the substantial number of radionuclides produced (see Table 1), each target was measured multiple times for several hours. This approach facilitated the

**Table 1:** Decay data of each radionuclide produced via irradiation of  $^{nat}\text{Dy}_2\text{O}_3$  target (from (IAEA, 2024)).

Nuclide	Decay mode	Half-life	$E_\gamma$ (keV)	$I_\gamma$ (%)
$^{157}\text{Dy}$	$\epsilon + \beta^+$ : 100 %	8.14 (4) h	326.34	93 (3)
$^{156}\text{Ho}$	$\epsilon + \beta^+$ : 100 %	56 (1) min	137.80	52 (5)
$^{159}\text{Ho}$	$\epsilon + \beta^+$ : 100 %	33.1 (1) min	121.01	36.2 (11)
$^{160g}\text{Ho}$	$\epsilon + \beta^+$ : 100 %	25.6 (3) min	728.17	33.2 (9)
$^{160m}\text{Ho}$	$\epsilon + \beta^+$ : 23.8 (20) % IT: 76.2 (20) %	5.02 (5) h	728.17	33.2 (9)
$^{161}\text{Ho}$	$\epsilon$ : 100 %	2.48 (5) h	103.05	3.9 (6)
$^{162g}\text{Ho}$	$\epsilon + \beta^+$ : 100 %	15 (1) min	80.70	8.0 (6)
$^{162m}\text{Ho}$	$\epsilon + \beta^+$ : 38 % IT: 62 %	67.0 (7) min	184.99	23.94 (7)

differentiation of radionuclides based on their respective half-lives. Moreover, it allowed us to calculate the cross-section values for nuclides produced (a) through proton irradiation and (b) originated from the decay of a parent radionuclide. A notable example is the case of  $^{160g}\text{Ho}$  ( $t_{1/2} = 25.6$  (3) h) and  $^{160m}\text{Ho}$  ( $t_{1/2} = 2.48$  (5) h). The latter constitutes the sole problematic long-lived radionuclidic impurity. Additionally, one of its daughter nuclides,  $^{160g}\text{Ho}$ , shares identical gamma rays, as documented in the Nuclear Data Sheets.

## Results and Discussion

The production cross sections of  $^{156}\text{g}, ^{159}\text{g}, ^{160g}, ^{160m}, ^{161}\text{g}, ^{162g}, ^{162m}\text{Ho}$  and  $^{157}\text{Dy}$  were successfully measured from 7.0 MeV to 18.2 MeV. The experimental results of  $^{161}\text{Ho}$  and  $^{160m}\text{Ho}$  are shown in Figure 1 in comparison with numerical values of previous works. Theoretical calculations were obtained from TENDL 2023 library, evaluated using the TALYS code.

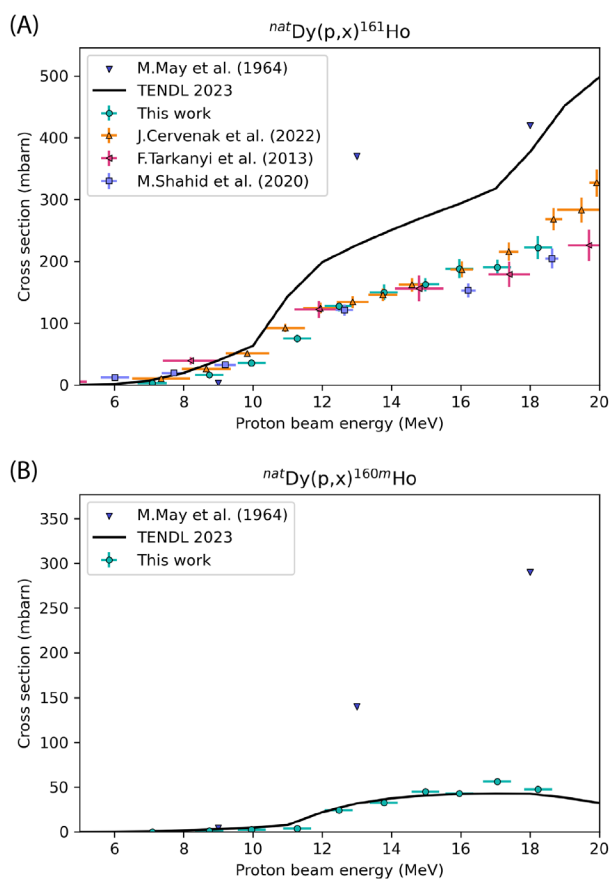


**Figure 1:** Comparison of experimental and theoretical production cross sections of (A)  $^{161}\text{Ho}$  and (B)  $^{160m}\text{Ho}$  in proton-irradiated  $^{nat}\text{Dy}_2\text{O}_3$ .

In Figure 1A, our results show good agreement with the available experimental data. TENDL 2023 evaluations considerably overestimate the experimental data. In the investigated energy range, two nuclear reactions contribute to the  $^{161}\text{Ho}$  production: (a)  $^{161}\text{Dy}(p,n)$  and (b)  $^{162}\text{Dy}(p,2)$  reactions. Figure 1B demonstrates a

notable agreement between our findings and theoretical evaluations for the  $^{160m}\text{Ho}$  production cross sections. However, the results of May et al. show a large discrepancy compared to our results. This deviation could potentially be attributed to the imprecision of the nuclear data used. Moreover, it is noteworthy that May et al. did not report the implementation of any correction accounting for the decay chain of  $^{160g}\text{Ho}$  and  $^{160m}\text{Ho}$ . This oversight could lead to an overestimation of the production cross section justified by the measurement of the total activity of both radionuclides. The  $^{160}\text{Dy}(p,n)$  and  $^{161}\text{Dy}(p,2n)$  reactions predominantly contribute to the  $^{160m}\text{Ho}$  production in the investigated energy range.

## Outlook

The following phase will involve the investigation of production cross section measurements using enriched  $^{161}\text{Dy}_2\text{O}_3$  (91.1 % enriched) and  $^{162}\text{Dy}_2\text{O}_3$  (94.5 % enriched) target materials, respectively. This step will also enable the calculation of nuclear cross sections of the relevant nuclear reactions.

## Acknowledgement

This research was supported by the European Union's Horizon 2020 research and innovation programme under grant agreement No. 101008571 (PRISMAP - The European medical radionuclides programme).

## References

- [1] S. Braccini, *AIP Conference Proceedings*, **1525**, 144-150 (2013)
- [2] J. Červenák, & O. Lebeda, *Nuclear Instruments and Methods in Physics Research, Section B: Beam Interactions with Materials and Atoms*, **522**, 1-13 (2022)
- [3] D. Filosofov, et al., *Nuclear Medicine and Biology*, **94-95**, 1-19 (2021)
- [4] IAEA Live Chart of Nuclides, <https://www-nds.iaea.org/relnsd/vcharthtml/VChartHTML.html> (accessed in 01/2024)
- [5] A. I. Kassis et al., *Radiation Protection Dosimetry*, **143**(2-4), 241-247 (2011)
- [6] E. Renaldin et al., *LRC Annual Report 2023*, 52-53 (2024)

# Cyclotron production of a medically relevant radionuclide $^{161}\text{Ho}$

E. Renaldin (UniBe & PSI), A. Sommerhalder (PSI), H. Zhang (PSI), N. P. van der Meulen (PSI), R. Eichler (PSI & UniBe), Z. Talip (PSI)

## Introduction

The production of a novel medical radionuclide requires a multidisciplinary approach. To succeed in this objective, each step must be optimized considering the impact of both preceding and following stages. Investigation of  $^{161}\text{Ho}$  production as a potential radionuclide for Targeted Radionuclide Therapy (TRT) consists of two subprojects: (1) cross-section measurements of relevant holmium radioisotopes using a medical cyclotron, and (2) investigation of different  $^{161}\text{Ho}$  production routes using medium energy proton accelerator.

The results of the first project are reported in (Renaldin et al., 2024). The second study focused on the assessment of the production yields and radionuclidic purity of the end-of-bombardment (EoB) product using different target materials.

## Materials and Methods

The  $^{161}\text{Ho}$  production was performed at the Paul Scherrer Institute (PSI) using a 72-MeV proton beam ( $I_p \leq 50 \mu\text{A}$ ) accelerated by the Injector II cyclotron. Four different target materials are planned to be utilized to study  $^{161}\text{Ho}$  production feasibility, namely: (1)  $^{nat}\text{Dy}_2\text{O}_3$ , (2)  $^{161}\text{Dy}_2\text{O}_3$ , (3)  $^{162}\text{Dy}_2\text{O}_3$ , and (3)  $^{nat}\text{Ho}_2\text{O}_3$ , thereby exploiting four nuclear reactions (Figure 1). During the last six months of Injector II operation, the investigation of  $^{161}\text{Ho}$  production was conducted only for  $^{nat}\text{Dy}_2\text{O}_3$  (99.99 %, ChemPUR, DE) and  $^{162}\text{Dy}_2\text{O}_3$  (enr. 94.5 %, ISOFLEX USA) target materials. Different proton energies were chosen to irradiate two targets for each test run. The proton energies were selected according to experimental and theoretical cross section data with

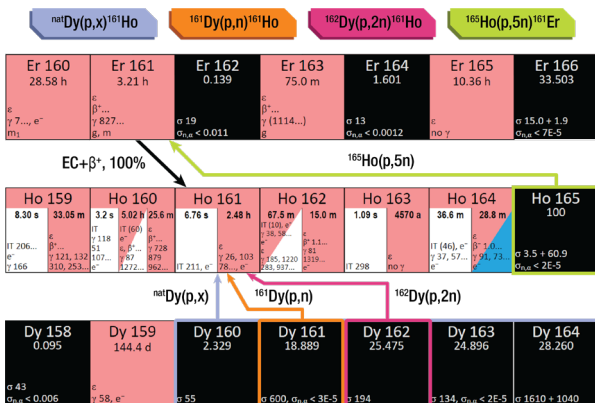
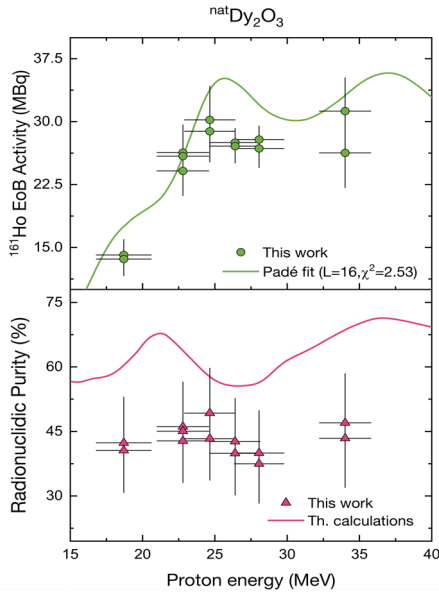


Figure 1: Karlsruhe nuclide chart showing different  $^{161}\text{Ho}$  production routes.

the focus on maximizing the  $^{161}\text{Ho}$  production yield. Niobium foils located before the target degrade the proton beam energy to the optimal value. Each target consists of a 40-mg disk, 6 mm in diameter made of lanthanide oxide powder pressed with a hydraulic press (thickness  $\approx 270 \mu\text{m}$ ). The disks are then encapsulated in aluminum. Initially, low proton currents ( $\approx 5 \mu\text{A}$ ) and short irradiation times ( $\approx 5 \text{ min}$ ) were employed to limit the activity produced. Afterward, both irradiation parameters were increased. This approach enabled the assessment of the EoB activity of short-lived radionuclides ( $30 \text{ min} < t_{1/2} < 1 \text{ h}$ ). Multiple gamma spectra following EoB were acquired using a n-type coaxial high-purity germanium (HPGe) (Inter technique Nucléaire, France) detector coupled to an electronic acquisition chain. Spectrometric analysis was performed utilizing InterWinner software.

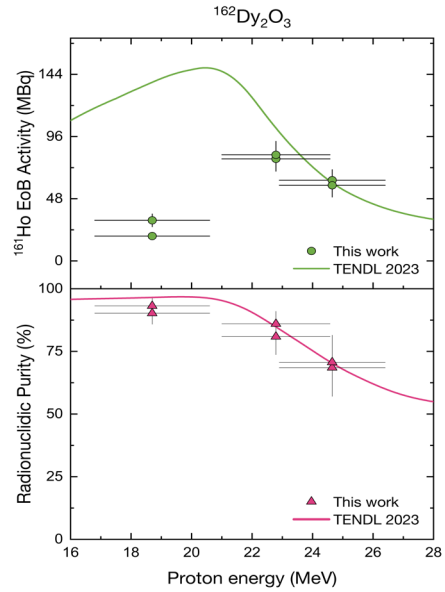
## Results and Discussion

Figure 3 and Figure 2 illustrate the EoB activities of  $^{161}\text{Ho}$  and the associated radionuclidic purities, considering a 5-hour cooling time, for  $^{nat}\text{Dy}_2\text{O}_3$  and  $^{162}\text{Dy}_2\text{O}_3$ , respectively. Predictions of EoB activities of  $^{161}\text{Ho}$  are also reported. EoB activities and radionuclidic purities were evaluated using Padé approximants fitted on the experimental cross-section data available in the literature for  $^{nat}\text{Dy}_2\text{O}_3$ . Therefore, analytic functions were obtained only for the excitation functions of  $^{159,161,162m}\text{Ho}$ . When such data were unavailable, theoretical cross sections obtained from TENDL 2023 were adopted for the calculations. As illustrated by Figure 3, the predictions for  $^{nat}\text{Dy}_2\text{O}_3$  targets slightly deviate from experimental data. Such discrepancy could be attributed to the fact that the thick target yields (TTY, MBq/ $\mu\text{A}$ ) were evaluated using an average target disk with the following characteristics: density of  $(5.1 \pm 0.4) \text{ g/cm}^3$ , thickness of 0.27 mm, and mass of 40 mg. Moreover, for the determination of EoB activities, simulated proton currents multiply the TTYs. Unfortunately, no diagnostic tool is installed in the IP2 irradiation target station to control the proton current. The values adopted were simulated using Beam Delivery Simulation (BDSIM), a Geant4-based software. On the other hand, Figure 3 shows a good agreement between our findings and the predictions for the  $^{162}\text{Dy}_2\text{O}_3$  targets based exclusively on TENDL 2023 theoretical cross sections. The large deviation of the point at 18.7 MeV



**Figure 2:** (Top) Comparison of our experimental data and calculations based on Padé approximant fitted using experimental and theoretical cross-section data of  $^{nat}\text{Dy}_2\text{O}_3$ . (Bottom) Radionuclidic purity results evaluated after a 5-hour cooling time. Irradiation conditions:  $I_p = 5 \mu\text{A}$ ,  $t_{irr} = 5 \text{ min}$ ,  $m_{tar} = 40 \text{ mg}$ .

might be attributed to (a) a possible loss of target material when opening the target capsule, and/or (b) to inaccurate proton currents. It is worth mentioning that no experimental data using  $^{162}\text{Dy}_2\text{O}_3$  as target material are present in the literature, to our knowledge. Considering the isotopic composition of the targets, proton irradiation of  $^{nat}\text{Dy}_2\text{O}_3$  leads to low purity levels. The most relevant holmium radionuclidic impurities are  $^{160m}\text{Ho}$  ( $t_{1/2} = 5.02$  (5)  $h$ ) and  $^{162m}\text{Ho}$  ( $t_{1/2} = 67.0$  (7)  $min$ ). The presence of  $^{162m}\text{Ho}$  imposes a constraint on the cooling time to be around 5 hours to maximize the radionuclidic purity. On the other hand,  $^{160m}\text{Ho}$  is critical because of its inevitable presence as long-lived impurity. The presence of  $^{160m}\text{Ho}$  and  $^{162m}\text{Ho}$  also indirectly contribute to decrease the purity through the production of daughter holmium nuclides, namely:  $^{160g}\text{Ho}$  ( $I_{IT} = 76.2\%$ ) and  $^{162g}\text{Ho}$  ( $I_{IT} = 62\%$ ,  $t_{1/2} = 15$  (1)  $min$ ). Using an enriched target material ensures the reduction of undesired impurities, as shown in Figure 3. In this case, the  $^{162m}\text{Ho}$  production is hindered due to the suppression of the  $^{161}\text{Dy}(p,\gamma)$ ,  $^{163}\text{Dy}(p,2n)$ , and  $^{164}\text{Dy}(p,3n)$  reactions. Conversely, the low isotopic abundance of  $^{161}\text{Dy}$  significantly limits the production of  $^{160m}\text{Ho}$  through the  $(p,2n)$  reaction. Besides the test irradiation experiments, a 40-mg  $^{162}\text{Dy}_2\text{O}_3$  disk was irradiated for 1 hour with a 50- $\mu\text{A}$  proton current. The EoB  $^{161}\text{Ho}$  activity was measured as 1.1 GBq with a radionuclidic purity of 83 % after 5-hour cooling time.



**Figure 3:** (Top) Comparison of our experimental data and calculations based on TENDL 2023 theoretical cross-section data of  $^{162}\text{Dy}_2\text{O}_3$ . (Bottom) Radionuclidic purity results evaluated after a 5-hour cooling time. Irradiation conditions:  $I_p = 5 \mu\text{A}$ ,  $t_{irr} = 5 \text{ min}$ ,  $m_{tar} = 40 \text{ mg}$ .

## Outlook

The irradiations of the remaining target materials ( $^{161}\text{Dy}_2\text{O}_3$ ,  $^{nat}\text{Ho}_2\text{O}_3$ ) are planned soon after the maintenance period. Using  $^{nat}\text{Ho}_2\text{O}_3$  as target material could significantly improve the final product features. Specifically, radionuclidic purity should improve thanks to significantly lower production of  $^{160m}\text{Ho}$  and  $^{162m}\text{Ho}$ . After an efficient radiochemical separation, this production route will enable the use of this Auger-electron emitter in systematic preclinical studies.

## Acknowledgement

This research was supported by the European Union's Horizon 2020 research and innovation programme under grant agreement No. 101008571 (PRISMAP - The European medical radionuclides programme).

## References

- [1] E. Renaldin et al., *LRC Annual Report 2023*, 50-51 (2024)
- [2] F. Tárkányi et al., *Applied Radiation and Isotopes*, **115**, 262–266 (2016)

# Production of high specific activity $^{166}\text{Ho}$ for targeted radionuclide therapy

E. Renaldin (UniBe & PSI), U. Köster (ILL), A. Vögele (PSI), N. P. van der Meulen (PSI), R. Eichler (PSI & UniBe), Z. Talip (PSI)

## Introduction

The Targeted Radionuclide Therapy (TRT) technique has succeeded in treating various types of small metastases thanks to the recent advancements in targeting agent design and novel radionuclide production. Notably, among the established radionuclides widely adopted in clinics,  $^{166}\text{Ho}$  ( $t_{1/2} = 26.807$  (12) h,  $\beta^- = 100\%$ ,  $E_{\beta^-av} = 665$  keV) is employed for treating several cancers [1]. Moreover, this radiolanthanide emits low-energy gamma quanta of moderate intensity:  $E_{\gamma} = 80.6$  keV,  $I_{abs} = 6.56$  (13) %, thereby enabling SPECT imaging during therapy but not adding excessive photon dose to the patient.

Our research involves developing an efficient production method to provide  $^{166}\text{Ho}$  in high specific activity, notably in non-carrier added (n.c.a.) form. Furthermore, producing the  $^{166}\text{Dy}$  precursor would enable the development of a generator system and the possibility of producing radionuclidically pure  $^{166}\text{Ho}$ .

## Materials and Methods

As illustrated by Figure 1 two subsequent neutron captures are employed to produce  $^{166}\text{Dy}$  using natural  $\text{Dy}_2\text{O}_3$  (99.99% purity, ChemPUR, DE) or enriched  $^{164}\text{Dy}_2\text{O}_3$  (enrichments: 94.36% and 96.80%, ISOVELX USA) as target material. In addition, stable cobalt was added to the ampoules as neutron fluence monitor. Two empty ampoules were also irradiated to determine the activated impurities in the quartz. The ampoules were irradiated for 6 to 7 days at the high-flux reactor of the Institut Laue-Langevin (ILL), Grenoble (FR) ( $\Phi_{th} \leq 1.2 \cdot 10^{15} \text{cm}^{-2}\text{s}^{-1}$ ), or for up to 3 weeks at the PSI SINQ facility ( $\Phi_{th} \leq 2.8 \cdot 10^{13} \text{cm}^{-2}\text{s}^{-1}$ ).

Each ampoule was measured multiple times using gamma-ray spectrometry throughout several months following the end of irradiation (Eol). A n-type high-purity germanium (HPGe) (Inter technique Nucléaire, France) detector was used together with InterWinner, a gamma spectroscopy analysis program.

## Results and Discussion

The table below reports the relevant irradiation parameters, the investigated target materials, the target masses, and the end of irradiation (Eol) activities

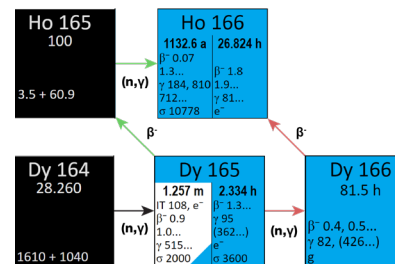


**Figure 1:** Karlsruhe nuclide chart showing the relevant radionuclides with the associated nuclear reactions and decay modes.

per unit of metal mass (Dy) compared to predictions based on tabulated thermal neutron capture cross sections ( $^{164}\text{Dy}(n, \gamma)^{165}\text{Dy}$ ,  $\sigma = 2650$  (25) barn,  $^{165}\text{Dy}(n, \gamma)^{166}\text{Dy}$ ,  $\sigma = 3600$ (300) barn, [2]).  $^{166m}\text{Ho}$  activities are also reported. The predictions of  $^{166}\text{Dy}$  production slightly underestimate the experimental outcomes on average. It is worth mentioning that they were evaluated based on experimental neutron fluxes.

To determine the activated impurities in the target material, gamma spectra of the irradiated empty ampoule and Ampoule (2) were compared (Figure 2). The spectrum of Ampoule (2) was acquired after the complete decay of  $^{166}\text{Dy}$ . Figure 2 shows that the radionuclides ( $^{46}\text{Sc}$  ( $t_{1/2} = 83.8$  d),  $^{141}\text{Ce}$  ( $t_{1/2} = 32.5$  d),  $^{152}\text{Eu}$  ( $t_{1/2} = 13.5$  y),  $^{154}\text{Eu}$  ( $t_{1/2} = 8.6$  y),  $^{155}\text{Eu}$  ( $t_{1/2} = 4.75$  y),  $^{156}\text{Eu}$  ( $t_{1/2} = 15.2$  d),  $^{160}\text{Tb}$  ( $t_{1/2} = 72.3$  d),  $^{169}\text{Yb}$ -169 ( $t_{1/2} = 32$  d) are mainly due to the impurities present in the irradiated quartz ampoule.

$^{166m}\text{Ho}$  ( $t_{1/2} = 1132.6$  (39) y), a potential long-lived radionuclidic impurity, were also determined. Since  $^{166}\text{Dy}$  does not decay to  $^{166m}\text{Ho}$ , the latter can only originate from the  $^{165}\text{Ho}(n, \gamma)^{166m}\text{Ho}$  reaction ( $\sigma_{th} = 3.5$  barn). Here, two sources of stable  $^{165}\text{Ho}$  could produce this isomer: (i) chemical Ho impurity in the target material & (ii) decay product of  $^{165}\text{Dy}$  ( $t_{1/2} = 2.334$ (1) h).

Based on the acquired data, a timeline is envisioned considering a constraint on  $^{166}\text{Ho}$  activity at the time of shipment from ILL reactor of 100 GBq due to radioprotection reasons (Figure 3). It shows calculated activities of both  $^{166}\text{Dy}$  and  $^{166}\text{Ho}$  after the irradiation of 650  $\mu\text{g}$  of  $^{164}\text{Dy}_2\text{O}_3$  (96.8%) at ILL for 6 days using the high flux ( $1.2 \cdot 10^{15} \text{cm}^{-2}\text{s}^{-1}$ ). The sudden drops of  $^{166}\text{Ho}$  activity determine the end of each separation under the assumption of 100% separation yield.

	Experimental neutron flux (cm <sup>-2</sup> s <sup>-1</sup> )	Irradiation time (d)	Target material (enrich.)	Dy <sub>2</sub> O <sub>3</sub> mass (μg)	<sup>166</sup> Dy EoB activity (GBq/mg)	Expected <sup>166</sup> Dy EoI activity (GBq/mg)	<sup>166m</sup> Ho (Bq)
(1)	3.12E+14	6.6	<sup>nat</sup> Dy <sub>2</sub> O <sub>3</sub> (28.26%)	7.0	4.2 ± 0.2	6.5	0
(2)	6.65E+14	6.0	<sup>164</sup> Dy <sub>2</sub> O <sub>3</sub> (94.36%)	6.3	65 ± 3	73	91
(3)	3.49E+14	6.6	<sup>164</sup> Dy <sub>2</sub> O <sub>3</sub> (96.8%)	8.3	8.8 ± 1.5	29	45
(4)	1.12E+15	6.8	<sup>164</sup> Dy <sub>2</sub> O <sub>3</sub> (96.8%)	8.3	119 ± 6	144	217
(5)	2.01E+13	3.8	<sup>164</sup> Dy <sub>2</sub> O <sub>3</sub> (96.8%)	8.3	0.072 ± 0.004	0.089	0
(6)	2.36E+13	20.9	<sup>164</sup> Dy <sub>2</sub> O <sub>3</sub> (96.8%)	1300	0.104 ± 0.006	0.21	425
(7)	2.24E+13	20.9	<sup>164</sup> Dy <sub>2</sub> O <sub>3</sub> (96.8%)	1100	0.131 ± 0.007	0.19	465

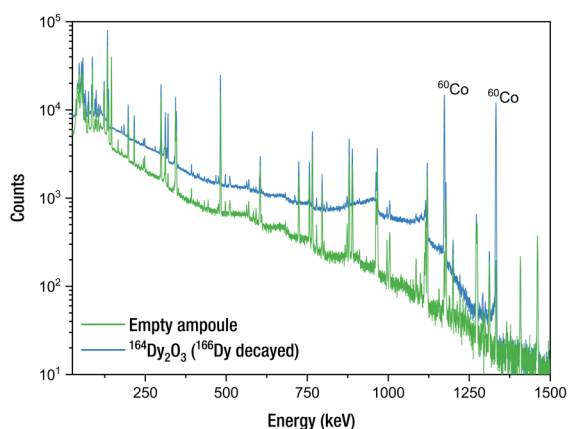


**Figure 2:** Comparison between the gamma spectra of Ampoule (2) after the complete decay of <sup>166</sup>Dy and the empty one.

Specifically, it is found that the total collected activity of <sup>166</sup>Ho is maximized adopting a cooling time of 20 hours after each separation. This can be achieved by loading the Dy fractions from the previous separation onto another column to retrieve the ingrowing <sup>166</sup>Ho through ideally faster subsequent separations.

### Conclusion and Outlooks

Two milligrams of <sup>164</sup>Dy<sub>2</sub>O<sub>3</sub> (enr. 96.8%) are potentially capable of producing large <sup>166</sup>Dy activities (EoI 260 GBq) exploiting the high neutron flux available at the ILL research reactor, enabling the promising generator system. Further ICP-MS measurements are planned to determine the <sup>165</sup>Ho quantities in the irradiated targets.

The promising experimental results obtained for the <sup>166</sup>Dy production at ILL reactor provide the basis for planning the development of chemical separation between Dy and Ho. Several resins will be tested to chemically isolate holmium in view of a generator system. Moreover, achieving radionuclidically pure <sup>166</sup>Ho as final product in high specific activities might streamline the introduction of this radionuclide into clinics for TRT.

### Acknowledgements

This research was supported by the European Union's Horizon 2020 research and innovation programme

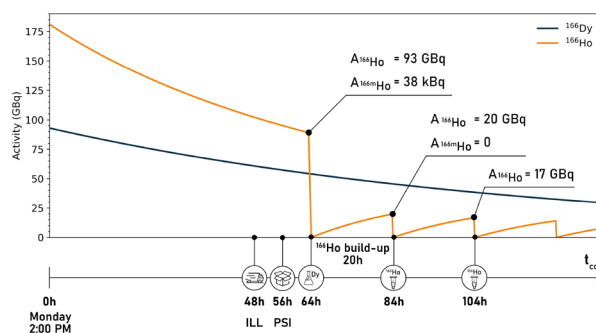


**Figure 3:** Qualitative trends of <sup>166</sup>Ho and <sup>166</sup>Dy following end of irradiation (EoI) considering a target mass of 650 μg <sup>164</sup>Dy<sub>2</sub>O<sub>3</sub>, irradiation time = 6 days, Φ = 1.2E+15 cm<sup>-2</sup>s<sup>-1</sup>. This plot displays a plausible production under the simplifying assumption of 100% separation yield at each step.

under grant agreement No. 101008571 (PRISMAP - The European medical radionuclides programme).

### References

- [1] N. J. M. Klaassen et al., *EJNMMI Radiopharm. Chem.*, **4**, 1-26, 2019
- [2] T. Sekine and H. Baba, *J. Inorg. Nucl. Chem.*, **43**, 1107–1113 (1981)

# Production of Terbium-155 via Dysprosium-155 by irradiation of $^{nat}\text{Tb}$ by medium energy protons

A. N. Moiseeva (PSI), C. Favaretto (PSI), Z. Talip (PSI), P.V. Grundler (PSI), C. C. Hillhouse (PSI), R. Eichler (PSI & UniBe), R. Schibli (ETHZ & PSI), N. P. van der Meulen (PSI)

## Introduction

Radionuclides must fulfill several criteria to be applied for theragnostics: i) complementary types of low and high LET radiation; ii) suitable half-life of the radioisotopes; iii) stability in bio/physiological reactions; and iv) absence of undesirable decay products. A quadruplet of terbium (Tb) radioisotopes meets all of them, presenting the perfect case towards bringing theragnostics into practice.

To date, only  $^{161}\text{Tb}$  has an established production protocol [1]. The other terbium radioisotopes have significant challenges related to production and purification, requiring either ultra-enriched target material (for example, requiring >99 %  $^{152}\text{Gd}$ ) or limited middle- and high-energy particle accelerators with subsequent separation difficulties or extremely scarce Isotope Separation On-Line (ISOL) facilities.

Earlier, an indirect method of  $^{155}\text{Tb}$  production with high radionuclidic purity was proposed [2]. The  $\alpha$ -particle beam is required for this method, however, it was proposed that  $^{155}\text{Tb}$  can be obtained by proton irradiation of naturally occurring  $^{159}\text{Tb}$  [3]: it is achievable and feasible [4]. In this light,  $^{155}\text{Tb}$  can be a most promising radioisotope for nuclear medicine in the next decade. In this study, we focused on the separation method of  $^{155}\text{Dy}$  from the terbium target.

## Materials and methods

15 mL of cation exchange Sykam resin with a grain size of 12-22  $\mu\text{m}$  (Sykam) was transferred into an 18-cm high and 10-mm i.d. column. The same column was used in all experiments. The column was saturated with 1.0 M  $\text{NH}_4\text{NO}_3$  and rinsed with water. Aliquots of terbium-dysprosium solution (1-30 mL) was loaded onto the column from 0.5 M HCl, 0.5 M, 7.0 M, 10 M, and 69%  $\text{HNO}_3$  solution, respectively. The column was rinsed with water and saturated with 1.0 M  $\text{NH}_4\text{NO}_3$  again in the case of loading from high-concentrated nitric acid solutions. The separation was performed with 0.11 M or 0.12 M  $\alpha$ -hydroxyisobutyric acid ( $\alpha$ -HIBA) with different flow rates. 2.5-10 mL fractions were collected and the content of Tb and ICP-OES measurements monitored the content of Tb and Dy.

Several experiments with different masses of terbium – from 5  $\mu\text{g}$  to 40 mg – were carried out to determine the mass effect on the elution profiles and to simulate the irradiated terbium target.

## Results

The optimal conditions of terbium oxide ( $^{nat}\text{Tb}_4\text{O}_7$ ) dissolution were in 1 mL 10 M  $\text{HNO}_3$ . The targets were dissolved for 24 min.

Loading the column with 10M  $\text{HNO}_3$  does not affect the separation process, but re-saturation of the column after the loading is required in this case.

With 5  $\mu\text{g}$  of terbium, the optimal separation conditions were found and presented in Fig. 1.

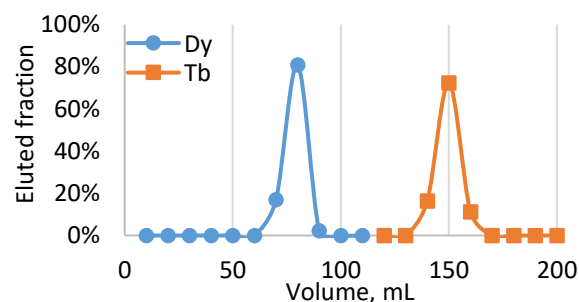


**Figure 1:** Reproducible elution profiles of Dy and Tb (both 5  $\mu\text{g}$ ) on Sykam Resin column with 0.11 M  $\alpha$ -HIBA as eluent.

According to the result with micro-amounts of terbium, experiments with a 40 mg target were conducted with elution of 0.11M  $\alpha$ -HIBA.

However, small amounts of terbium were eluted with the Dy fraction with the same conditions (Fig. 2).

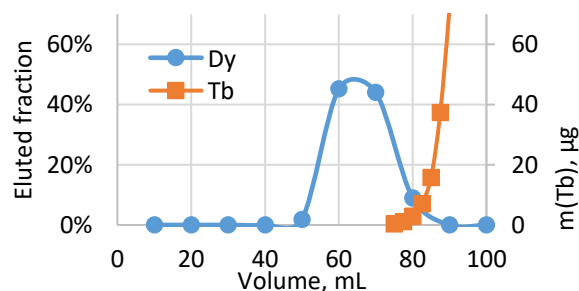


**Figure 2:** Reproducible elution profiles of 5  $\mu\text{g}$  Dy and 40 mg Tb on Sykam Resin column with pump rate 0.7 mL/min and eluent  $\alpha$ -HIBA 0.11 M.

To prevent contamination of dysprosium fraction with terbium, the flow rate of the eluent was decreased from 0.7 mL/min to 0.6 mL/min. The result is presented in the fig. 3.

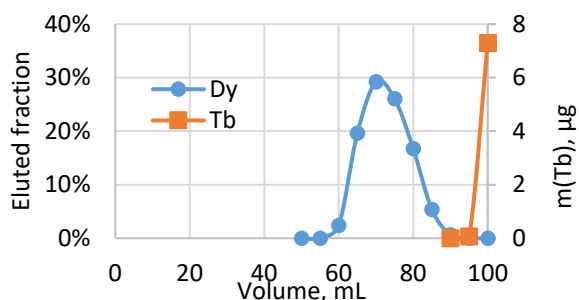


**Figure 3:** Reproducible elution profiles of 5 µg Dy and 40 mg Tb on Sykam Resin column with pump rate 0.6 mL/min and 0.11 M  $\alpha$ -HIBA as eluent.

The decrease of pump speed ensured the full separation of micro-amounts of dysprosium from the 40-mg terbium target. The time required for the separation step is 2.5 h.

### Conclusions and outlook

The proposed separation method can be used as the first stage of indirect  $^{155}\text{Tb}$  production. The method will be based on the separation of  $^{155}\text{Dy}$  from a terbium target irradiated with protons, using cation exchange chromatographic methods using Sykam resin. The amount of  $^{155}\text{Tb}$  produced will also depend on the time required for dysprosium fraction separation from terbium target material. So far, it is possible to separate dysprosium within 4 h after the simulated end of irradiation. As a result, 2 Gb of  $^{155}\text{Tb}$  with radionuclidic purity > 99.9 % can be obtained after 12 h irradiation of 40 mg  $^{\text{nat}}\text{Tb}_4\text{O}_7$  target with 51 MeV protons.

It is important to research the second stage of separation, when ingrown  $^{155}\text{Tb}$  should be isolated from dysprosium fraction after 40 h. This stage should notably increase the chemical purity of  $^{155}\text{Tb}$  due to separation of the possible presence of not only decaying  $^{155}\text{Dy}$  but also long-lived or stable  $^{154,156}\text{Dy}$  as part of the dysprosium fraction.

### References

- [1] N. Gracheva et al., *EJNMMI Radiopharm. Chem.*, **4**, 12 (2019)
- [2] A. N. Moiseeva et al., *Nucl. Med. Biol.*, **126–127**, 108389 (2023)
- [3] Steyn et al., *Nucl. Instr. Meth. Phys. B*, **319**, 128 (2014)
- [4] C. Favaretto, Doctoral Thesis, ETH Zurich (2023)

## Developing direct $^{68}\text{Ga}$ production for medical cyclotrons

P. V. Grundler (PSI), S. Braccini (LHEP, UniBe), N. P. van der Meulen (PSI)

### Introduction

$^{68}\text{Ga}$  is a positron emitter with a half-life of 68 minutes and, thus, suitable for medical imaging by positron emission tomography (PET). The use of generator with  $^{68}\text{Ge}$  ( $T_{1/2} = 271$  days) as mother nuclide is widespread, however, since there is at times a struggle of generator supply to meet the demand, the development of  $^{68}\text{Ga}$  production with medical cyclotrons is actively pursued, using liquid [1] or solid targets [2]. The cross section for the  $^{68}\text{Zn}(p,n)^{68}\text{Ga}$  at 12 MeV is high enough (800 mb) [2] to easily provide GBq activities of  $^{68}\text{Ga}$  in one irradiation.  $^{68}\text{Zn}$ , with a natural abundance of 18.45%, is readily available as isotopically enriched target material, a prerequisite for high radionuclidic purity. To achieve high radiochemical purity, an efficient and fast chemical separation procedure is required to remove the large excess of  $^{68}\text{Zn}$  target material and other potential inactive metallic contaminants that may compete with  $^{68}\text{Ga}$  for the chelating sites during the radiolabelling procedure.

### Experimental

Recycled  $^{68}\text{Zn}$ , from investigations for the production of  $^{67}\text{Cu}$  [3], was used as target material. The development of the purification method was already reported previously [4]. The  $^{68}\text{Zn}$  was used as solid target, therefore, the material needed to be shaped into a 6 mm disc. Dendritic  $^{68}\text{Zn}$ , obtained by electrowinning from an alkaline ammonium chloride solution, was used to press target discs of about 40 mg.

The targets were encapsulated in aluminium with a 1-mm Al cover plate (Fig. 1).

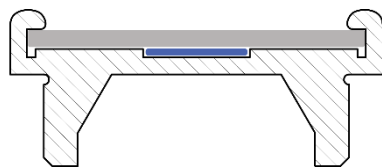


**Figure 1:** Cross cut through aluminium capsule containing the disc of target material at the centre. Proton beam enters the capsule from the top in this view.

Irradiations were performed at PSI's IP2 target station with a 72 MeV proton beam from the Injector 2 separated-sector cyclotron and degraded with 3.4 mm-thick niobium to 10.3 MeV. After retrieving the target from the capsule and determining its raw activity, it was

transferred to a vial in the chemical separation set-up in a hot cell.

The set-up, mounted on a panel, consists of a vial to dissolve the target in concentrated HCl, a peristaltic pump to load the dissolved target onto a macroporous polymeric resin which retains the  $^{68}\text{Ga}$  while Zn, the  $\text{Ti}^{3+}$  used to reduce the problematic  $\text{Fe}^{3+}$  are eluted with 7.0 M HCl and sent to the recycling bottle. The  $^{68}\text{Ga}$  is then eluted from the column with 1.0 M HCl and loaded onto a second column, containing extraction resin, using a second pump. The final  $^{68}\text{Ga}$  solution is then eluted from the second column with 0.1 M HCl in a volume of about 700  $\mu\text{L}$  which can be used for labelling.

Quality of the produced  $^{68}\text{Ga}$  was assessed by performing a test labelling of DOTATOC analysed by HPLC to evaluate the radiochemical purity.  $\gamma$ -spectrometry was used to determine the radionuclidic purity, whereas ICP-OES was performed on decayed samples to quantify the non-radioactive contaminants.

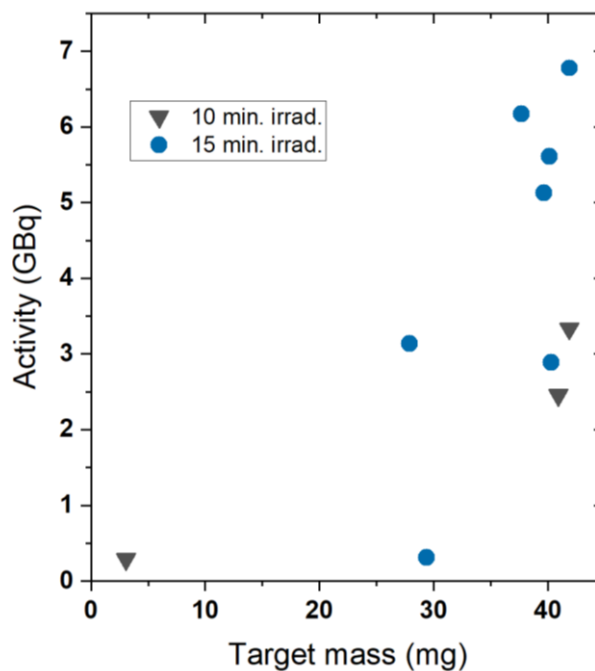


**Figure 2:** Activity of targets at EOB vs target mass ( $^{68}\text{Zn}$ ).

## Results

A total of 10 irradiations were performed with target masses between 3 and 42 mg. Fig. 2 shows the activity at EOB vs target mass. The scatter is due to the variable quality of the proton beam.

All targets were processed to isolate  $^{68}\text{Ga}$  from  $^{68}\text{Zn}$ . The separation process took between 47 and 80 minutes, depending on eluent volumes used for the different steps. Occasionally, issues in loading and connecting the reaction vial to the set-up increased the processing time (as was the case with 80 minutes). The recovered activities, listed in Table 1, demonstrated that the recovery is generally regarded as good, with more than 70% separation yield, but that the speed of the separation is crucial for a better final yield.

**Table 1:**  $^{68}\text{Ga}$  activities separated from the irradiated  $^{68}\text{Zn}$  targets for the 10 production runs.

Target mass (mg)	Activity EOS (GBq)	Yield	Separation yield, decay corrected
3.06	0.119	41.5%	81.4%
41.88	1.244	37.3%	78.5%
40.94	0.922	37.6%	71.4%
39.70	2.35	45.9%	74.1%
40.17	2.22	39.6%	68.6%
37.70	2.56	41.5%	80.5%
27.90	1.06	33.8%	63.6%
29.37	0.083	26.9%	47.1%
41.90	2.66	39.2%	70.2%
40.33	0.719	24.9%	57.4%

The radionuclidic purity of the  $^{68}\text{Ga}$  solution was >97%, with  $^{67}\text{Ga}$  <2% and  $^{66}\text{Ga}$  <1% at EOS. To assess the suitability of the  $^{68}\text{Ga}$  for preclinical application, tests to label it to DOTATOC were performed. The quality proved to be variable from no labelling up to 100% yield at 100 MBq/nmol. Runs yielding only small activities proved to be of lower quality. However, high activities were not always a guarantee for good quality. The variability is likely due to the incomplete removal of the target material and some environmental impurities. Chemical analyses with ICP-OES were performed to identify and quantify these contaminants (Table 2).

**Table 2:** Impurities quantified in samples from four production runs compared to the apparent molar activity at 50 MBq/nmol.

Impurity (ppb)	Individual production runs			
Al	667	823	848	684
Cu	4	22	88	8
Fe	78	96	91	101
Ga	<1	12	4	10
Pb	2	9	27	<1
Ti	32	72	419	422
Zn	2774	3392	2549	603
Total	3557	4426	4026	1828
AMA 50 MBq/nmol				
RCP (%)	53	99.7	46	98

As can be seen from Table 2, there is no clear correlation between the level of impurities and the results of the labelling. Either the problematic impurity evaded detection so far or the reagents for the labeling tests were of inconsistent quality. Further investigations are underway.

## Conclusions

The present work has demonstrated that  $^{68}\text{Ga}$  can be produced in quantity and quality as required for preclinical studies from solid  $^{68}\text{Zn}$  target at a cyclotron. However, the robustness of the separation method needs to be improved to provide a constant high quality. The irradiation should work well on a medical cyclotron, which will be tested in a near future at the machine situated at the Bern University Hospital (Inselspital).

## Acknowledgements

The authors thank Zhang Hui (PSI) for supervising the irradiations and Alex Sommerhalder (PSI) for providing support for the target handling before and after irradiation.

## References

- [1] M. E. Rodnick et al., *EJNMMI Radiopharmacy and Chemistry*, **5**(1), 25 (2020)
- [2] S. Braccini et al., *Appl. Radiat. Isot.*, 186, 110252 (2022)
- [3] R. Schwarzbach et al., *J. Labelled Compd. Radiopharm.*, **44**(S1), S809 (2001)
- [4] P. V. Grundler et al., *LRC Annual Report 2020*, 48 (2021)

# First-in-human administration of [<sup>161</sup>Tb]Tb-DOTA-LM3 in a patient with metastatic neuroendocrine tumour of the ileum

C. Favaretto (USB & PSI), J. Fricke (USB), F. Westerbergh (University of Gothenburg), L. McDougall (USB), P. V. Grundler (PSI), S. Geistlich (PSI), P. Bernhardt (University of Gothenburg), N. P. van der Meulen (PSI), R. Schibli (PSI & ETHZ), D. Wild (USB)

## Introduction

Similar to lutetium-177, terbium-161 undergoes decay with a half-life of 6.95 days, emitting medium-energy  $\beta^-$  particles ( $E_{\beta_{\text{average}}} = 154 \text{ keV}$ ) and  $\gamma$ -radiation suitable for imaging and dosimetry purposes ( $E_{\gamma} = 49 \text{ keV}$  [17%],  $75 \text{ keV}$  [10%]) [1]. In addition to lutetium-177, terbium-161 also releases conversion electrons and substantial amounts of Auger electrons (1213 %) with a high Linear Energy Transfer over a short distance ( $< 40 \text{ keV}/\mu\text{m}$ ). Preclinical evaluations showed high therapeutic efficacy of <sup>161</sup>Tb when conjugated to somatostatin receptor subtype 2 antagonists, like DOTA-LM3, which displays a much higher tumour accumulation compared to somatostatin receptor subtype 2 agonists [2, 3]. In particular, [<sup>161</sup>Tb]Tb-DOTA-LM3 exhibited superior efficacy in comparison to [<sup>177</sup>Lu]Lu-DOTATOC, which is commonly employed in neuroendocrine tumour treatment [3].

## Experimental

In this report, we present the case of the first patient with a metastatic ileal neuroendocrine tumour (NET) who underwent a test infusion of 1 GBq [<sup>161</sup>Tb]Tb-DOTA-LM3 in an on-going prospective Phase 0 study. Maximum intensity projection (MIP) SPECT images and transaxial SPECT/CT images obtained up to 168 h after infusion were performed. The scans were then compared with the MIP PET image acquired following the administration of [<sup>68</sup>Ga]Ga-DOTATATE, a standard diagnostic agent employed in the imaging of NETs. In addition, quantitative SPECT/CT was performed 3, 24, 72 and 168 h post-injection of [<sup>161</sup>Tb]Tb-DOTA-LM3, to calculate tumour and organ absorbed doses.

## Results and discussion

MIP PET image captured 1 h after intravenous administration of [<sup>68</sup>Ga]Ga-DOTATATE (a) displayed a moderate tumour burden with several lymph node, liver, and peritoneal metastases. MIP SPECT images obtained at 24 h (b) and 168 h (c), along with transaxial SPECT/CT images at 168 h (d, e) after the infusion of 1 GBq [<sup>161</sup>Tb]Tb-DOTA-LM3, exhibited satisfactory image quality, revealing the same tumour lesions displayed in the PET image. In the quantification, the prolonged mean tumour half-life of 130 h in liver metastases (red arrows), measuring 3.1 – 3.3 cm in the contrast-enhanced CT scan (f, g), resulted in a mean tumour

absorbed dose of 28 Gy/GBq. The absorbed doses for the bone marrow (black triangles), kidney, and spleen were determined as 0.31, 3.33, and 6.86 Gy/GBq, respectively. Moreover, only mild side effects were observed [4].

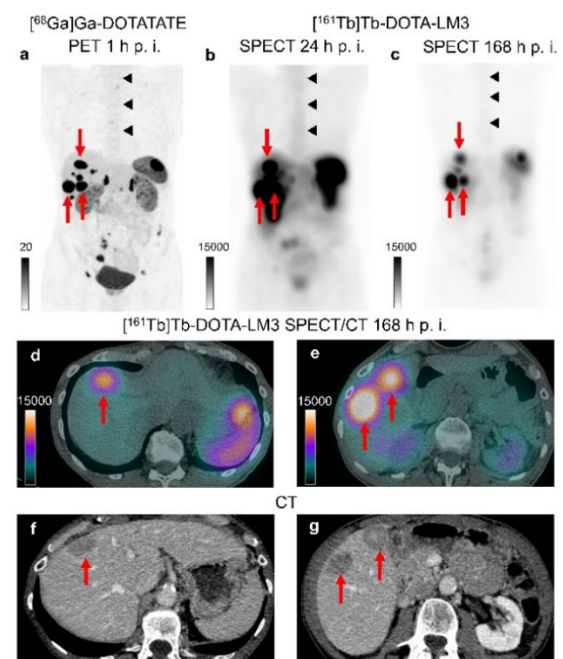


**Figure 1:** PET/CT image of a NET patient 1 h after injection of [<sup>68</sup>Ga]Ga-DOTATATE (a) and SPECT/CT image of the same patient 24 h (b), 168 h (c, d, e, f, g) after injection of [<sup>161</sup>Tb]Tb-DOTA-LM3.

In conclusion, the reported case highlights the potential of [<sup>161</sup>Tb]Tb-DOTA-LM3 as a promising clinical alternative to the existing standard radionuclide therapy involving [<sup>177</sup>Lu]Lu-DOTATOC or [<sup>177</sup>Lu]Lu-DOTATATE (Lutathera®) for patients with metastatic gastroenteropancreatic NETs [4].

## Acknowledgements

This study was funded by the Swiss National Science Foundation (no. 32003B\_205070).

## References

- [1] C. Reich et al., *Nucl. Data Sheets*, **211**, 2497-2731 (2011)
- [2] M. Fani et al., *Cancers*, **14**(5), 1172 (2022)
- [3] F. Borgna et al., *Eur. J. Nucl. Med. Mol. Imaging*, **49**(4), 1113-1126 (2022)
- [4] J. Fricke et al., *Eur. J. Nucl. Med. Mol. Imaging*, accepted, (2024)

# Improving the cyclotron production of scandium-44 towards its application in nuclear medicine

C. Favaretto (USB & PSI), P. V. Grundler (PSI), A. Sommerhalder (PSI), R. Schibli (ETHZ & PSI), N. P. van der Meulen (PSI)

## Introduction

The favourable decay properties of scandium-44 ( $E\beta^+_{av} = 630$  keV,  $T_{1/2} = 4.04$  h,  $E\gamma = 1157$  keV,  $I = 100\%$ ) present it as a promising candidate for cancer diagnosis through positron emission tomography (PET) in nuclear medicine [1]. Its similar coordination chemistry to lutetium-177, combined with the capacity to generate PET images with higher resolution compared to Ga-68, makes it also a possible alternative for diagnostic applications within theragnostic systems [2]. The ability to produce this radionuclide in sufficient quantity and quality is an important step in advancing its clinical translation.

## Experimental

Calcium oxide isotopically enriched in calcium-44 (97%, Trace Sciences International, USA) was used to prepare, through powder compression, solid targets for proton irradiation. These targets underwent irradiation with protons at the IP2 irradiation station, fed from Injector-II cyclotron (72 MeV degraded to  $\sim 10.3$  MeV with Nb) at PSI. After the irradiation, the radiochemical separation of scandium-44 from the target material was performed, employing extraction chromatography and ion exchange techniques. Specifically, various extraction resins were evaluated for the main separation between scandium and calcium. Additionally, a cation exchange column was introduced in the method to replace the final step of the previously established method [3], aiming to achieve a final product with a constant pH. At End of Separation (EOS), radionuclidic purity was evaluated through  $\gamma$ -spectrometry and radiochemical purity determined by test labelling with DOTATOC.

## Results and discussion

Activities up to 1.6 GBq were achieved at EOS. The selection of a proton energy at 10.3 MeV allowed for the minimization of scandium-44m content ( $<1\%$  at EOS), demonstrated by the  $\gamma$ -spectrum (Fig. 1a). Other radionuclidic impurities, including scandium-47, scandium-46, and yttrium-88, were present at negligible levels ( $\sim 0.1\%$  at EOS). The final activity was retrieved in a small volume ( $<1$  mL) at pH 4, which was also identified as the optimal pH for radiolabelling using scandium-44. In addition, the radiochemical purity was demonstrated as sufficient for routine labelling of DOTATOC at 25 MBq/nmol (Fig. 1b).

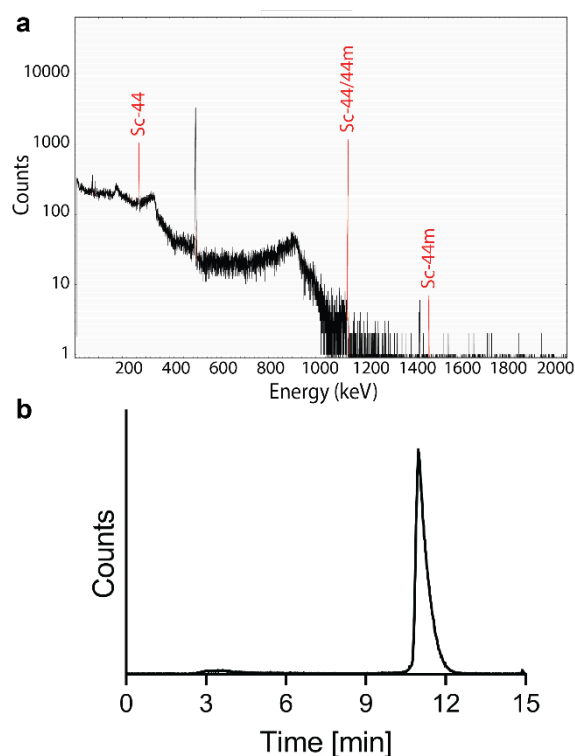


**Figure 1:**  $\gamma$ -spectrum of scandium-44 at EOS (30-min measurement; 1 m distance from the detector) (a) and radiochromatogram of the radiolabelling performed with DOTATOC (3.2 min RT indicates “free” or unlabeled scandium-44, while 10.9 min indicates [ $^{44}\text{Sc}$ ]Sc-DOTATOC).

In conclusion, this work has demonstrated the capability to generate quantities and quality suitable for both preclinical and clinical investigations. While preclinical studies have highlighted the potential applications of scandium-44 [4], there is an anticipation to translate the labelling of scandium-44 to an automated production module system within Good Manufacturing Practice (GMP), marking a significant step towards its clinical test.

## Acknowledgements

This study was funded by the Swiss National Science Foundation (no. 32003B\_205070).

## References

- [1] J. Chen et al., *Nucl. Data Sheets*, **112**, 2357-2495 (2011)
- [2] F. Rösch et al., *Dalton. Trans.*, **40**, 6104-6111 (2011)
- [3] C. Müller et al., *J. Nucl. Med.*, **54**, 2168-2174 (2013)
- [4] N. van der Meulen et al., *Molecules*, **25**, 4706 (2020)

# Research studies towards production of medical isotopes using ISOL techniques

M. Mostamand (PSI)

## Introduction

TATTOOS project aims to provide a unique research opportunity with radionuclides in Switzerland and Europe. Radioactive isotopes are generated through spallation, fragmentation, and fission reactions in suitable target materials with 590 MeV proton beam from HIPA. The facility is based on the ISOL (Isotope Separation Online) technique. Radioactive ion beams are extracted from thick targets composed of a variety of refractory materials. The production rate of specific isotopes (Z, A) is determined by their production cross section for the given proton beam energy, proton beam intensity and the target thickness.

The production rates can be optimized through the choice of target material and thickness. The proton beam intensity is limited to 100  $\mu\text{A}$ , therefore the admissible beam intensity is constrained by ability of the target dissipate the deposited beam power without exceeding the nominal target operating temperature.

A typical high-power tantalum metal foil target [1] can accept up to 70  $\mu\text{A}$  at a thickness of 0.14 mol/cm<sup>2</sup> and an operating temperature of 2300 °C. A composite ceramic uranium carbide target [2] with a typical thickness of 0.05 mol uranium/cm<sup>2</sup> can take up to 20  $\mu\text{A}$  proton at 1950 °C.

The operating temperature is determined by the vapor pressure of the target material. The pressure inside the target needs to be kept at high-vacuum levels (<10–5 mbar) to preserve the ion source efficiency and structural integrity over run periods of up to 4 weeks (TRIUMF experience). The target temperature depends on power deposition and the efficiency of power dissipation, governed by the thermal conductivity of the target material and the emissivity of the target container. The resulting target temperature limitations can be detrimental to the efficient and fast release of isotopes through diffusion and effusion which benefits from high operating temperatures. The best balance between these two opposing requirements can be achieved by using refractory materials with high thermal stability, low vapor pressure and good thermal conductivity.

For the ionization process a variety of ion source options can be utilized [3]. Which ionization method is most suitable, depends strongly on the ionization potential of the atoms or molecules released from the target. The isotopes in TATTOOS will be ionized with a

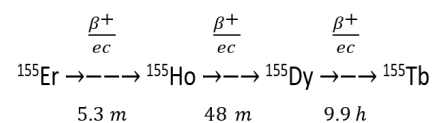
surface ion source or by resonant laser ionization.

To produce heavy isotopes for targeted alpha therapy research, composite ceramic uranium carbide targets [2] will be used. Neutron-deficient isotopes for medical applications in the lanthanide region are efficiently produced from tantalum metal foil targets, which are filled with several hundred 25  $\mu\text{m}$  thick Ta foil disks.

## Production of Tb isotopes

The TRIUMF Isotope Database [4] is maintained as a publicly accessible website. It provides options for users to extract public information on RIB yields, production rates, target configurations and operating conditions. A crucial part of planning the experiment is to determine the most suitable target and beamtime required to collect the desired amount of different Tb isotopes.

<sup>155</sup>Tb: a simulation data search through FLUKA and GEANT4 data sets indicates that for isotopes at A = 155 from Ta targets, the peak production at this mass is around Z = 68, <sup>155</sup>Er. The ISAC mass separator at TRIUMF transmits all isobars at A/q = 155 with equal efficiency. As shown in below equation, radioactive isotopes produced at the highest rates decay through  $\beta^+$ /electron capture and eventually built-up activity of relatively long-lived <sup>155</sup>Tb ( $t_{1/2} = 5.32$  d).



Thus, the most efficient way to produce high activities of <sup>155</sup>Tb in the shortest possible beamtime is to collect the isobaric RIB components Er, Ho, and Dy which are produced at higher rates than <sup>155</sup>Tb. The same process can be implemented for <sup>152</sup>Tb. Besides the collection of isobaric components of Tb discussed above, Tb can also be produced through laser ionization [5]. The two laser ionization schemes presented in [5] have been tried at TRIUMF. The yield results indicate a proper efficiency of <sup>155</sup>Tb and <sup>152</sup>Tb with respect to surface ionization. However, the production of <sup>149</sup>Tb was not confirmed using these laser schemes. This could be either due to the massive background isobaric contamination from other lanthanides in this region or there might be an isotopeshift that needs to be investigated.

## Prospects

To investigate and understand the efficient method to produce all favorite isotopes of Tb, one can consider to laser ionize all isobaric components of certain Tb isotope simultaneously.

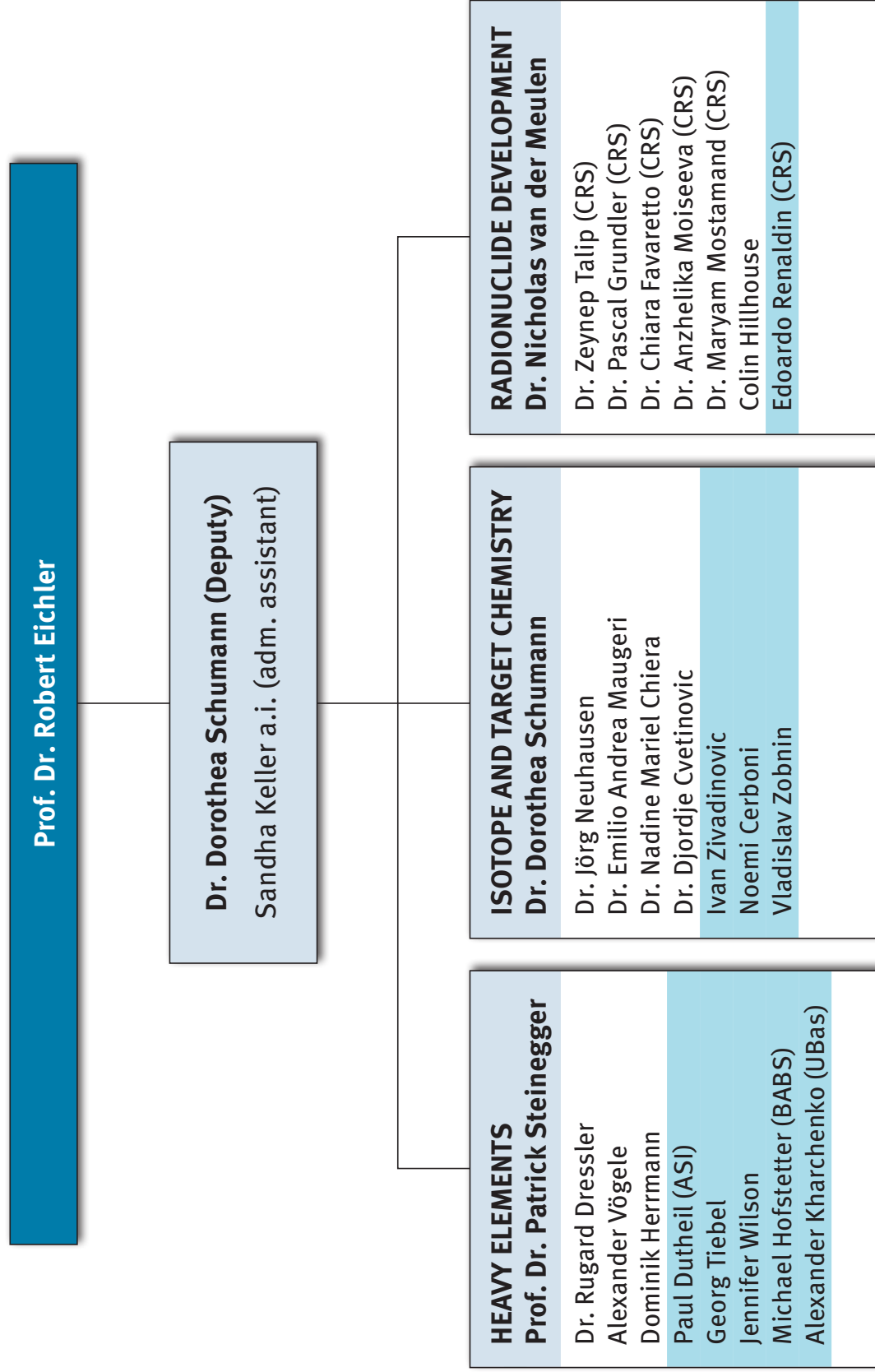
Another factor that needs to be investigated in more details is the saturation of the ionizer tube. This can be evaluated off-line.

The production of  $^{149}\text{Tb}$  using laser ionization requires a different ion source other than surface ion source to suppress some background contamination coming from the source and be able to detect the effect of laser on the production of this isotope. This can be studied at TRIUMF using ion guide laser ion source (IGLIS) [6].

## References

- [1] M. Dombisky et al., *Nucl. Instrum. Methods Phys. Res. B*, **204** (2003)
- [2] P. Kunz et al., *J. Nucl. Mater.*, **440**(1-3), 110-116 (2013)
- [3] P. G. Bricault et al., *Nucl. Instrum. Methods Phys. Res. B*, **366**, 34 (2016)
- [4] P. Kunz, TRIUMF Isotope Database, <https://yield.targets.triumf.ca> (2022)
- [5] V. M. Gadelshin, et al., *Front. Med.*, **8**, (2021)
- [6] S. Raeder, et al., *Rev. Sci. Instrum.*, **85**, 033309 (2014)

31.12.2023



### List of publication 2023

Alcayne, V.; Cano-Ott, D.; Garcia, J.; González-Romero, E.; Martínez, T.; Mendoza, E.; Sánchez, A.; Plaza, J.; Balibrea-Correa, J.; Casanovas, A.; et al.

*A segmented total energy detector (sTED) for (n,  $\gamma$ ) cross section measurements at n\_TOF EAR2*  
EPJ Web Conf. 2023, 284, 01043 (01045 pp.), <https://doi.org/10.1051/epjconf/202328401043>

Alcayne, V.; Mendoza, E.; Cano-Ott, D.; Kimura, A.; Aberle, O.; Amaducci, S.; Andrzejewski, J.; Audouin, L.; Babiano-Suarez, V.; Bacak, M.; et al.

*Results of the  $^{244}\text{Cm}$ ,  $^{246}\text{Cm}$  and  $^{248}\text{Cm}$  neutron-induced capture cross sections measurements at EAR1 and EAR2 of the n\_TOF facility*  
EPJ Web Conf. 2023, 284, 01009 (01006 pp.), <https://doi.org/10.1051/epjconf/202328401009>

Babiano-Suarez, V.; Balibrea-Correa, J.; Caballero-Ontanaya, L.; Domingo-Pardo, C.; Ladarescu, I.; Lerendegui-Marco, J.; Tain, J.L.; Calviño, F.; Casanovas, A.; Tarifeño-Saldivia, A.; et al.

*High resolution  $^{80}\text{Se}(n,\gamma)$  cross section measurement at CERN n\_TOF*  
EPJ Web Conf. 2023, 284, 01001 (01006 pp.), <https://doi.org/10.1051/epjconf/202328401001>

Balibrea-Correa, J.; Babiano-Suárez, V.; Lerendegui-Marco, J.; Domingo-Pardo, C.; Ladarescu, I.; Tarifeño-Saldivia, A.; Alcayne, V.; Cano-Ott, D.; González-Romero, E.; Martínez, T.; et al.

*First measurement of the  $^{94}\text{Nb}(n,\gamma)$  cross section at the CERN n\_TOF facility*  
EPJ Web Conf. 2023, 279, 06004 (06008 pp.), <https://doi.org/10.1051/epjconf/202327906004>

Beyer, D.; Vaccarin, C.; Deupi, X.; Mapanao, A.K.; Cohrs, S.; Sozzi-Guo, F.; Grundler, P.V.; van der Meulen, N.P.; Wang, J.; Tanriver, M.; et al.

*A tool for nuclear imaging of the SARS-CoV-2 entry receptor: molecular model and preclinical development of ACE2-selective radiopeptides*  
EJNMMI Res. 2023, 13(1), 32 (14 pp.), <https://doi.org/10.1186/s13550-023-00979-2>

Borghesi, M.; Alpert, B.; Balata, M.; Becker, D.; Bennet, D.; Celasco, E.; Cerboni, N.; De Gerone, M.; Dressler, R.; Faverzani, M.; et al.

*An updated overview of the HOLMES status*  
Nucl. Instrum. Methods Phys. Res. A 2023, 1051, 168205 (168203 pp.),  
<https://doi.org/10.1016/j.nima.2023.168205>

Chen, K.; Mackiewicz, A.; Virtanen, S.; Grundler, P.V.; Seifert, H.-P.; Ritter, S.

*Effect of zinc injection on mitigating stress corrosion cracking initiation of structural materials in light water reactor primary water*  
Corrosion Reviews, 2023, 41(3), 2023, pp. 387-398. <https://doi.org/10.1515/corrrev-2022-0098>

Chiera, N.M.; Aksenov, N.V.; Albin, Y.V.; Bodrov, A.Y.; Bozhikov, G.A.; Chuprakov, I.; Dmitriev, S.N.; Dressler, R.; Eichler, R.; Kraus, B.; et al.

*Observation of a volatile astatine hydroxide species in online gas-adsorption thermochromatography experiments*  
Mol. Phys. 2023, e2272685 (2272610 pp.), <https://doi.org/10.1080/00268976.2023.2272685>

Chiera, N.M.; Dressler, R.; Sprung, P.; Talip, Z.; Schumann, D.

*Determination of the half-life of gadolinium-148*  
Appl. Radiat. Isot. 2023, 194, 110708 (110705 pp.), <https://doi.org/10.1016/j.apradiso.2023.110708>

De Gerone, M.; Bevilacqua, A.; Borghesi, M.; Cerboni, N.; Ceruti, G.; De Bodin De Galembert, G.; Faverzani, M.; Fedkevych, M.; Ferri, E.; Gallucci, G.; et al.

*Development and commissioning of the ion implanter for the HOLMES experiment*

Nucl. Instrum. Methods Phys. Res. A 2023, 1051, 168168 (168163 pp.),

<https://doi.org/10.1016/j.nima.2023.168168>

Dellepiane, G.; Casolaro, P.; Favaretto, C.; Gottstein, A.; Grundler, P.V.; Mateu, I.; Renaldin, E.; Scampoli, P.; Talip, Z.; van der Meulen, N.P.; et al.

*Cross-section measurement of thulium radioisotopes with an 18 MeV medical PET cyclotron for an optimized  $^{165}\text{Er}$  production*

Appl. Radiat. Isot. 2023, 200, 110954 (110911 pp.), <https://doi.org/10.1016/j.apradiso.2023.110954>

Dietz, M.; Lederer-Woods, E.; Tattersall, D.; Battino, A.; Günsing, O.; Heinitz, S.; Krlička, J.; Leredegui-Marco, J.; Reifarth, L.; Valenta, V.; et al.

*The stellar  $^{72}\text{Ge}(n, \gamma)$  cross section for weak s-process: a first measurement at  $n_{\text{TOF}}$*

EPJ WEB Conf. 2023, 284, 01017 (01014 pp.), <https://doi.org/10.1051/epjconf/202328401017>

Domingo-Pardo, C.; Aberle, O.; Alcayne, V.; Altieri, S.; Amaducci, S.; Andrzejewski, J.; Babiano-Suarez, V.; Bacak, M.; Balibrea, J.; Beltrami, C.; et al.

*The neutron time-of-flight facility  $n_{\text{TOF}}$  at CERN: recent facility upgrades and detector developments*

J. Phys.: Conf. Ser. 2023, 2586, 012150 (012111 pp.), [https://doi.org/10.1088/1742-](https://doi.org/10.1088/1742-6596/2586/1/012150)

[6596/2586/1/012150](https://doi.org/10.1088/1742-6596/2586/1/012150)

Domingo-Pardo, C.; Babiano-Suarez, V.; Balibrea-Correa, J.; Caballero, L.; Ladarescu, I.; Leredegui-Marco, J.; Tain, J.L.; Tarifeño-Saldivia, A.; Aberle, O.; Alcayne, V.; et al.

*Advances and new ideas for neutron-capture astrophysics experiments at CERN  $n_{\text{TOF}}$*

Eur. Phys. J. A 2023, 59(1), 8 (11 pp.), <https://doi.org/10.1140/epja/s10050-022-00876-7>

Domingo-Pardo, C.; Babiano-Suarez, V.; Balibrea-Correa, J.; Caballero, L.; Ladarescu, I.; Leredegui-Marco, J.; Tarifeño-Saldivia, A.; Aberle, O.; Alcayne, V.; Altieri, S.; et al.

*Compton imaging for enhanced sensitivity ( $n, \gamma$ ) cross section TOF experiments: status and prospects*

EPJ WEB Conf. 2023, 284, 01018 (01015 pp.), [10.1051/epjconf/202328401018](https://doi.org/10.1051/epjconf/202328401018).

Dupont, E.; Otuka, N.; Rochman, D.; Nogèure, G.; Aberle, O.; Alcayne, V.; Altieri, S.; Amaducci, S.; Andrzejewski, J.; Babiano-Suarez, V.; et al.

*Overview of the dissemination of  $n_{\text{TOF}}$  experimental data and resonance parameters*

EPJ WEB Conf. 2023, 284, 18001 (18004 pp.), <https://doi.org/10.1051/epjconf/202328418001>

Durďáková, T.-M.; Hrdlička, Z.; Král, M.; Hovorka, Š.; Vögele, A.; Eichler, R.; Trtik, P.; Vopička, O.

*Radiation softening and hardening of PDMS in combined neutron and  $\gamma$  rays*

Polym. Degrad. Stab., 2023, 208, 110241 (110247 pp.),

<https://doi.org/10.1016/j.polymdegradstab.2022.110241>

Favaretto, C.; Grundler, P.V.; Talip, Z.; Landolt, S.; Sepini, L.; Köster, U.; Müller, C.; Schibli, R.; Geistlich, S.; van der Meulen, N.P.

*$^{161}\text{Tb}$ -DOTATOC production using a fully automated disposable cassette system: a first step toward the introduction of  $^{161}\text{Tb}$  into the clinic*

J. Nucl. Med. 2023, 64(7), 1138-1144, <https://doi.org/10.2967/jnumed.122.265268>

Ferri, E.; Alpert, B.; Balata, M.; Becker, D.; Bennet, D.; Borghesi, M.; Cerboni, N.; De Gerone, M.; Dressler, R.; Faverzani, M.; et al.

*Status of HOLMES, an experiment for measuring the  $v$  mass*

Neutrino oscillation workshop (NOW 2022), 2023, 421, 076 (073 pp.),

<https://doi.org/10.22323/1.421.0076>

García-Infantes, M.E.; Praena, P.; Casanovas, P.; Mastromarco, M.; Aberle, M.; Alcayne, M.; Altieri, S.; Amaducci, C.; Amar Es-Sghir, D.; Andrzejewski, A.; et al.

*First high resolution measurement of neutron capture resonances in  $^{176}\text{Yb}$  at the  $n_{\text{TOF}}$  CERN facility*

EPJ WEB Conf. 2023, 284, 09001 (09005 pp.), <https://doi.org/10.1051/epjconf/202328409001>

Garg, R.; Dellmann, S.; Lederer-Woods, C.; Bruno, C.G.; Eberhardt, K.; Geppert, C.; Heftrich, T.; Kajan, I.; Käppeler, F.; Phoenix, B.; et al.

*$^{179}\text{Ta}(n, \gamma)$  cross-section measurement and the astrophysical origin of the  $^{180}\text{Ta}$  isotope*

Phys. Rev. C 2023, 107(4), 045805 (045807 pp.), <https://doi.org/10.1103/PhysRevC.107.045805>

Happl, B.; Brandt, M.; Balber, T.; Benčurová, K.; Talip, Z.; Voegelé, A.; Heffeter, P.; Kandioller, W.; Van der Meulen, N.P.; Mitterhauser, M.; et al.

*Synthesis and preclinical evaluation of radiolabeled  $^{103}\text{Ru}$ BOLD-100*

Pharm. 2023, 15(11), 2626 (2611 pp.), <https://doi.org/10.3390/pharmaceutics15112626>

Juget, F.; Durán, T.; Nedjadi, Y.; Talip, Z.; Grundler, P.V.; Favaretto, C.; Casolaro, P.; Dellepiane, G.; Braccini, S.; Bailat, C.; et al.

*Activity measurement of  $^{44}\text{Sc}$  and calibration of activity measurement instruments on production sites and clinics*

Molecules 2023, 28(3), 1345 (1310 pp.), <https://doi.org/10.3390/molecules28031345>

Juget, F.; van Dijk, M.; Maugeri, E.A.; Schumann, M.D.; Heinitz, S.; Boyarsky, A.; Köster, U.; Shchutska, L.; Bailat, C.

*Measurement of the  $^{171}\text{Tm}$  beta spectrum*

Appl. Radiat. Isot. 2023, 202, 111058 (111056 pp.), <https://doi.org/10.1016/j.apradiso.2023.111058>

Kiselev, D.; Baumann, P.; Duperrex, P.A.; Haj Tahar, M.; Jollet, S.; Knecht, A.; Laube, D.; Reggiani, D.; Snuverink, J.; Sobbia, R.; et al.

*The PSI meson target facility and its upgrade IMPACT-HIMB*

EPJ WEB Conf. 2023, 285, 07002 (07004 pp.), <https://doi.org/10.1051/epjconf/202328507002>

Kiselev, D.; Eichler, R.; Haj Tahar, M.; Hartmann, M.; Kirch, A.; Knecht, K.; Koschik, A. D.; Laube, Rauber, T.; Reggiani, D.; R. Schibli; J. Snuverink, U. Wellenkamp; H. Zhang, N.P. van der Meulen

*IMPACT: A Substantial Upgrade to the HIPA Infrastructure at PSI*

JACoW 2023, 34-37 <https://doi:10.18429/JACoW-CYCLOTRONS2022-MOBO02>

Kossert, K.; Veicht, M.; Mihalcea, I.; Nedjadi, Y.; Schumann, D.; Symochko, D.

*Activity standardization of  $^{32}\text{Si}$  at PTB*

Appl. Radiat. Isot., 2023, 202, 111042 (111018 pp.), <https://doi.org/10.1016/j.apradiso.2023.111042>

Lerendegui-Marco, J.; Babiano-Suárez, V.; Balibrea-Correa, J.; Domingo-Pardo, C.; Ladarescu, I.; Tarifeño-Saldivia, A.; Alcayne, V.; Cano-Ott, D.; González-Romero, E.; Martínez, T., et al.

*New detection systems for an enhanced sensitivity in key stellar ( $n, \gamma$ ) measurements*

EPJ WEB Conf. 2023, 279, 13001 (13007 pp.), <https://doi.org/10.1051/epjconf/202327913001>

Lerendegui-Marco, J.; Casanovas, A.; Alcayne, V.; Aberle, O.; Altieri, S.; Amaducci, S.; Andrzejewski, J.; Babiano-Suarez, V.; Bacak, M.; Balibrea, J.; et al.

*New perspectives for neutron capture measurements in the upgraded CERN-n\_TOF Facility*  
EPJ WEB Conf. 2023, 284, 01028 (01026 pp.), <https://doi.org/10.1051/epjconf/202328401028>

Manna, A.; Pirovano, E.; Colonna, N.; Castelluccio, D.; Console Camprini, P.; Cosentino, L.; Dietz, M.; Ducasse, Q.; Finocchiaro, P.; Le Naour, C.; et al.

*Characterization of a detector setup for the measurement of the  $^{235}\text{U}(n,f)$  cross section relative to  $n$ - $p$  scattering up to 500 MeV at the n\_TOF facility at CERN*  
EPJ WEB Conf. 2023, 284, 04016 (04015 pp.), <https://doi.org/10.1051/epjconf/202328404016>

Massimi, C.; Aberle, O.; Alcayne, V.; Altieri, S.; Amaducci, S.; Andrzejewski, J.; Babiano-Suarez, V.; Bacak, M.; Balibrea, J.; Beltrami, C.; et al.

*Neutron-induced cross section measurements*  
EPJ WEB Conf. 2023, 279, 11009 (11006 pp.), <https://doi.org/10.1051/epjconf/202327911009>

Mastromarco, M.; Manna, A.; García-Infantes, F.; Amaducci, S.; Mengoni, A.; Massimi, C.; Tagliente, G.; Cristallo, S.; Aberle, O.; Alcayne, V.; et al.

*Measurement of the  $^{160}\text{Gd}(n,\gamma)$  cross section at n\_TOF and its medical implications*  
EPJ WEB Conf. 2023, 284, 09002 (09005 pp.), <https://doi.org/10.1051/epjconf/202328409002>

Michalopoulou, V.; Diakaki, M.; Vlastou, R.; Kokkoris, M.; Stamatopoulos, A.; Tsinganis, A.; Eleme, Z.; Patronis, N.; Heyse, J.; Schillebeeckx, P.; et al.

*Measurement of the  $^{235}\text{U}(n,f)$  cross section relative to the  $^{10}\text{B}(n,\alpha)$  reaction with micromegas detectors at the CERN n\_TOF facility: first results*  
EPJ WEB Conf. 2023, 284, 01030 (01034 pp.), <https://doi.org/10.1051/epjconf/202328401030>

Michalopoulou, V.; Stamatopoulos, A.; Diakaki, M.; Tsinganis, A.; Vlastou, R.; Kokkoris, M.; Patronis, N.; Eleme, Z.; Macina, D.; Tassan-Got, L.; et al.

*Measurement of the neutron-induced fission cross section of  $^{230}\text{Th}$  at the CERN n\_TOF facility*  
Phys. Rev. C 2023, 108(1), 014616 (014615 pp.), <https://doi.org/10.1103/PhysRevC.108.014616>

Mitrano, D.M.; Milić, J.V.; Steinegger, P.; Merz, L.

*Reflections on the SCNAT young faculty meeting 2023: effective communication within academia and beyond*  
Chimia 2023, 77(9), <https://doi.org/628-631>, 10.2533/chimia.2023.628

Mucciola, R.; Paradela, C.; Manna, A.; Alaerts, G.; Massimi, C.; Kopecky, S.; Mengoni, A.; Moens, A.; Schillebeeckx, P.; Wynants, R.; et al.

*Neutron capture and total cross-section measurements on  $^{94,95,96}\text{Mo}$  at n\_TOF and GELINA*  
EPJ WEB Conf. 2023, 284, 01031 (01034 pp.), <https://doi.org/10.1051/epjconf/202328401031>

Müller, C.; van der Meulen, N.P.; Schibli, R.

*Opportunities and potential challenges of using terbium-161 for targeted radionuclide therapy in clinics*  
Eur. J. Nucl. Med. and Molecular Imaging 2023, 50, 3181-3184, <https://doi.org/10.1007/s00259-023-06316-y>

Nedjadi, Y.; Durán, M.T.; Juget, F.; Bochud, F.; Veicht, M.; Schumann, D.; Mihalcea, I.; Kossert, K.; Bailat, C.

*Activity standardisation of  $^{32}\text{Si}$  at IRA-METAS*

Appl. Radiat. Isot. 2023, 202, 111041 (111015 pp.), <https://doi.org/10.1016/j.apradiso.2023.111041>

Nurkić, D.; Milin, M.; Jelavić Malenica, D.; Vukman, N.; Vidović, N.; Soić, N.; Figuera, P.; Di Pietro, A.; Cherubini, S.; Čolović, P.; et al.

*Cluster states in carbon isotopes  $^{13-15}\text{C}$  studied with the  $^{10}\text{Be}+^9\text{Be}$  reactions*

Acta Phys. Pol. B 2023, 14(6), 4-A32 (35 pp.), <https://doi.org/10.5506/APhysPolBSupp.16.4-A32>

Oprea, A.; Gunging, F.; Schillebeeckx, P.; Aberle, O.; Bacak, M.; Berthoumieux, E.; Cano-Ott, D.; Diakaki, M.; Dupont, E.; Geslot, B.; et al.

*Measurement of the  $^{241}\text{Am}(n,\gamma)$  cross section at the  $n_{\text{TOF}}$  facility at CERN*

EPJ WEB Conf. 2023, 284, 01036 (01034 pp.), <https://doi.org/10.1051/epjconf/202328401036>

Patronis, N.; Mengoni, A.; Goula, S.; Aberle, O.; Alcayne, V.; Altieri, S.; Amaducci, S.; Andrzejewski, J.; Babiano-Suarez, V.; Bacak, M.; et al.

*Status report of the  $n_{\text{TOF}}$  facility after the 2<sup>nd</sup> CERN long shutdown period*

EPJ Tech. Instrum. 2023, 10(1), 13 (10 pp.), <https://doi.org/10.1140/epjti/s40485-023-00100-w>

Pavón-Rodríguez, J.A.; Alcayne, V.; Amaducci, S.; Bacak, M.; Casanovas, A.; Cortés-Giraldo, M.A.; García-Infantes, F.; Lerendegui-Marco, J.; Manna, A.; Musacchio-Gonzalez, E.; et al.

*Characterisation of the  $n_{\text{TOF}}$  20 m beam line at CERN with the new spallation target*

EPJ WEB Conf. 2023, 284, 06006 (06006 pp.), <https://doi.org/10.1051/epjconf/202328406006>

Pirovano, V.; Manna, D.; Colonna, J.; Console Camprini, E.; Cosentino, T.; Dietz, E.; Ducasse, A.; Finocchiaro, J.; Massimi, J.; Mengoni, A.; et al.

*Detector set up for the measurements of the neutron-induced fission cross section of  $^{235}\text{U}$  relative to  $n$ - $p$  scattering up to 150 MeV at CERN- $n_{\text{TOF}}$*

EPJ WEB Conf. 2023, 284, 01043 (01045 pp.), <https://doi.org/10.1051/epjconf/202328404019>

Radzina, M.; Saule, L.; Mamis, E.; Koester, U.; Cocolios, T. E.; Pajuste, E.; Kalnina, M.; Palskis, K.; Sawitzki, Z.; Talip Z.; Jensen, M.; Duchemin, C.; Leufgen, K.; Stora T.

*Novel radionuclides for use in Nuclear Medicine in Europe: where do we stand and where do we go?*

EJNMMI Radiopharmacy and Chemistry 2023, 8, 27. <https://doi.org/10.1186/s41181-023-00211-5>

Renaldin, E.; Dellepiane, G.; Braccini, S.; Sommerhalder, A.; Zhang, H.; van der Meulen, N.P.; Eichler, R.; Talip, Z.

*Study of thulium-167 cyclotron production: a potential medically-relevant radionuclide*

Front. Chem. 2023, 11, 1288588 (1288514 pp.), <https://doi.org/10.3389/fchem.2023.1288588>

Schumann, D.

*The 30<sup>th</sup> conference of the International Nuclear Target Development Society, INTDS 2022*

Nucl. Phys. News 2023 33(2), 28-29, <https://doi.org/10.1080/10619127.2023.2168921>

Sosnin, N.V.; Lederer-Woods, C.; Krtička, M.; Garg, R.; Dietz, M.; Bacak, M.; Barbagallo, M.; Battino, U.; Cristallo, S.; Damone, L.A.; et al.

*Measurement of the  $^{77}\text{Se}(n,\gamma)$  cross section up to 200 keV at the  $n_{\text{TOF}}$  facility at CERN*

Phys. Rev. C 2023, 107(6), 065805 (065809 pp.), <https://doi.org/10.1103/PhysRevC.107.065805>

Stamati, M.E.; Torres-Sánchez, P.; Pérez-Maroto, P.; Cecchetto, M.; Goula, M.; Mastromarco, M.; Chasapoglou, S.; Beltrami, C.; Chiesa, D.; Manna, A.; et al.

*EPJ WEB Conf.* 2023, 284, 06009 (06007 pp.), <https://doi.org/10.1051/epjconf/202328406009>

Torres-Sánchez, P.; Praena, J.; Porras, I.; Sabaté-Gilarte, M.; Lederer-Woods, C.; Aberle, O.; Alcayne, V.; Amaducci, S.; Andrzejewski, J.; Audouin, L.; et al.

*Measurement of the  $1^{4N}(n,p)^{14}C$  cross section at the CERN n\_TOF facility from subthermal energy to 800 keV*

*Phys. Rev. C* 2023, 107(6), 064617 (064615 pp.), <https://doi.org/10.1103/PhysRevC.107.064617>

Tschan, V.J.; Busslinger, S.D.; Bernhardt, P.; Grundler, P.V.; Zeevaart, J.R.; Köster, U.; van der Meulen, N.P.; Schibli, R.; Müller, C.

*Albumin-binding and conventional PSMA ligands in combination with  $^{161}Tb$ : biodistribution, dosimetry, and preclinical therapy*

*J. Nucl. Med.* 2023, 64(10), 1625-1631, <https://doi.org/10.2967/jnumed.123.265524>

Wallner, A.; Fifield, L.K.; Froehlich, M.B.; Koll, D.; Leckenby, G.; Martschini, M.; Pavetich, S.; Tims, S.G.; Schumann, D.; Slavkovská, Z.

*Accelerator mass spectrometry with ANU's 14 million volt accelerator*

*Nucl. Instrum. Methods Phys. Res. B* 2023, 534, 48-53, <https://doi.org/10.1016/j.nimb.2022.10.021>

Wilson, J.M.; Mihalcea, I.; Veicht, M.; Cvjetinović, Đ.; Schumann, D.

*Recovery of no-carrier-added  $^{41}Ca$ ,  $^{44}Ti$ , and  $^{26}Al$  from high-energy proton-irradiated vanadium targets*

*Radiochim. Acta* 2023, 111(4), 265-271, <https://doi.org/10.1515/ract-2022-0072>

### Contributions to conferences, workshops and seminars

N. Cerboni et al.

*In-Depth Characterization of Targets Prepared by Coupled Reduction (poster)*

Scholar Fund of the Swiss Chemical Industry Symposium, ETHZ, Zurich, Switzerland, January 19, 2023

N. Cerboni

*Updates on the Reduction of Lanthanides*

LRC Seminar, PSI, Villigen PSI, Switzerland, March 3, 2023

N. Cerboni

*Electrodeposited thin films of metallic radiolanthanides for Auger Electron Spectroscopy*

Symposium of the Laboratory of Inorganic Chemistry (LAC), ETHZ, Zurich, Switzerland, May 3, 2023

N. Cerboni et al.

*Electrodeposition of thin films of metallic Radiolanthanides from Ionic Liquids as Sources for Auger Electron Spectroscopy (poster)*

NES PhD Day 2023, PSI, Villigen PSI, Switzerland, May 9, 2023

N. Cerboni

*Recent advances of targets produced by coupled reduction*

7th International Conference on the Chemistry and Physics of the Transactinide Elements (TAN 23), Huizhou, China, November 12 – 17, 2023

N. Cerboni et al.

*Preparation of sources of medically relevant radiolanthanides for Auger electron spectroscopy (poster)*

NES-ENE FoKo Event 2023, PSI, Villigen PSI, Switzerland, December 4, 2023

Đ. Cvjetinović,  
*Kick off meeting (talk)*

RadioMag Collaboration Board Meeting, Vinča, Belgrade, Serbia, December 11 – 15, 2023

Đ. Cvjetinović  
*Novel concept of a  $^{44}\text{Ti}/^{44}\text{Sc}$  generator (poster)*

NES-ENE FoKo Event 2023, PSI, Villigen PSI, Switzerland, December 4, 2023

P. Duthel  
*An electrochemical approach for routine radioanalytical separations of radionuclides (seminar talk)*  
LRC Seminar, PSI, Villigen PSI, Switzerland, March 3, 2023

P. Duthel et al.  
*An electrochemical approach for routine radioanalytics (poster)*  
NES PhD Day 2023, PSI, Villigen PSI, Switzerland, May 9, 2023

P. Duthel  
*Electrochemical approach for routine separation and analysis of radionuclides (talk)*  
SCF Congress, Nantes, France, June 26 – 28, 2023

P. Duthel et al.  
*Electrochemical approach for routine radioanalytical separations (poster)*  
SCS Fall Meeting 2023, Universität Bern, Bern, Switzerland, August 24 – 25, 2023

P. Duthel  
*Flow electrolytic approach for separation and analysis of radionuclides (talk)*  
Radioanalytik-Seminar, FHNW Campus Brugg, Brugg, Switzerland, December 06 – 07, 2023

P. Duthel et al.  
*Electrochemical approach for routine radioanalytical separations (poster)*  
NES-ENE FoKo Event 2023, PSI, Villigen PSI, Switzerland, December 4, 2023

R. Dressler  
*Half-life determination of  $^{53}\text{Mn}$  (talk)*  
RANC 2023, Budapest, Hungary, May 07 – 12, 2023

R. Dressler  
*Measurement of neutron capture cross sections at stellar energies at the n\_TOF a-NEAR Station (talk)*  
The n\_TOF Collaboration General Meeting, Valencia, Spain, November 22 – 24, 2023

R. Eichler  
*Superheavy Element Research in Switzerland (invited talk)*  
International IUPAP Conference Heaviest nuclei and atoms, Yerevan, Armenia, April 24-30, 2023

R. Eichler  
*Current and Future Isotope Production in Switzerland (invited talk)*  
Seminar of the Institute of Modern Physics (IMP) of the Chinese Academy of Sciences, Lanzhou, China, July 24, 2023

R. Eichler  
*The PSI perspective towards the TATTOOS online separator (online talk)*  
PRISMAP CM6 Meeting, November 29, 2023

R. Eichler  
*IMPACT-TATTOOS: Take radionuclide production and application at PSI to the next level (invited talk)*  
PSI-Mitarbeiterinformation, PSI, Villigen PSI, Switzerland, January 31, 2023

R. Eichler

*Current and Future Isotope Production in Switzerland (invited talk)*

Seminar of the Cyclotron Institute, Texas A&M University, College Station, Texas, USA, August 11, 2023

R. Eichler

*Implication of "surface inhomogeneity" and "kinetics of deposition" on gas chromatography (talk)*

7th International Conference on the Chemistry and Physics of the Transactinide Elements (TAN 23), Huizhou, China, November 12 – 17, 2023

R. Eichler

*IMPACT-TATTOOS: Take radionuclide production and application at PSI to the next level (talk)*

Seminar Collaboration visit to TRIUMF, Vancouver, Canada, April 12, 2023

C. Favaretto

*Introduction of  $^{161}\text{Tb}$  into the clinics through its automated purification and the Good Manufacturing Practice compliant production of  $^{161}\text{Tb}$ -DOTA-LM3 (talk)*

iSRS 2023, Honolulu, USA, May 22 – 26, 2023

C. Favaretto

*Development of terbium radioisotopes towards clinical theragnostic applications in nuclear medicine (invited talk)*

II Meeting Internazionale Giovani Ricercatori Italiani in Sede all'Estero, Reggio Emilia, Italy, October 14, 2023

P. V. Grundler et al.

*Paving the way to provide the therapeutic radionuclide  $^{161}\text{Tb}$  for clinical studies: challenges and lessons learned (poster)*

SCS Fall Meeting 2023, Universität Bern, Bern, Switzerland, August 24 – 25, 2023

M. Hofstetter et al.

*Lanthanoid patterns in Nuclear Forensics (poster)*

SSCI Symposium 2023, ETH Zürich (ETH Hönggerberg), Zürich, Switzerland, January 19, 2023

M. Hofstetter et al.

*Ultra-trace Lanthanoid Impurities in Nuclear Forensic Applications (poster)*

NES PhD Day 2023, PSI, Villigen PSI, Switzerland, May 9, 2023

M. Hofstetter

*Lanthanoid patterns in nuclear material – A new analytical approach (talk)*

Annual Meeting of the International Technical Working Group in Nuclear Forensics (ITWG), Tbilisi, Georgia, June 19 – 23, 2023

M. Hofstetter et al.

*Nuclear Forensic Investigations of High Purity Depleted Uranium Ammunition (poster)*

SCS Fall Meeting 2023, Universität Bern, Bern, Switzerland, August 24 – 25, 2023

A. M. Ivan

*Fellowship at PSI*

LRC Seminar, PSI, Villigen PSI, Switzerland, February 20, 2023

J. Neuhausen

*WP12- Chemistry control experiments and modelling (online talk)*

PATRICIA 6th Technical Coordination Board Meeting, April 3, 2023

J. Neuhausen

*WP12- Chemistry control experiments and modelling (online talk)*

PATRICIA 4th Technical Review Meeting, April 3, 2023

J. Neuhausen

*WP12- Chemistry control experiments and modelling (talk)*

PATRICIA 7th Technical Coordination Board Meeting, Aix-en-Provence, France, October 10, 2023

J. Neuhausen

*WP12- Chemistry control experiments and modelling (talk)*

PATRICIA 5th Technical Review Meeting, Aix-en-Provence, France, October 11, 2023

E. Renaldin

*Cyclotron production of thulium-167 for medical applications (talk)*

11<sup>th</sup> RAD Conference, Herceg Novi, Montenegro, June 19, 2023

E. Renaldin

*Production of radiolanthanides for medical applications (talk)*

Graduate Student Symposium 2023, Universität Bern, Bern, Switzerland, September 13 – 14, 2023

E. Renaldin et al.

*Production cross section measurements of the medically relevant radionuclide thulium-167 using an 18-MeV medical cyclotron (poster)*

SCS Fall Meeting 2023, Universität Bern, Bern, Switzerland, August 24 – 25, 2023

D. Schumann, Đ. Cvjetinović

6th Meeting of the SINCHRON Collaboration, ETHZ, Zurich, Switzerland, February 9, 2023

D. Schumann

*How accurate are half-lives of long-lived isotopes?*

RANC 2023, Budapest, Hungary, May 07 – 12, 2023

D. Schumann, Đ. Cvjetinović

7th Meeting of the SINCHRON Collaboration, PSI, Villigen PSI, Switzerland, 13.06.2023.

D. Schumann, R. Dressler

*Quo vadis, n\_TOF?*

n\_TOF Collaboration Board Meeting, CERN, Geneva, Switzerland, July 12, 2023

D. Schumann

*Isotope production at PSI*

Radioisotope Production at SNS (RIPS) Workshop, ORNL, Oak Ridge, USA, September 27, 2023

D. Schumann, Z. Talip, Đ. Cvjetinović

8th Meeting of the SINCHRON Collaboration, HZDR, Dresden, Germany, 9-10.11.2023.

D. Schumann, Đ. Cvjetinović

7th Meeting of the SINCHRON Collaboration

PSI, Villigen, Switzerland, 13.06.2023.

D. Schumann, Đ. Cvjetinović

6th Meeting of the SINCHRON Collaboration

ETH, Zurich, Switzerland, 09.02.2023.

P. Steinegger

*Chemistry with Superheavy Elements in Switzerland (invited talk)*

Seminar of the Institute of Modern Physics (IMP) of the Chinese Academy of Sciences, Lanzhou, China, July 24, 2023

P. Steinegger

*Chemistry with Superheavy Elements in Switzerland (invited talk)*

Seminar of the Cyclotron Institute, Texas A&M University, College Station, Texas, USA, August 11, 2023

P. Steinegger

*The chemistry of Superheavy Elements – Current activities and what's next? (invited talk)*

7th International Conference on the Chemistry and Physics of the Transactinide Elements (TAN 23), Huizhou, China, November 12 – 17, 2023

P. Steinegger

*Einzelatomchemie am Ende des Periodensystems (invited talk)*

Radioanalytik-Seminar, FHNW Campus Brugg, Brugg, Switzerland, December 06 – 07, 2023

Z. Talip

*WP12 Radiolanthanides (talk)*

PRISMAP Review Meeting, Leuven, Belgium, January 10, 2023

Z. Talip

*Production of Medical Radionuclides from Bench to Bedside (keynote speech)*

Swiss Radiopharmacy Day, Bern, Switzerland, March 8, 2023

Z. Talip

*GMP requirements for the production of novel radionuclides (online talk)*

PRISMAP-EMA ITF Briefing Meeting, March 31, 2023

Z. Talip

*Production of Radiolanthanides for Auger electron Therapy (talk)*

Auger Symposium, Montpellier, France, September 7, 2023

Z. Talip

*WP12 Progress*

PRISMAP 6th Consortium Meeting, Lisbon, Portugal, November 27, 2023

G. Tiebel

*Development of high-temperature chromatography for the heaviest elements (online talk)*

TASCA Workshop 2023 (hybrid workshop), Germany, April 26, 2023

G. Tiebel et al.

*Ion-Funnel-to-IVAC system for experiments with shortest-lived radionuclides beyond Fl (poster)*

NES PhD Day 2023, PSI, Villigen PSI, Switzerland, May 9, 2023

G. Tiebel

*Ion-Funnel-to-IVAC system for experiments with shortest-lived radionuclides beyond Fl (talk)*

NES PhD Day 2023, PSI, Villigen PSI, Switzerland, May 9, 2023

G. Tiebel et al.

*The ion-funnel-to-IVAC system for chemistry experiments with radionuclides having half-lives in the sub-second regime (poster)*

SCS Fall Meeting 2023, Universität Bern, Bern, Switzerland, August 24 – 25, 2023

G. Tiebel

*Production of short-lived radionuclides @ Texas A&M University (seminar talk)*

LRC Seminar, PSI, Villigen PSI, Switzerland, September 29, 2023

G. Tiebel

*The ion-funnel-to-IVAC system for chemistry experiments with radionuclides having half-lives in the sub-second regime (talk)*

7th International Conference on the Chemistry and Physics of the Transactinide Elements (TAN 23), Huizhou, China, November 12 – 17, 2023

G. Tiebel et al.

*The ion-funnel-to-IVAC system for chemistry experiments with radionuclides having half-lives in the sub-second regime (poster)*

NES-ENE FoKo Event 2023, PSI, Villigen PSI, Switzerland, December 4, 2023

N. van der Meulen

*The potential of Tb-149 production towards targeted alpha therapy (invited talk)*

TAT12, Cape Town, South Africa, March 2, 2023

N. van der Meulen

*The production of radionuclides towards theragnostics application (invited talk)*

ISTR-2023, Vienna, Austria, April 20, 2023

N. van der Meulen

*The development of radionuclides towards theragnostic application in nuclear medicine (invited online talk)*

16<sup>th</sup> Varenna Conference on Nuclear Reaction Mechanisms (NRM2023), Varenna (online), 16 June 2023

N. van der Meulen

*Development of radionuclides towards clinical application: an overview of emerging radionuclides (invited talk)*

SASNM 2023, Gqeberha, South Africa, August 24 – 27, 2023

N. van der Meulen

*Terbium-149 production: a pragmatic view of its clinical potential (talk)*

EANM'23, Vienna, Austria, 10 September 10, 2023 (top rated oral presentation)

Chaired TROP Session "Radiopharmaceutical Sciences + Translational Molecular Imaging & Therapy - At the Nucleus: Radionuclide Production" at EANM'23

N. van der Meulen et al.

*Targeted Alpha Tumour Therapy and Other Oncological Solutions (TATTOOS) as part of Paul Scherrer Institute's IMPACT Large Facilities project (poster)*

NES-ENE FoKo Event 2023, PSI, Villigen PSI, Switzerland, December 4, 2023

J. Wilson

*Gas-Phase Chemistry of Group 13 Elements (online talk)*

TASCA Workshop 2023 (hybrid workshop), Germany, April 26, 2023

J. Wilson

*Online Gas Adsorption Chromatography of Thallium (seminar talk)*

ASRC Internal Seminar, Japan Atomic Energy Agency, Tokai-mura, Japan, June 21, 2023

J. Wilson et al.

*Gas-Phase Adsorption Chromatography of Thallium on Dehydroxylated Fused Silica Surfaces (poster)*

SCS Fall Meeting 2023, Universität Bern, Bern, Switzerland, August 24 – 25, 2023

J. Wilson

*Gas-Phase Chromatography Studies at JAEA (seminar talk)*

LRC Seminar, PSI, Villigen PSI, Switzerland, September 29, 2023

J. Wilson

*Gas-Phase chemistry experiments with thallium, the lighter homolog of nihonium (talk)*

7th International Conference on the Chemistry and Physics of the Transactinide Elements (TAN 23), Huizhou, China, November 12 – 17, 2023

J. Wilson et al.

*Gas-Phase Adsorption Chromatography of Thallium on Dehydroxylated Fused Silica Surfaces (poster)*

NES-ENE FoKo Event 2023, PSI, Villigen PSI, Switzerland, December 4, 2023

I. Zivadinovic

*Po release from MEGAPIE samples (online talk)*

4th PATRICIA Technical Review Meeting, April 3 – 5, 2023

I. Zivadinovic et al.

*Evaporation of polonium from heavy-liquid-metal-cooled reactors (poster)*

Heavy Metal Summer School, SCK•CEN, Mol, Belgium, June 12 – 16 2023

I. Zivadinovic et al.

*Evaporation of polonium from heavy-liquid-metal-cooled reactors (poster)*

SCS Fall Meeting 2023, Universität Bern, Bern, Switzerland, August 24 – 25, 2023

I. Zivadinovic

*Transpiration experiments with Po from MEGAPIE samples (online talk)*

5th PATRICIA Technical Review Meeting, October 10 – 12, 2023

I. Zivadinovic

*Evaporation of polonium and tellurium from heavy-liquid-metal-cooled reactors*

LRC Seminar, PSI, Villigen PSI, Switzerland, October 20, 2023

I. Zivadinovic et al.

*Evaporation of polonium from heavy-liquid-metal-cooled reactors (poster)*

NES-ENE FoKo Event 2023, PSI, Villigen PSI, Switzerland, December 4, 2023

V. Zobnin, J. Neuhausen

*Updates on task 3.1 – Fission product release from HLM and deposition from the gas phase (online talk)*

PASCAL progress meeting, April 18 – 19, 2023

V. Zobnin, J. Neuhausen, R. Eichler

*Identification of volatile tellurium species in vapors over lead-bismuth eutectic melts (poster)*

Heavy Metal Summer School, SCK•CEN, Mol, Belgium, June 12 – 16 2023

V. Zobnin, J. Neuhausen, R. Eichler

*Thermosublimatographic study of Te volatile species formed over LBE melts (poster)*

SCS Fall Meeting 2023, Universität Bern, Bern, Switzerland, August 24 – 25, 2023

V. Zobnin, J. Neuhausen

*Updates on task 3.1 – Fission product release from HLM and deposition from the gas phase (talk)*

PASCAL progress meeting, SCK•CEN, Mol, Belgium, September 20 – 22, 2023

V. Zobnin, J. Neuhausen, R. Eichler

*Thermosublimatographic study of tellurium speciation in vapors over lead-bismuth eutectic melts (talk)*

LRC Seminar, PSI, Villigen PSI, Switzerland, October 20, 2023

V. Zobnin, J. Neuhausen, R. Eichler

*Thermosublimatographic study of Te volatile species formed over LBE melts (poster)*

NES-ENE FoKo Event 2023, PSI, Villigen PSI, Switzerland, December 4, 2023

## Public relations and outreach activities

P. Steinegger

*Fantastic Elements and where to find them (talk)*

DL23-I, Stab BR NAZ, Federal Training Center (FTCS), Schwarzenburg, Switzerland, March 21 – 24, 2023

P. Steinegger

*Produktion von Radionukliden für die Forschung und Medizin (talk)*

Besuchstag Labor Spiez am PSI, PSI, Villigen PSI, Switzerland, July 4, 2023

P. Steinegger

*Speeddating mit Radioaktiven Schwergewichten*

Studieninformationstage 2023, ETHZ (HG), Zürich, Switzerland, September 6, 2023

M. Hofstetter

*Grundlagenseminar der Schweizerischen Gesellschaft der Kernfachleute (participation)*

Magglingen, Switzerland, October 02 – 05, 2023

M. Hofstetter

*Radioanalytik-Seminar (participation)*

FHNW Campus Brugg, Brugg, Switzerland, December 06 – 07, 2023

## Internal presentations

R. Eichler

*Update TATTOOS November 2023*

7<sup>th</sup> HIMB External Advisory Board meeting, Paul Scherrer Institute, Switzerland, November 6-7, 2023

R. Eichler

*The Laboratory of Radiochemistry*

Seminar at the LRC visit to EMPA St. Gallen, St Gallen, Switzerland, September 27, 2023

P. Steinegger

*The Heavy Elements Group of LRC*

LRC Orientation Day, PSI, Villigen PSI, Switzerland, December 8, 2023

Z. Talip

*Medical Radionuclide Production at the Paul Scherrer Institute*

PSI Human Resources, PSI, Villigen PSI, Switzerland, March 31, 2023

Z. Talip

*Isotope and Target Chemistry Group*

LRC Orientation Day, PSI, Villigen PSI, Switzerland, December 8, 2023

Z. Talip

Production of Medical Radionuclides at PSI (invited talk)

PSI-ASI Seminar, PSI, Villigen PSI, Switzerland, December 12, 2023

Z. Talip

*Non-linear Career Path*

PSI Fellow Program Career Talk, PSI, Villigen PSI, Switzerland, December 13, 2023

N. van der Meulen

*The development of radionuclides towards clinical translation*

CRS Networking event (with invited industrial partners), PSI, Villigen PSI, Switzerland, June 22, 2023

N. van der Meulen

*PSI-INFN Radionuclide/Radiopharmacy Collaboration: where are we and where do we overlap?*

PSI-INFN Meeting, PSI, Villigen PSI, Switzerland, September 6, 2023

N. van der Meulen

*Targeted Alpha Tumour Therapy and Other Oncological Solutions (TATTOOS) as part of Paul Scherrer Institute's IMPACT Large Facilities project*

1<sup>st</sup> TATTOOS External Advisory Board Meeting (online), November 23, 2023

N. van der Meulen

*Radionuclide Development. To infinity...and beyond!*

LRC Orientation Day, PSI, Villigen PSI, Switzerland, December 8, 2023

N. van der Meulen

*Radionuclide Development. Tb-161: To infinity...and beyond!*

PROGNOSTICS consortium meeting, Basel University Hospital, Basel, Switzerland, December 15, 2023

## Membership in scientific committees and external activities

### Noemi Cerboni

- International Nuclear Target Development Society (INTDS), co-editor newsletter

### Đorđe Cvjetinović

- PSI Fellow Board, board member

### Prof. Dr. Robert Eichler

- Associate Editor of the International Journal of Modern Physics E (IJMPE) World Scientific Publishing
- Labor für Ionenstrahlphysik ETH Zürich, Member of Curatorial Board (on behalf of PSI)
- Radiochimica Acta, Member of the Scientific Advisory Board

**Dr. Emilio A. Maugeri**

- International Nuclear Target Development Society (INTDS), executive board member

**Dr. Jörg Neuhausen**

- PATRICIA, work package leader

**Prof. Dr. Patrick Steinegger**

- Platform Chemistry, Swiss Academy of Sciences, board member
- Fachgruppe Nuklearchemie, German Chemical Society (GDCh), counselor (not elected)
- Division of Nuclear and Radiochemistry (DNR), European Chemical Society (EuChemS), board member
- Division of Fundamental Research (DFR), Swiss Chemical Society (SCS), board member
- CERN-ISOLDE Collaboration Committee (representative for Switzerland w/ Dr. N. van der Meulen)

**Dr. Zeynep Talip**

- PRISMAP, work package leader
- Member of NuPECC Long Range Plan 2024 Applications and Societal Benefit Thematical Working Group (Health and Nuclear Data)

**Dr. Nicholas van der Meulen**

- ARRONAX International Scientific Committee, member
- PSI internal research commission (FoKo), member
- International Advisory Committee for the Workshop on Targetry and Target Chemistry, member
- Public Library Of Science (PLOS), academic editor
- Instruments (MDPI), reviewer board member
- EJNMMI Radiopharmacy and Chemistry, editorial board member
- PSI Team Leader at CERN-ISOLDE
- CERN-ISOLDE Collaboration Committee (representative for Switzerland)
- CERN-MEDICIS Collaboration Board, member

**Lectures and Courses****P. Dutheil**

*Praktikum Allgemeine Chemie (529-0011-04L)*

D-CHAB, ETHZ, January 3 – 25, 2023

**R. Eichler**

*Nuclear and Radiochemistry*

DCBP University of Bern, Fall semester 2023

**R. Eichler**

*Nuclear Fuel Cycle and Disposal (151-0160-00L)*

D-MAVT, ETHZ, Spring semester 2023

**P. Steinegger**

*Vertiefte Grundlagen der Chemie II für Lehrdiplom (529-0961-00L)*

D-CHAB, ETHZ, Spring semester 2023

**P. Steinegger**

*Anorganische Chemie I (529-0121-00 V/U)*

D-CHAB, ETHZ, Fall semester 2023

**G. Tiebel***Praktikum Allgemeine Chemie (529-0011-04L)*

D-CHAB, ETHZ, January 3 – 25, 2023

**Z. Talip***Application of Separation Techniques to Radiolanthanides*

PRISMAP Radiolanthanide Summer School, DTU, Roskilde, Denmark, 10 May 2023

**N. van der Meulen***Basics of separation chemistry*

PRISMAP Radiolanthanide Summer School, DTU, Roskilde, Denmark, 7 May 2023

**N. van der Meulen***Pursuing the theragnostic principle at Paul Scherrer Institute*

TUBITAK visiting scientist programme, Izmir, Turkey, 15 May 2023

**N. van der Meulen**

Terbium Radionuclides for Imaging and Therapy: How Far Have We Progressed?

TUBITAK visiting scientist programme, Aydin, Turkey, 16 May 2023

**N. van der Meulen**

Radionuclides for nuclear medicine: the triumphs and challenge 18 May 2023.

**Awards****G. Tiebel***Best Poster Presentation Award*

NES PhD Day 2023, PSI, Villigen PSI, Switzerland, May 9, 2023

**M. Hofstetter***Best Poster Presentation Award (runner-up)*

SCS Fall Meeting 2023, Universität Bern, Bern, Switzerland, August 24 – 25, 2023

**Master thesis****Marco Witschi (UniBern)***The evaporation behaviour of refractory elements from liquid LBE*

Dr. Jörg Neuhasuen (PSI)

Prof. Dr. Robert Eichler (PSI &amp; UniBern)

September 6, 2023

**Xuandong Kou (ETHZ)***Electrochemical production of targets for nuclear science*

Dr. Emilio A. Maugeri (PSI)

Prof. Dr. Patrick Steinegger (PSI &amp; ETHZ)

September 29, 2023

## Bachelor thesis

### **Sofia Lanfranchi (ETHZ)**

Distribution Coefficients of Different Resins for the Separation of Erbium from Holmium and Thulium

Dr. Zeynep Talip (PSI)

Prof. Dr. Patrick Steinegger (PSI & ETHZ)

December 10, 2023

## Internships and Semester projects

### **Patrick Albrecht (EPFL-ETHZ)**

*Preparation of Natural Hafnium Samples for the Production of  $^{179}\text{Ta}$*

Dr. Đorđe Cvjetinović, Dr. Pascal Grundler, Dr. Dorothea Schumann

Prof. Dr. Annalisa Manera (ETHZ)

September 9 – December 20, 2023

### **Nestor Iwanojko (ETHZ)**

*Analytical approach to simulating molecular flow in IVAC experiments involving SHEs*

Dr. Rugard Dressler (PSI),

Georg Tiebel (PSI & ETHZ)

Prof. Dr. Patrick Steinegger (PSI & ETHZ)

June 1 – November 30, 2023

### **Luca Mössinger (Uni Hamburg)**

*Gas chromatographic behavior of tellurium evaporated from liquid lead bismuth eutectic*

Vladislav Zobnin (PSI)

Prof. Dr. Robert Eichler (PSI & UniBern)

August 7 – October 8, 2023

### **Sofia Pasolini (EPFL-ETHZ)**

*Radionuclide production using thermal neutrons and medium energy protons*

Dr. Zeynep Talip (PSI)

Prof. Dr. Annalisa Manera (ETHZ)

September 9 – December 20, 2023

### **Augustin Pelletier (EPFL-ETHZ)**

*Development of an Aerosol Gas-Jet Degasser-Unit for liquid-phase chemical studies with Fission-Products at SINQ*

Paul Dutheil (PSI & ETHZ)

Dr. Rugard Dressler (PSI)

Prof. Dr. Annalisa Manera (ETHZ)

September 9 – December 20, 2023

### **Sofia Portolan (EPFL-ETHZ)**

*Self-assembled monolayers of radiolanthanides for alpha spectroscopy sources*

Dr. Emilio A. Maugeri (PSI)

Prof. Dr. Annalisa Manera (ETHZ)

September 9 – December 20, 2023

**Felix Weigand (ETHZ)***Electrodeposition of Tb films from ionic liquids*

Noemi Cerboni (PSI &amp; ETHZ)

Dr. Emilio Maugeri (PSI)

Prof. Dr. Patrick Steinegger (PSI &amp; ETHZ)

September 18, 2023 – December 22, 2023

**Grants/funding**

Swiss Roadmap for Research Infrastructures 19, titled "IMPACT - Isotope and Muon Production using Advanced Cyclotron and Target technologies", included into the Swiss Roadmap, January 31, 2023, Robert Eichler & Nicholas van der Meulen

Swiss Nanoscience Institute (SNI), titled "Enabling the challenging separation of radionuclides via the entrapment inside molecular containers", accepted on June 15, 2023, P. Steinegger (co-applicant with Konrad Tiefenbacher, University of Basel/ETH Zürich)

Cancer League (Krebsliga Schweiz) grant proposal titled "Investigation of Auger electron therapy using peptide receptor antagonists that localise at the cellular membrane", as of January 1, 2023, Nicholas van der Meulen (co-applicant)

PHRT proposal titled "PeRsOnalized theraGNOstics of metaStaTIC proState cancer" (PROGNOSTICS), June 10, 2023, Nicholas van der Meulen (collaborator)

**Visiting guests****Daniela Gugiu** (RATEN Institute for Nuclear Research, Pitesti, Romania)**Ana-Maria Ivan** (RATEN Institute for Nuclear Research, Pitesti, Romania)**Lionel Ferry** (CEA, Cardarache, France)**Mojmír Němec & Pavel Bartl** (Czech Technical University, Prague, Czechia)**Gero Frisch** (TU Bergakademie Freiberg, Germany)**Nina Kneip** (Leibniz Universität, Hannover, Germany)**Yuta Ito** (JAEA, Tokai-Mura, Japan)**Mustapha Laatiaoui** (Johannes Gutenberg-Universität Mainz, Mainz, Germany)**Franziska Frei** (METAS, Wabern, Switzerland)**Carina Dirks-Fandrei** (ITM, Garching, Germany)**Steffen Happel** (Triskem, France)

## Presentations in LRC seminars

**Daniela Gugiu** (RATEN Institute for Nuclear Research, Pitesti, Romania)

“ALFRED infrastructure and Romania’s R&D Agenda on LFR”, NES Colloquium, February 20, 2023

**Mojmír Němec & Pavel Bartl** (Czech Technical University, Prague, Czechia)

“Aqueous chemistry of homologues of SHEs at the CTU in Prague”, March 3, 2023

**Gero Frisch** (TU Bergakademie Freiberg, Germany, Germany)

“Electrochemical applications of ionometallurgy: Why we (don’t) use ionic liquids in metal processing?”, LRC Seminar @ ETH Zürich, April 27, 2023

**Nina Kneip** (Leibniz Universität, Hannover, Germany)

“Resonance ionization mass spectrometry: Isotope enrichment of rare species and ultra-trace spectroscopy in actinides”, June 23, 2023

**Yuta Ito** (JAEA, Tokai-Mura, Japan)

“Thermalizing short-lived RI beams for precision spectroscopy”, September 29, 2023

**Mustapha Laatiaoui** (Johannes Gutenberg-Universität Mainz, Mainz, Germany)

„Hyperfine selective chromatography and its potential application beyond Nobelium“, October 13, 2023

**Lionel Ferry & Christian Latge** (CEA, Cadarache, France)

“Jules Horowitz Reactor (JHR): a future Material Test Reactor in support to nuclear industry, regulators and R&D institutes”, NES Colloquium, October 20, 2023

**Vitor Barrote** (PSI, Villigen PSI, Switzerland)

“Characterization of major and minor elements (+Si) in CRUD by SF-ICPMS”, November 3, 2023

**Franziska Frei** (METAS, Wabern, Switzerland)

“The Lab for Ionizing Radiation at METAS”, December 15, 2023



